Nanomechanical Instability and Electron Interference Blockade in Carbon Nanotube Quantum Dots

Dissertation
zur Erlangung des Doktorgrades der Naturwissenschaften
(Dr. rer. nat.)
der Fakultät für Physik
der Universität Regensburg

vorgelegt von

Michael Schafberger
aus
Regensburg

im Jahr 2018

Die Arbeit wurde von Prof. Dr. Christoph Strunk angeleitet.
Das Promotionsgesuch wurde am 23.01.2018 eingereicht.
DasPromotionskolloquium fand am 09.11.2018 statt.

Prüfungsausschuss:	Vorsitzender:	Prof. Dr. Gunnar Bali
	1. Gutachter:	Prof. Dr. Christoph Strunk
	2. Gutachter:	PD. Dr. Andrea Donarini
	weiterer Prüfer:	Prof. Dr. John Lupton

Contents

1

Introduction

Single walled carbon nanotubes were first observed in arc-discharge experiments [1,2] and first measurements of single nanotubes contacted with metallic contacts were performed in 1997 [3, 4]. The ongoing improvement in nano-fabrication techniques opened more possibilities for a large variety of measurements. Since carbon nanotubes are intrinsic one-dimensional conductors, the formation of a quantum dot system is straightforward in comparison to two-dimensional electron gas systems, where the quantum dot has to be constricted electrostatically. Many different transport behaviors were observed in carbon nanotube systems, e.g. Luttinger-liquid behavior [5, 6], ballistic transport [7] and Fabry-Pérot-like oscillations [8]. Adding the possibility of contacting the carbon nanotubes with different types of metallic leads, including ferromagnetic [9] and superconducting materials [10, 11] a lot of research can be performed on such systems.

Having the possibility of performing Shot noise measurements on these systems, a powerful tool to gain a deeper understanding of the underlying processes is at hand [12–14].

In addition, carbon nanotubes have excellent mechanical properties, e.g. a low mass, high stiffness and a huge Young's modulus [15]. They can act as mechanical beam resonators with high quality factors of the bending mode [16, 17]. This allows to employ carbon nanotubes as ultra-sensitive mass sensors [18] and is also a promising system to reach the quantum limit of mechanical motion.

Also from a technological point of view carbon nanotubes represent a promising material system. With the downscaling of transistors in the semiconductor industry reaching its limits [19], Moore's Law [20], which says that the number of transistors in an integrated circuit doubles every two years, will come to an end. Switching from silicon to CNT-based transistors might be the solution to further increase the number of devices in integrated circuits, since no isolation region between the n-type and p-type field effect transistors (FETs) is necessary in CNT CMOS circuits [21]. Apart from replacing active devices, CNTs might also replace on-chip interconnect applications due to their ability to carry high current densities with a fixed resistance over several micrometers [22].

In this thesis the effect of electron interference and nanomechanical instabilities on the transport behavior of carbon nanotube quantum dots is investigated. It is organized as follows: Chapter 2 gives a background on the theory necessary for this thesis. At first the atomic and electric properties of carbon nanotubes, as well as their transport behavior is presented. Then the basics of quantum dots, Coulomb blockade and especially carbon nanotube quantum dots are explained. The next section deals with the effect of charge population trapping in general, in quantum dot systems and in the special case of dark states in carbon nanotube quantum dots due to electron interference. Then different sources of noise and noise measurement techniques are presented. The last section of chapter 2 deals with the nanomechanical properties of suspended carbon nanotubes, the different vibrational modes and their effects on the electronic transport. In chapter 3 the sample fabrication method and the experimental setup, as well as the calibration of the noise measurement setup is presented. Chapter 4 shows the effect of electron interference in a clean and regular carbon nanotube quantum dot. At first, a basic sample characterization is performed, before the transport features of dark states are examined in detail. These are then compared to the theoretical model by numerical simulations. In chapter 5 the influences of nanomechanical motion of a suspended carbon nanotube quantum dot on the electronic transport is presented. After a basic sample characterization, instabilities inside charge transitions and extensions of conducting regions, caused by nanomechanical feedback, are investigated. The magnetic field dependence of these features, as well as their signature in noise measurements are shown. After a general discussion and outlook in chapter 6 the recipes for all fabrication steps are listed in the appendix.

2 Theoretical Background

This chapter provides the theoretical background needed for the interpretation of the experimental results presented in this work.
First the structural, electronic and transport characteristics of carbon nanotubes are shown. The basic principles of Coulomb blockade, quantum dots in general as well as the special case of carbon nanotubes are introduced. Then the effect of coherent population trapping in atomic physics is introduced. This concept is then transfered to quantum dot systems and its realization in a single carbon nanotube quantum dot is explained. An overview of the different sources of noise and noise measurement setups is given. At last the different vibrational modes of suspended carbon nanotubes and their effect on the electronic transport is discussed.

2.1 Properties of Carbon Nanotubes

The following section summarizes the general properties of carbon nanotubes. The atomic structure, the electronic properties and the mechanisms of electronic transport in this material system are presented, following the references [23–26].

2.1.1 Atomic Structure

In nature carbon has different allotropes such as diamond, graphite, graphene, fullerenes or carbon nanotubes. However there are only two variations of valence bonds between the carbon atoms. In one case, one s-orbital and three p-orbitals form four sp^3-orbitals through hybridization. This results in a tetrahedral unit, which forms the three dimensional structure of diamond. The other case is the sp^2 hybridization, formed by one s-orbital and two p-orbitals, which results in a planar hexagonal lattice. This one-atom thick layer is called graphene, which was first experimentally isolated in 2004 [27] and has become increasingly important since.

Carbon nanotubes (CNTs) can be described as a graphene sheet rolled up into a cylinder. If they consist of only one layer of graphene, one speaks about single walled carbon nanotubes (SWCNTs). Their wall thickness therefore is only one carbon atom. A coaxial arrangement of multiple tubes inside each other is called multi walled carbon nanotube (MWCNT). They were first observed in 1991 by S. Iijama [1] via tunneling electron microscopy.
CNTs can be fabricated by different methods such as arc discharge, laser ablation, high pressure CO conversion (HiPCO) and chemical vapor deposition (CVD) [28]. The latter approach was used in this work and is explained in Ch. 3.1.3, with its exact recipe presented in App. A.2.2.

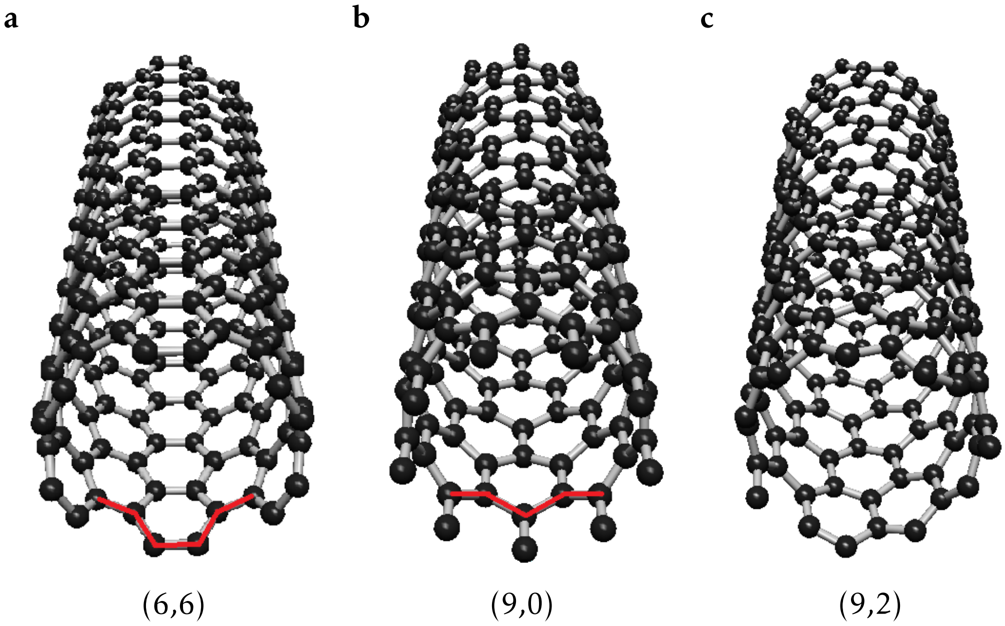

Figure 2.1: Carbon nanotubes with different chiral angles: **a** Armchair CNT, **b** zigzag CNT, **c** chiral CNT. Created with *Nanotube Modeler 1.7.8.*(©JCrystalSoft 2015)

A single walled carbon nanotube is obtained by rolling up a graphene sheet along the chiral vector $\vec{C}$ which is defined via the lattice vectors of graphene $\vec{a}_1$ and $\vec{a}_2$

$$\vec{C} = m \cdot \vec{a}_1 + n \cdot \vec{a}_1 \rightarrow (n,m). \tag{2.1}$$

The chiral indices m and n define the structure of a SWCNT. The tilt angle between the hexagon structure and the nanotube axis, or between $\vec{a}_1$ and $\vec{C}$, is called chiral angle Θ and is also defined by the chiral indices

$$\Theta = \arccos\left(\frac{2n+m}{2\sqrt{n^2+m^2+nm}}\right). \tag{2.2}$$

Due to the hexagonal symmetry of the honeycomb lattice the chiral angle Θ is in the range of $0° \leq |\Theta| \leq 30°$. Depending on Θ one can distinguish three different types of SWCNTs: *Zig-zag* CNTs, where (n,m) = (n,0) and $\Theta = 0°$, form a zig-zag pattern along the circumference, highlighted with a red line in Fig. 2.1a.
Armchair tubes have the conditions (n,m) = (n,n) and $\Theta = 30°$ and show an armchair pattern along the circumference, shown in Fig. 2.1b. The remaining *chiral* tubes with (n,m $\neq$ n $\neq$ 0) and $0° \leq |\Theta| \leq 30°$ feature no distinct pattern at the circumference. One example of a chiral tube with the chiral indices (9,2) is shown in Fig. 2.1c.
The diameter of a CNT d_t also depends on the chiral indices and is given by

$$d_t = \left|\frac{\vec{C}}{\pi}\right| = \frac{a}{\pi}\sqrt{n^2 + m^2 + nm}, \tag{2.3}$$

where a = 1.42 Å$\cdot\sqrt{3}$.
The unit cell of a carbon nanotube is the rectangle *OABB′*, depicted in Fig. 2.2, which is spanned by the vectors $\vec{C}$ and $\vec{T}$. The number of hexagons per unit cell N is defined by

$$N = \frac{|\vec{C} \times \vec{T}|}{|\vec{a}_1 \times \vec{a}_2|}. \tag{2.4}$$

Since each graphene unit cell consists of two atoms, the number of carbon atoms in one CNT unit cell is *2N*.

2.1.2 Electronic Band Structure

Just as the atomic structure of CNTs originates from that of graphene, many properties of the electronic band structure can also be deduced from graphene.
The graphene unit cell contains two atoms with three sp^2-orbitals and one p_z-orbital each. The sp^2-orbitals overlap with those of the neighboring atoms, forming a bonding band σ and an antibonding band σ^*. These bands do not participate in transport, since they are far away from the Fermi level. The p_z-orbitals, which are perpendicular to the honeycomb plane, get delocalized and form bonding and antibonding bands called π and π^*.

In Fig. 2.3a a primitive unit cell of graphene is depicted. It is spanned by the two base vectors $\vec{a}_1$ and $\vec{a}_2$ and contains two carbon atoms A and B. In the reciprocal space the Brillouin zone of the unit cell of graphene is again hexagonal, as depicted in Fig. 2.3b. The corners are alternately labeled K and K'. Since the three K (K') points are connectable by reciprocal lattice vectors, they therefore

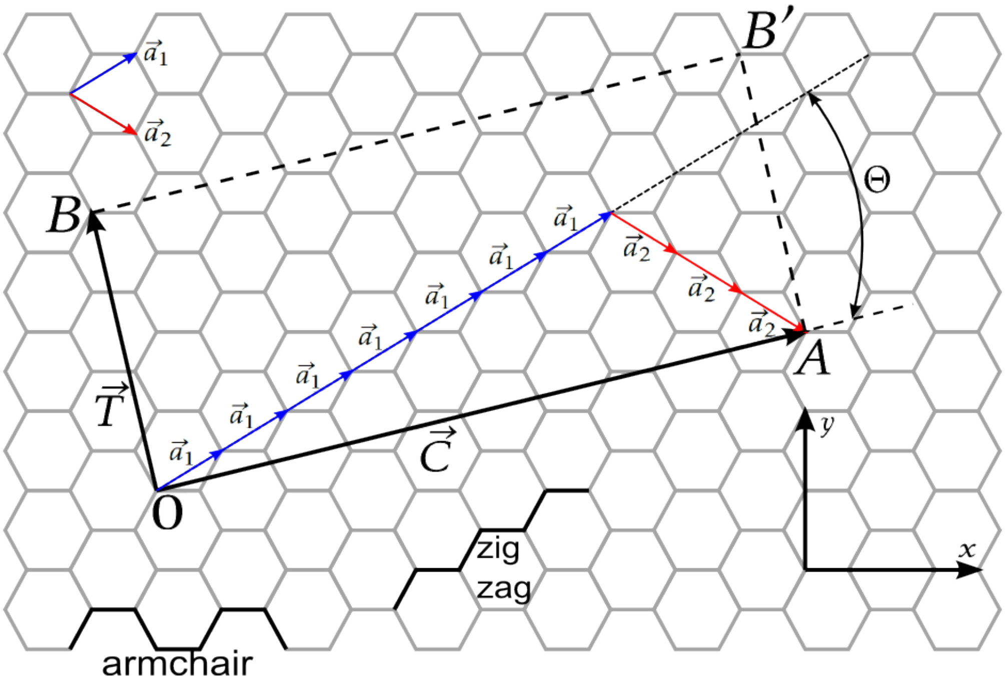

Figure 2.2: Honeycomb lattice of graphene. Surface area of the nanotube is defined by the chiral vector $\vec{C}$ and the translational vector $\vec{T}$. The blue (red) arrows indicate the base vectors $\vec{a}_1$ ($\vec{a}_2$) of graphene. The chiral angle Θ is defined as the tilt angle between the nanotube axis and the underlying hexagon structure.

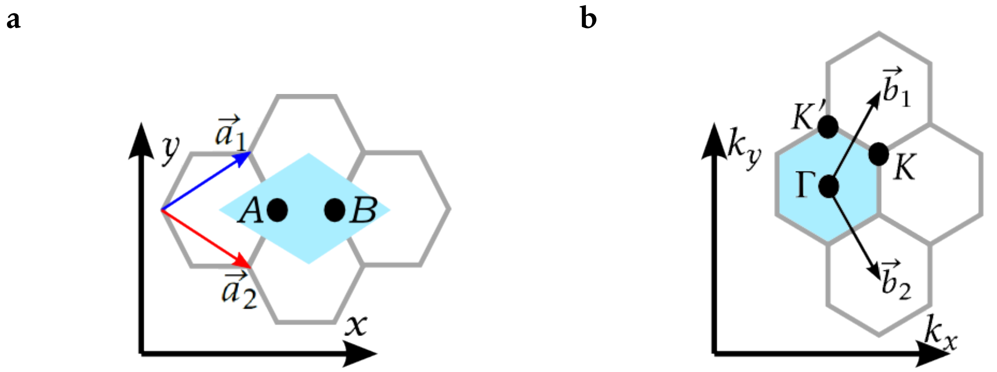

Figure 2.3: **a** Honeycomb lattice in real space. The blue area shows a primitive unit cell containing two atoms A and B. The unit cell is spanned by the two base vectors $\vec{a}_1$ and $\vec{a}_2$. **b** Lattice of graphene in $\vec{k}$-space. The blue hexagon is the first Brillouin zone and $\vec{b}_1$ and $\vec{b}_2$ are the corresponding reciprocal lattice vectors.

correspond to equivalent electron states.
In the tight binding approximation the valence (π) and conduction (π^*) band of graphene can be calculated from the p_z-orbitals of carbon and the simplified dispersion relation can be expressed as

$$E(k_x, k_y) = \pm\gamma_0 \left[1 + 4\cos\left(\frac{\sqrt{3}k_x a}{2}\right)\cos\left(\frac{k_y a}{2}\right) + 4\cos^2\left(\frac{k_y a}{2}\right)\right]^{1/2}, \tag{2.5}$$

where $\gamma_0 \approx 3$ eV is the hopping energy between the carbon atoms.
Following Eq. 2.5 the energy dispersion has no bandgap, since the π and π^* bands touch at K and K', where the density of states is zero. This makes undoped graphene a semimetal.
In a first approximation the graphene band structure stays unperturbed by rolling up into a CNT, except for adding a periodic boundary condition in the circumferential direction. This so called "zone-folding approximation" leads to a quantization of the wave vector component perpendicular to the chiral vector $\vec{C}$:

$$k_\perp = \vec{k} \cdot \vec{C} = 2\pi q, \tag{2.6}$$

where q is an integer. The parallel component of the wave vector stays continuous, since the length of the CNT is assumed infinite. The allowed values of $\vec{k}$ lead to lines in reciprocal space at an angle $\pi/3 + \Theta$ from the k_x axis, with the distance between two lines being inversely proportional to the CNT diameter, i.e. $\Delta k = 2/d$. Since the one-dimensional dispersion relation is a cut of the two-dimensional dispersion relation of graphene along the quantization lines, the chiral vector $\vec{C}$ and chiral angle Θ and therefore the chiral indices (n,m) determine whether a CNT is metallic or semiconducting. In graphene the dispersion relation is linear close to the Fermi surface, which results in a cone-like shape around the Dirac points (K,K'), as depicted in Fig. 2.4a. Since the closest branch to the Fermi level determines the transport behavior, the other cuts can be neglected. Figure 2.4b shows the resulting energy dispersion if a cut runs through a Dirac point. There is no band gap and the corresponding density of states, which is plotted in Fig. 2.4c, is always greater than zero. Therefore the carbon nanotube is metallic. The situation in which there is a separation $|\Delta\kappa_\perp|$ between the cut and the Dirac point is shown in Fig. 2.4d and e. The dispersion relation results in two hyperbolic bands with a gap $E_G = 2\hbar v_F |\Delta\kappa_\perp|$, where $v_F = 8 \times 10^5$ ms^{-1} is the Fermi velocity. The density of states becomes zero inside the bandgap and the CNT is semiconducting. It can be shown that only when the chiral indices are such that (n-m)/3 $\in \mathbb{Z}$ the resulting nanotube is metallic.

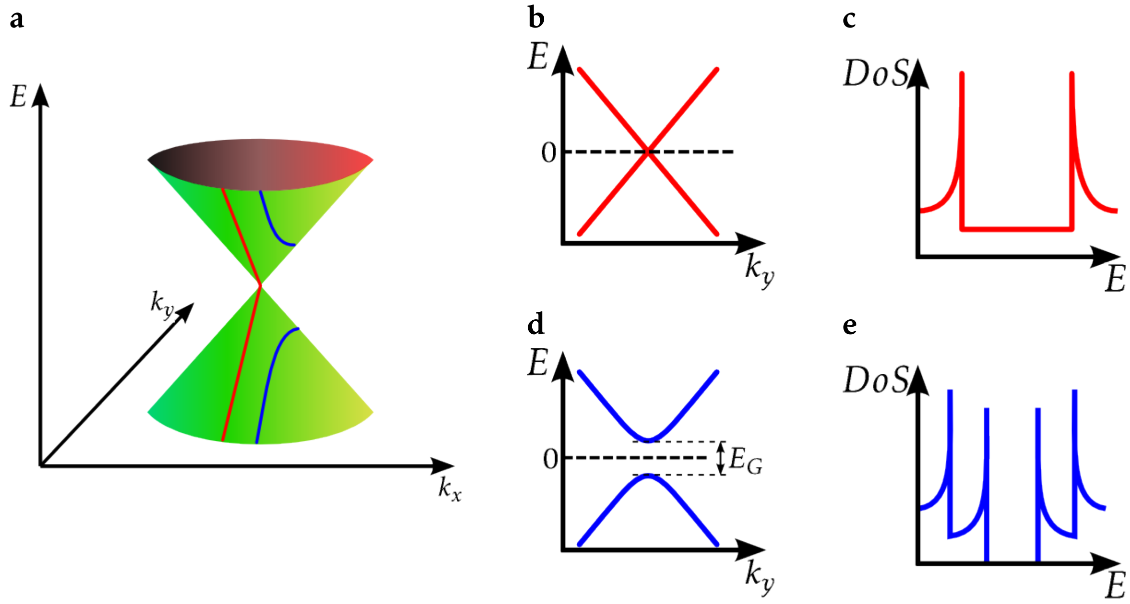

Figure 2.4: **a** Dispersion relation of graphene at low energies results in Dirac cones. Quantized k_x values lead to cuts through the graphene dispersion. **b** If a cut goes through a K point (red line), the CNT dispersion is linear, there is no bandgap and the tube is metallic. **c** The density of states is then constant. **d** If a cut misses the K point (blue line), the resulting CNT dispersion relation shows a bandgap. **e** The tube is semiconducting and the density of states goes to zero within the gap.

2.2 Electronic Transport in Carbon Nanotubes

Considering an electric current through a wire, the conductance G and the resistance R are given by $G = \sigma A/L$ and $R = \rho L/A = G^{-1}$, where L is the length of the conductor and A its cross sectional area. If the conductor is macroscopic, the conductivity σ and the resistivity $\rho = 1/\sigma$ are material constants and independent of the length L and area A. When the size of the conductor becomes small compared to the characteristic lengths for the electron motion, σ and ρ will depend on the length and area of the conductor due to quantum effects like interference caused by scattering on boundaries, defects or impurities.

There are at least three characteristic lengths which have to be considered in mesoscopic systems: The Fermi wavelength λ_F, the mean free path L_m and the phase relaxation length L_ϕ. The Fermi wavelength $\lambda_F = 2\pi/k_F$ is the de Broglie wavelength for electrons at the Fermi energy. The mean free path L_m, or momentum relaxation length, is the average distance an electron travels before it is scattered, and the phase relaxation length L_ϕ is the length over which an electron retains its phase information.

The different scattering mechanisms do not affect these length scales equally. For instance, elastic scattering only contributes to L_m and not L_ϕ, whereas inelastic scattering influences both. The scattering between two electrons does not affect L_m, but only L_ϕ. Since only electrons near the Fermi energy contribute in transport experiments, time scales for the phase relaxation length and the mean free path can be determined via the Fermi velocity, e.g. the momentum relaxation time $t_m = L_m/v_F$ and the phase relaxation time $t_\phi = L_\phi/v_F$. The relation between the length scales determines three different transport regimes: ballistic, diffusive and classic transport. These regimes will be discussed in this section.

2.2.1 Ballistic Transport

For ballistic transport the relation $L \ll L_m, L_\phi$ is valid and leads to conduction of single electrons with no phase and momentum relaxation. This can be described by the Landauer-Büttiker formalism [29]. The current for one conduction channel is given by

$$I = \frac{e}{h} \int d\epsilon (f_L(\epsilon) - f_R(\epsilon)) T(\epsilon), \tag{2.7}$$

where $T(\epsilon)$ is the transmission probability and $f_{L,R}(E)$ is the Fermi Dirac distribution for the two contacts:

$$f_{L,R}(E) = \frac{1}{1 + e^{(E-\mu_{L,R})/k_B T}}. \tag{2.8}$$

For zero temperature the conductance of this system is

$$G(\epsilon') = \frac{e^2}{h} T(\epsilon'). \tag{2.9}$$

This leads to a maximum conductance $G_{max} = e^2/h$ for a mesoscopic conductor in the ballistic transport regime with full transmission ($T = 1$). Due to the spin and valley degeneracy in carbon nanotubes, there are four conductance channels available. Therefore the maximum conductance in CNTs increases to

$$G_{max} = 4\frac{e^2}{h}, \tag{2.10}$$

which leads to a minimal resistance of

$$R_{min} = 1/G_{max} \approx 6.4\ \mathrm{k}\Omega. \tag{2.11}$$

Due to impurities in the carbon nanotube, the conductance in real samples is reduced to $G < 4e^2/h$. Examples of ballistic transport in CNTs, where the tube between the contacts acts as a Fabry-Pérot interferometer, can be found in Ref. [8, 30].

2.2.2 Classical Transport

For $L_\phi \ll L_m \ll L$ phase and momentum relaxation events occur so often that the electron wave function cannot be described by a single phase and therefore the Schrödinger's equation cannot be solved for the entire sample. In this case the total resistance consists of a series connection of microscopic resistances for every momentum relaxation length L_m. Summing up all resistances simply gives Ohm's law as expected for a classical conductor.

2.2.3 Diffusive Transport

For $L_m \ll L_\phi < L$ many elastic scattering events take place. They only affect the mean free path L_m. Therefore the conductor is in the diffusive transport regime and the wave function becomes localized. There are two different cases of localization, which are discriminated by the localization length $L_C = ML_m$, where M is the number of conduction channels. If the phase coherence length L_ϕ is larger than the localization length L_C, the system is in the strong localization regime, where the conductance arises from thermal hopping from one localized state to another. If the localization length is larger than the phase relaxation length, the sample is in the weak localization regime, where universal conductance fluctuations and negative magnetoresistance can be observed. The interaction of electrons with each other has only a small effect on macroscopic systems, since the long range part of the Coulomb interaction is screened. However for conductors of reduced dimensions, the Coulomb interaction is not effectively screened and the electron-electron interaction becomes important. One implication of that is Coulomb blockade, which dominates the electric transport through conductive islands connected to metallic leads via tunneling junctions. This is the case of carbon nanotube samples with high contact resistances. Coulomb blockade is important for the study of transport phenomena and is therefore described in greater detail in the following section.

2.3 Quantum Dots and Coulomb Blockade

In general a quantum dot (QD) is a "zero-dimensional" conductive island surrounded by a non-conductive environment. It can be created by using different methods like, e.g. self assembled metal clusters [31], electrostatically defined QDs in two-dimensional electron gases [32], or contacted nanowires [33]. In this thesis the quantum dot is formed by the suspended part of a CNT, grown over a pair of electrodes. If the distance between the electrodes is small enough, the electron motion is confined in the longitudinal direction as well. To perform transport measurements, source and drain electrodes need to be connected via tunnel junctions, as illustrated in Fig. 2.5. Additionally a capacitively coupled gate electrode is used to adjust the potential of the QD. The transport properties of QDs are summarized in this section following references [34–40].

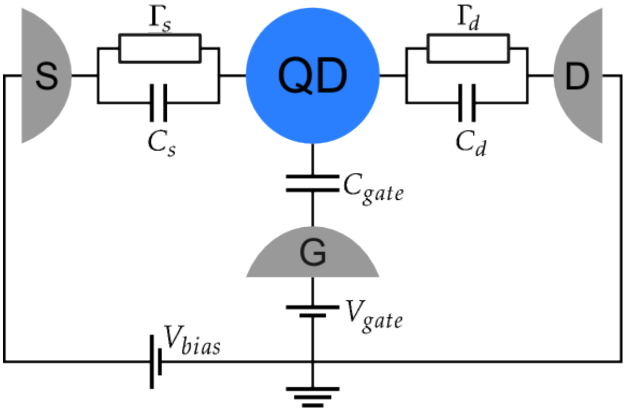

Figure 2.5: Schematic drawing of a quantum dot device. Source and drain electrodes are connected to the dot via tunnel junctions with tunneling rates Γ_s and Γ_d and corresponding capacities C_s and C_d. The gate electrode, used to shift the electronic states of the dot, is capacitively coupled with C_{gate}.

2.3.1 Coulomb Blockade at Zero Bias

A quantum dot can be thought of as a metallic capacitor which can be charged with electrons. To add another electron, one must provide the charging energy which is the energy needed to overcome the Coulomb repulsion caused by the electrons already occupying the dot:

$$U = \frac{e^2}{C_\Sigma}. \tag{2.12}$$

$C_\Sigma = C_s + C_d + C_{gate} + C_{add}$ is the sum of the source, drain, gate and additional capacitances of the dot. For the observation of the phenomenon called Coulomb blockade, two conditions have to be fulfilled:

1. The number of charges has to be fixed, therefore the thermal energy has to be smaller than the charging energy to prevent thermally induced charge fluctuations on the dot
$$\frac{e^2}{C_\Sigma} \gg k_B T. \tag{2.13}$$
At low temperatures this condition can be met by measuring small structures, since the capacitances scale with the size.

2. The number of charges must be well defined in the time scale of a typical experiment, therefore the time for charging and discharging the quantum dot has to be long enough. The charging time for a capacitor is given by $\Delta t = R_t C_{s,d}$, where $R_t = R_{s,d}$ is the tunneling resistance. The Heisenberg uncertainty principle $\Delta E \Delta t = U \Delta t = (e^2/C_\Sigma) R_t C_{s,d}$ implies that the tunneling resistance R_t has to exceed the quantum resistance h/e^2:
$$R_t \gg \frac{h}{e^2} = 25.813\ \mathrm{k\Omega}. \tag{2.14}$$

When the system is in Coulomb blockade no charge transfer through the system is possible due to Coulomb repulsion between the electrons on the dot and in the leads. The dot becomes conductive if the number of charges on the dot can fluctuate by at least one, which means that the probability to find N and $N+1$ charges on the dot is equal. One can derive the probability $P(N)$ for N charges on the dot
$$P(N) = \frac{1}{Z} \exp\left(-\frac{\Omega(N)}{k_B T}\right), \tag{2.15}$$
by using the grand canonical potential $\Omega(N) = F(N) - \mu N$. Here μ is the chemical potential of the leads connecting to the dot, Z is the partition function and
$F(N) = E(N) - ST$ is the free energy:
For low temperatures the free energy can be approximated by the ground state energy $E(N)$ of the quantum dot, which simplifies the condition $P(N) = P(N+1)$ to
$$E(N) - E(N+1) = \mu. \tag{2.16}$$

The chemical potential of the dot is often defined as the energy difference between the dot with N and N + 1 charges.

$$\mu_{dot}(N) \equiv E(N) - E(N+1). \tag{2.17}$$

In the low bias limit single electron tunneling can only occur if the chemical potential of the dot and the leads are equal: $\mu_{dot} = \mu$.

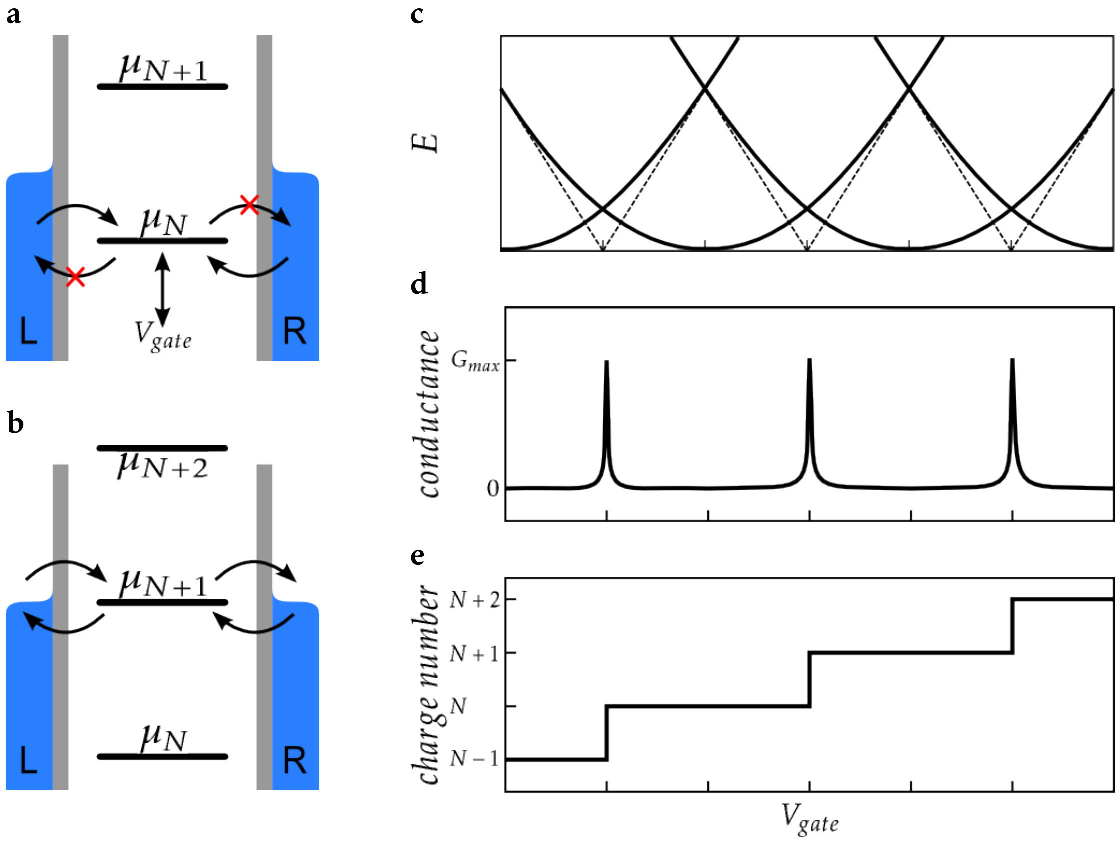

Figure 2.6: Coulomb blockade in a quantum dot at zero bias voltage. **a** Chemical potential of the dot μ_N lies below and μ_{N+1} above the lead potentials. Electrons can tunnel onto μ_N, but are unable to leave the dot, therefore the current is blocked. **b** Potential of the dot μ_N is aligned with the lead potentials. This allows charge fluctuations and the dot becomes conductive. **c** Energy versus gate voltage: quadratic gate voltage dependence leads to parabolas. At the intersection point the energy for N and $N+1$ is equal which allows current flow. **d** This results in peaks in the conductance at the corresponding gate voltage values. **e** For each intersection point, the number of charges occupying the dot is increased by one.

If the chemical potential of the dot lies below the chemical potentials of the leads, charges can tunnel onto the unoccupied state but not out since they can not overcome the energy difference. The quantum dot is in Coulomb blockade (cf. Fig. 2.6a). If the chemical potentials of the leads and the dot align, the charge numbers on the dot can fluctuate and current can flow (cf. Fig. 2.6b).

Assuming the quantum dot to be a metallic island with a constant density of states, one can express the ground state energy of the dot by the classical charging energy of a capacitor:

$$E(N) \simeq \frac{1}{2C_\Sigma}(eN + C_{gate}V_{gate})^2. \tag{2.18}$$

The condition for single electron tunneling can then be expressed as

$$\mu = e\alpha_{gate}V_{gate} + \frac{e^2}{C_\Sigma}\left(N + \frac{1}{2}\right) = e\alpha_{gate}V_{gate} + U\left(N + \frac{1}{2}\right), \tag{2.19}$$

where the ratio between the gate capacitance and the total capacitance was shortened to the so called gate conversion factor α_{gate}:

$$\alpha_{gate} \equiv \frac{C_{gate}}{C_\Sigma}. \tag{2.20}$$

The quantum dot potential can be moved by the gate voltage. The voltage needed to align the next chemical potential of the dot $\mu(N+1)$ to the chemical potential of the leads is

$$\Delta V_{gate} = \frac{e}{\alpha_{gate}C_\Sigma} = \frac{e}{C_{gate}}. \tag{2.21}$$

Figure 2.6c-e depict the discussed properties of the QD. In panel c the electrostatic energy in dependence of the gate voltage is shown. The parabolic behavior is a result of the quadratic dependence on V_{gate} (Eq. 2.18). Each parabola refers to a state with different charge number N and the dashed lines indicate the energy difference between two states. At the intersection points of the parabolas, the charging energy for N and $N+1$ is equal and current can flow. This leads to peaks in the conductance, which are depicted in panel d. Panel e shows the average charge number which increases stepwise by $\Delta N = 1$ every time a conductance peak is passed.

2.3.2 Quantum Coulomb Blockade

So far a metallic quantum dot with a constant density of states was assumed. However in systems where the Fermi wavelength is on the scale of the device itself, the energy levels will be quantized. This quantization can be resolved in experiments if the thermal energy is smaller than the level spacing ($\Delta\epsilon \gg k_BT$). For instance the level spacing $\Delta\epsilon$ of a particle in a box of size L depends on the dimensionality of the system:

$$\Delta\epsilon = \frac{N}{4}\frac{\hbar^2\pi^2}{mL^2} \qquad (1D) \qquad (2.22)$$

$$\Delta\epsilon = \frac{1}{\pi}\frac{\hbar^2\pi^2}{mL^2} \qquad (2D) \qquad (2.23)$$

$$\Delta\epsilon = \left(\frac{1}{3\pi^2 N}\right)^{\frac{1}{3}}\frac{\hbar^2\pi^2}{mL^2} \qquad (3D) \qquad (2.24)$$

Therefore a semiconductor quantum dot with a size of 100 nm has a level spacing of around 0.03 meV. Since the thermal energy at typical cryogenic temperatures (100 mK) is about 0.01 meV, the confinement energy $\Delta\epsilon$ plays a role in the spectrum of the quantum dot.

2.3.3 Coulomb Blockade at Finite Bias

Up to this point the quantum dot was only charged by providing energy via the gate electrode. By applying a bias voltage to the leads the difference of the chemical potentials of source and drain μ_s and μ_d can be varied respectively ($eV_{bias} = \mu_s - \mu_d$). This interval between μ_s and μ_d is called the bias window and in the classical regime, transport through the dot can only take place if the chemical potential of the dot lies within it. Performing a bias spectroscopy measurement where bias and gate voltage are changed continuously while the current through the dot is measured one obtains a color plot of the current as a function of V_{gate} and V_{bias}. This so called *charging* or *stability diagram* is depicted in Fig. 2.7a. In the white, diamond-shaped regions (blue circled 1 in Fig. 2.7a), no energy level is located inside the bias window and therefore no current through the dot is flowing. This pattern is known as *Coulomb diamonds*. The corresponding energy diagram (Fig. 2.7b sub-panel 1) shows that charges from both leads can tunnel into the dot, but cannot tunnel out, since the state of the dot lies below the chemical potentials of the leads. Therefore no current can flow. Increasing V_{gate} or V_{bias} correspondingly, one can get to areas (marked with 2), where one state lies within the bias window and therefore the blockade is lifted and current is allowed to flow. Increasing V_{bias} further, another chemical potential level enters the bias window, which leads to a stepwise increase of the current.

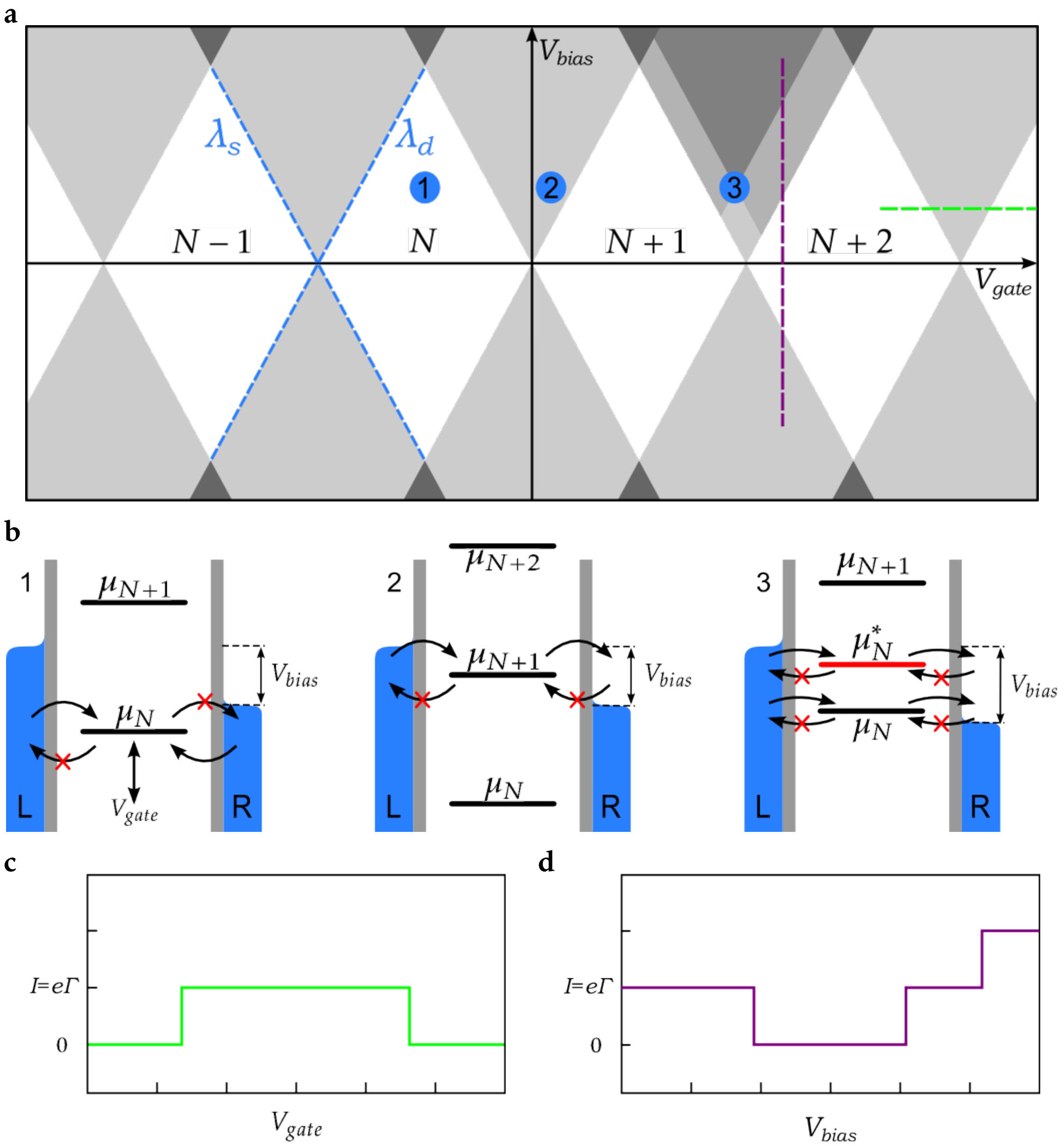

Figure 2.7: Coulomb blockade at finite bias: **a** Stability diagram of a quantum dot in the regime where the Coulomb diamond pattern appears. The blue dashed lines highlight the single electron lines for the source and drain contacts with their corresponding slopes λ_s and λ_d. **b** The chemical potentials for different positions in the stability diagram. **1** Inside the white diamond shaped areas no current is flowing and the particle number, occupying the dot, is constant. 2 A state of the quantum dot enters the bias window which allows current to flow. **3** An additional excited state increases the number of transport channels and therefore the current. **c** Current versus gate voltage at finite bias voltage (cf. green line in panel a). When the line cut goes through the conducting region the current jumps from 0 to $e\Gamma$, leading to a rectangular shape. **d** Current versus bias voltage at a certain gate voltage (cf. purple line in panel a). Excited state in bias window increases current further.

Taking the quantum regime of the transport into account, discrete levels as well as their excitations can be measured. There are two different types of changes in the tunneling current when V_{bias} is increased. The first one corresponds to the change of the number of charge states which are accessible in the bias window. This situation is the same as in the classical case and the voltage difference between these current steps is called *addition energy*. The second type of current change is due to a change in the number of quantum states which can be occupied by an electron on the dot. This situation is illustrated in part 3 of Fig. 2.7b, where an excited state μ_N^* enters the bias window $\mu_s > \mu_N, \mu_N^* > \mu_d$. In this case the current is step-like increased since two charge transfer channels can contribute to the transport and therefore increase the tunneling probability. The voltage difference for this type of current change is called *excitation energy*. The case of an excited level entering the bias window is presented in Fig. 2.7d, where the bias voltage dependence of the current is sketched at a gate voltage position, indicated by the purple dashed line in Fig. 2.7a.

The edges of the Coulomb diamonds, depicted as blue dashed lines in Fig. 2.7a, are called *source* and *drain* lines, along which the chemical potential of the source (drain) contact μ_s (μ_d) is aligned to μ_{dot}. According to Eq. 2.19, the dot potential along the drain line can be expressed as

$$\mu_{dot} = \mu_d = E_N + \left(N + \frac{1}{2}\right)\frac{e^2}{C_\Sigma} + e(\alpha_s V_{bias} + \alpha_{gate} V_{gate}) = const. \tag{2.25}$$

Also the source line can be written similarly

$$\mu_{dot} = \mu_s = E_N + \left(N + \frac{1}{2}\right)\frac{e^2}{C_\Sigma} + e[(1 - \alpha_s) V_{bias} + \alpha_{gate} V_{gate}] = const. \tag{2.26}$$

One can now define additional conversion factors for source (α_s) and drain (α_d) contacts:

$$\alpha_s \equiv \frac{C_s}{C_\Sigma}, \quad \alpha_d \equiv \frac{C_d}{C_\Sigma}. \tag{2.27}$$

With these two equations the slopes of the single electron lines (source line and drain line) can be determined as

$$\lambda_s \equiv \frac{dV_{Gate}}{dV_{bias}} = \frac{1 - \alpha_s}{\alpha_{gate}} = \frac{C_\Sigma - C_s}{C_{gate}}, \tag{2.28}$$

$$\lambda_d \equiv \frac{dV_{gate}}{dV_{bias}} = -\frac{\alpha_s}{\alpha_{gate}} = -\frac{C_s}{C_{gate}}. \tag{2.29}$$

Therefore the gate conversion factor α_{gate} can be expressed as:

$$\alpha_{gate} = \frac{1}{|\lambda_s| + |\lambda_d|}. \tag{2.30}$$

2.3.4 Carbon Nanotube Quantum Dots

In carbon nanotube quantum dots three different transport regimes, depending on the transparency of the contact-tube interface, can be observed. In contrast to split gate defined heterostructure quantum dots, the transparency cannot easily be controlled, but is set by the relation of the work function of the contact material and the nanotube. It can be varied by the gate voltage and is often different for the hole and electron side of semiconducting nanotubes. This behavior is shown for instance in [41–43].

For high transparencies the CNT is in the so called *Fabry-Pérot regime*. It behaves like a one-dimensional coherent electron wave guide. The weak barriers at the contacts define a cavity whose transport behavior can be described as a Fabry-Pérot interferometer. In this regime, which was already mentioned in Ch. 2.2.1, the conductance can reach the limit of $4e^2/h$. For more opaque contact interfaces and a conductance of $G \lesssim 1.5e^2/h$, the system is in an intermediate transport regime where high order effects like cotunneling and the Kondo effect appear [38, 44–46]. Therefore this regime is often referred to as *Kondo regime*.

For low contact transparencies and a low conductance ($G \ll 1e^2/h$) Coulomb blockade dominates the transport and the system is in the so called *closed regime*. Here single electrons tunnel sequentially through the dot, which is why such a device is often referred to as a single electron transistor (SET).

A stability diagram in the closed regime shows a pattern originating from the subsequent shell filling of the dot. This is presented in Fig. 2.8c. Due to the K/K' and spin degeneracy, a fourfold pattern can be observed. This pattern is needed to extract important transport parameters of the device [48–50]. These parameters are the quantum energy level separation $\Delta\epsilon$, the charging energy U, the subband mismatch δ and the exchange energy J. Figure 2.8a and b sketch the meaning of these energies. The exchange energy J is equal to the energy difference between a parallel and anti-parallel spin configuration in two different orbital states. The band mismatch δ is the small energy difference between the two branches and $\Delta\epsilon$ is the energy spacing of two quantized levels of the CNT band structure.

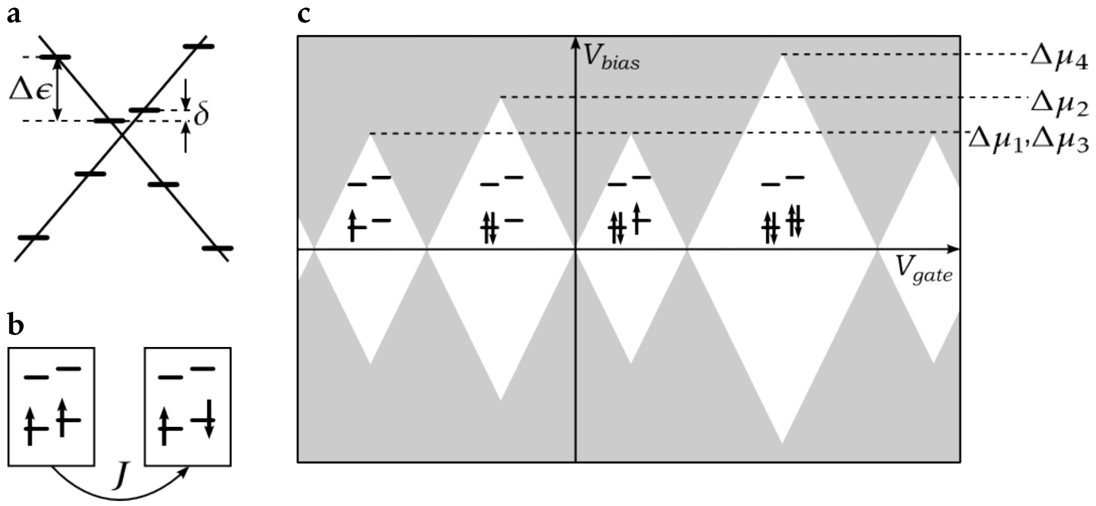

Figure 2.8: Shell filling of a CNT quantum dot. **a** Dispersion relation of a carbon nanotube with discrete energy levels with a separation of $\Delta\epsilon$. The subband mismatch δ shifts the levels of the two branches slightly. **b** The energy difference between two spins with a parallel and anti-parallel configuration in two different orbital states is called exchange energy J. **c** Stability diagram of a carbon nanotube quantum dot, which shows a four fold symmetry in the Coulomb diamond pattern. The sizes of the Coulomb diamonds vary between small, medium, small and large. The respective energies, which can be extracted, are labeled $\Delta\mu_i$ for $i \in \{1,2,3,4\}$. Adapted from [47].

According to [51] the Hamiltonian for the exchange interaction is defined as

$$H_J = -\frac{J}{2}\sum_{\sigma=\pm}\Big[n_{K,\sigma}n_{K',\sigma} + d^\dagger_{K,\sigma}d^\dagger_{K',-\sigma}d_{K,-\sigma}d_{K',\sigma}\Big], \tag{2.31}$$

where $n_{K,\sigma}$ is the number of electrons with spin σ and pseudo-spin K and $d^{(\dagger)}_{K,\sigma}$ describes the removal (addition) of an electron with the quantum numbers K and σ. Assuming $\delta = 0$, the following expressions for the addition energies can be written as:

$$\Delta\mu_1 = U - \frac{J}{2}, \tag{2.32}$$

$$\Delta\mu_2 = U + \frac{3J}{2}, \tag{2.33}$$

$$\Delta\mu_3 = \Delta\mu_1, \tag{2.34}$$

$$\Delta\mu_4 = U + \Delta\epsilon - \frac{J}{2}. \tag{2.35}$$

Here μ_i are the addition energies for specific charge numbers $i \in \{1,2,3,4\}$ within a fourfold degenerate shell.

2.4 Coherent Population Trapping

In Ch. 2.3 it was shown that the spatial confinement and the finite length of a CNT leads to discrete atom-like levels in its energy dispersion. Therefore these quasi 0D nanostructures are often referred to as *artificial atoms* [52]. This analogy suggests to transfer concepts of atomic physics to quantum dots [53].

2.4.1 Coherent Population Trapping in Optics

One effect of atomic physics is the coherent population trapping (CPT), where illumination of atoms can trap electrons into a coherent superposition of orbital states, which are completely decoupled from the dynamics and do not emit fluorescent light [54–56]. Therefore these states are called *dark states*. They were observed for the first time by Alzetta et al. when sodium vapor was illuminated by a dye laser, in a way that the hyperfine splitting of the ground state matched the frequency difference of the two modes of the laser [57]. This observation was explained by Arimondo and Orriols in their analysis of a three level system in the folded (Λ-shaped) configuration [58]. This level system is depicted in Fig. 2.9.

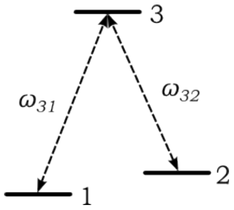

Figure 2.9: Λ- shaped three level system of atomic levels. Two energy levels 1 and 2 have a common excited state 3. The corresponding optical transitions with frequencies ω_{21} and ω_{31} are depicted with dashed arrows.

They consider an atomic system consisting of two levels 1 and 2, which have a energy separation in the microwave region, and a common excited state 3. This level is coupled to the lower states by optical transitions at frequencies ω_{31} and ω_{32}. The laser which illuminates the system contains two coherent modes with frequencies ω_1 and ω_2, amplitudes E_1 and E_2 and a phase difference Φ. Its electric field, polarized along the x-axis and propagating in the z-direction, can be described as

$$E_x(z,t) = \frac{1}{2}E_1\{\exp[1(\Omega_1 t - K_1 z_0)] + c.c\} + \frac{1}{2}E_2\{\exp[1(\Omega_2 t - K_2 z_0 + \Phi)] + c.c\},$$

where $\Omega_i = \omega_i - K_i v_z$ and $i = 1,2$. The Doppler shift $K_i v_z$, due to the thermal motion of the atoms, along the z-direction is taken into account. Each laser mode is supposed to interact with only one optical transition. This approximation is valid for a mode separation $\omega_1 - \omega_2$ smaller than the optical linewidth. The interaction of the electromagnetic field with the atomic system is described by two generalized Rabi frequencies

$$\alpha = \frac{\mu_{13} E_1}{2\hbar} \quad \text{and} \quad \beta = \frac{\mu_{23} E_2}{2\hbar} \exp[i\Phi], \tag{2.36}$$

where μ_{13} and μ_{23} are the electric dipole matrices.
In the rotating wave approximation, where rapidly oscillating terms are removed, the motion equations of the density matrix ρ can be written as

$$\dot{\rho}_{11} = i\alpha(\tilde{\rho}_{31} - \tilde{\rho}_{13}) - \frac{\rho_{11} - \rho_{22}}{\tau_1} + f\frac{\rho_{33}}{T_1}, \tag{2.37}$$

$$\dot{\rho}_{22} = i\beta^*(\tilde{\rho}_{32} - \tilde{\rho}_{23}) - \frac{\rho_{22} - \rho_{11}}{\tau_1} + (1-f)\frac{\rho_{33}}{T_1}, \tag{2.38}$$

$$\dot{\rho}_{33} = i\alpha(\tilde{\rho}_{13} - \tilde{\rho}_{31}) - i(\beta\tilde{\rho}_{23} - \beta^*\tilde{\rho}_{32}) - \frac{\rho_{33}}{T_1}, \tag{2.39}$$

$$\dot{\tilde{\rho}}_{13} + i(\Delta - i/T_2)\tilde{\rho}_{13} = i\alpha(\rho_{33} - \rho_{11}) - i\beta^*\tilde{\rho}_{12}, \tag{2.40}$$

$$\dot{\tilde{\rho}}_{23} + i(\Delta' - i/T_2)\tilde{\rho}_{23} = i\beta^*(\rho_{33} - \rho_{22}) - i\alpha\tilde{\rho}_{21}, \tag{2.41}$$

$$\dot{\tilde{\rho}}_{12} + i(\Delta - \Delta' - i/\tau_2)\tilde{\rho}_{12} = i\alpha\tilde{\rho}_{32} - i\beta\tilde{\rho}_{13}, \tag{2.42}$$

where

$$\Delta = \Omega_1 - \omega_{31}, \quad \Delta' = \Omega_2 - \omega_{32}, \quad \Delta - \Delta' = \Omega_1 - \Omega_2 - \omega_{21}.$$

Here the relaxation processes are included with T_1 as the relaxation time from the excited state ρ_{33}, T_2 the decay time for the optical coherences ρ_{13} and ρ_{31}, τ_2 as the time constant for the lower states coherence ρ_{12} and τ_1 as a relaxation time to produce equal populations in the lower states. f and $1-f$ are the probabilities for the decay in the states 1 and 2 respectively and the optical coherences are defined as

$$\rho_{13} = \tilde{\rho}_{13} \exp[i(\Omega_1 t - K_1 z_0)], \tag{2.43}$$

$$\rho_{23} = \tilde{\rho}_{23} \exp[i(\Omega_2 t - K_2 z_0)], \tag{2.44}$$

$$\rho_{12} = \tilde{\rho}_{12} \exp[i(\Omega_1 - \Omega_2)t]. \tag{2.45}$$

If one now substitutes $\tilde{\rho}_{13}$ and $\tilde{\rho}_{23}$ in Eq. 2.39 and assumes that both laser modes are in resonance with the optical transitions ($\Delta = \Delta' = 0$), the expression for ρ_{33} results in

$$\rho_{33} = 2\alpha^2 T_1 T_2(\rho_{11} - \rho_{33}) + 2\beta^2 T_1 T_2(\rho_{22} - \rho_{33}) + 4\alpha\beta T_1 T_2 \operatorname{Re}(\tilde{\rho}_{12}). \tag{2.46}$$

Assuming that the optical transitions 1-3 and 2-3 act separately one can show that $\tilde{\rho}_{12}$ is a negative real quantity. Therefore the interference, which is the third term in Eq. 2.46, leads to a decrease in the excited state population ρ_{33}.
Following the analysis of Brewer and Hahn [59] one obtains a solution for Eq. 2.37 - 2.42 and ρ_{33} can be plotted where one laser mode is kept in resonance ($\Delta = 0$) while the frequency of the other is swept through the resonance condition for the two quantum Raman transition connecting the two ground states 1 and 2:

$$\Delta' - \Delta = \omega_{21} - (\omega_1 - \omega_2) - (K_2 - K_1)v_z = 0. \tag{2.47}$$

Figure 2.10 shows that ρ_{33} has a minimum value in a narrow region near the resonance with linewidth fixed by the relaxation time of the ground state coherence τ_2. Therefore the excited state is completely depopulated, when both laser excitations are in resonance.

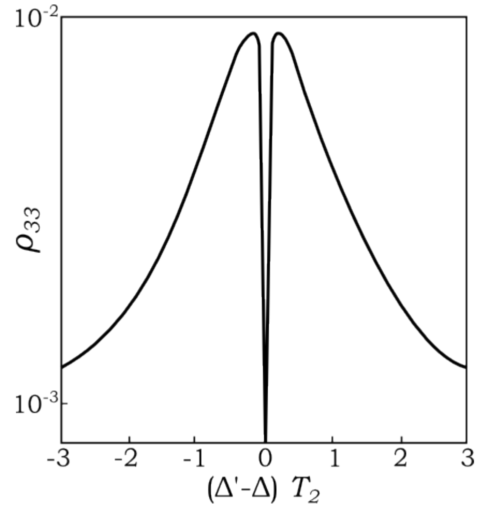

Figure 2.10: Excited state occupation as a function of the resonance parameter $(\Delta' - \Delta)T_2$. Applied parameters: $\Delta = 0$, $\alpha T_2 = |\beta| T_2 = 0.1$, $\Phi = 0$, $\tau_2 = \tau_1 = 10^5 T_2$ and $T_1 = T_2/2$. The minimum value of ρ_{33} is $9 \cdot 10^{-6}$. Taken from [58]

In summary this means, that Raman transitions connecting the levels 1 and 2 create a coherence of the lower states which decreases the net number of transitions from the lower states to the excited state, through the interference term in

Eq. 2.46. This interference phenomenon occurs each time the mode separation matches the ground state splitting.

2.4.2 All Electronic Coherent Population Trapping

An analogue without laser illumination of coherent population trapping in quantum dots was presented by Michaelis et al. [60]. In a system containing three tunnel-coupled quantum dots, an electron can become trapped in a coherent superposition of states in different dots, which blocks the current flow through the system due to Coulomb blockade. For the sake of clarity only the main results are presented. Further details can be found in [60].

In this concept the bias voltage plays the role of the laser illumination, as described in Ch. 2.4.1.

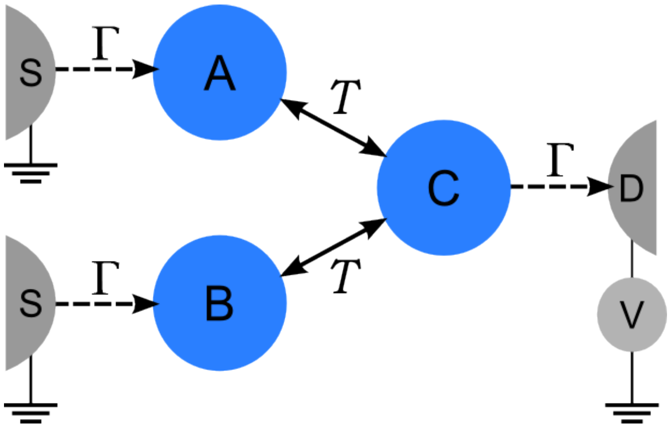

Figure 2.11: System of three quantum dots, in which a dark state can form. The transitions from the source contacts to the quantum dots A and B, and from C to the drain electrode are unidirectional with a tunneling rate Γ. The interdot transitions are labeled with T and are reversible. Sketch adapted from [60].

Figure 2.11 shows the scheme of the three-dot system. The transitions from the leads on the left side to the dots A and B as well as from the dot C to the lead to the right are irreversible due to the bias voltage. They are described by the following jump operators with a tunneling rate Γ:

$$L_A = \sqrt{\Gamma}|A\rangle\langle 0|, \quad L_B = \sqrt{\Gamma}|B\rangle\langle 0|, \quad L_C = \sqrt{\Gamma}|0\rangle\langle C|, \tag{2.48}$$

where $|0\rangle$ is the state in which all three dots are empty. The energies of the single particle levels $|A\rangle, |B\rangle, |C\rangle$ are set to zero, to neglect inelastic transitions between these levels. The elastic transitions between the three quantum dots, with a tunneling rate T are reversible and are described by a tunneling Hamiltonian:

$$H = T\,|C\rangle\langle A| + T\,|C\rangle\langle B| + H.c. = \sqrt{2}T\,|C\rangle\langle\Phi_+| + h.c. \tag{2.49}$$

The superposition of states $|A\rangle$ and $|B\rangle$ is defined as

$$|\Phi_\pm\rangle = \frac{1}{\sqrt{2}}(|A\rangle \pm |B\rangle). \tag{2.50}$$

The dynamics of such a device can be studied by a master equation approach which gives the time evolution of the three-dot density matrix $\rho(t)$:

$$\frac{\mathrm{d}\rho}{\mathrm{d}t} = -i\,[H,\rho] + \sum_{X=A,B,C}\left(L_X\rho L_X^\dagger - \frac{1}{2}L_X^\dagger L_X\rho - \frac{1}{2}\rho L_X^\dagger L_X\right). \tag{2.51}$$

For the basis of the density matrix the four states of the system are used:

$$|e_1\rangle = |\Phi_+\rangle, \quad |e_2\rangle = |\Phi_-\rangle, \quad |e_3\rangle = |C\rangle, \quad |e_4\rangle = |0\rangle, \tag{2.52}$$

The stationary result of Eq. 2.51 is

$$\boxed{\lim_{t\to\infty}\rho(t) = |\Phi_-\rangle\langle\Phi_-|,} \tag{2.53}$$

meaning that, without any sort of decoherence, the electron is trapped in the antibonding superposition of the two states $|A\rangle$ and $|B\rangle$.

This result shows that the effect of coherent population trapping can be achieved without laser illumination, allowing to transfer the CPT concept to an all electronic analogue.

2.4.3 Coherent Population Trapping in Carbon Nanotubes

If one wants to transfer this scheme of charge population trapping to a single quantum dot, an orbital degree of freedom and a source of coherence in the coupling to the leads is needed. In a carbon nanotube quantum dot the first requirement is easily met, since for low energies the valley degree of freedom can be mapped on the orbital one.

In the following segment it will be shown, that electrons which tunnel from the lead to the CNT generally acquire an orbital phase providing coherence. The presentation follows the reference [61]:

In general the tunneling Hamiltonian is written as

$$H_{tun} = \sum_{\alpha\vec{k}ml_z\sigma} t_{\alpha\vec{k}ml_z} d^\dagger_{ml_z\sigma} c_{\alpha\vec{k}\sigma} + h.c., \tag{2.54}$$

where $d^\dagger_{ml_z\sigma}$ creates an electron in the CNT in shell m with angular momentum $l_z = \pm l$ and spin $\sigma = \uparrow, \downarrow$. $c_{\alpha\vec{k}\sigma}$ destroys one electron in the lead $\alpha = L, R$ with spin σ and momentum $\vec{k}$. The tunneling amplitude $t_{\alpha\vec{k}ml_z}$ is the overlap of the wave function of the lead$\Psi_{\alpha\vec{k}\sigma}(\vec{r}) = \langle\vec{r}|\alpha\vec{k}\sigma\rangle$ and of the CNT $\Phi_{ml_z\sigma}(\vec{r}) = \langle\vec{r}|ml_z\sigma\rangle$. It can be written as

$$t_{\alpha\vec{k}ml_z} = \int_{\text{lead}} \mathrm{d}\vec{r}\,\Psi^*_{\alpha\vec{k}\sigma}(\vec{r})\left(\frac{p^2}{2m_{el}} + v(\vec{r})\right)\Phi_{ml_z}(\vec{r}). \tag{2.55}$$

The wave function of the CNT is much more localized than the one of the lead. Therefore the contribution of the lead Hamiltonian to the overlap can be neglected. The electronic properties of the atomic orbitals $|j\rangle$ are mainly given by p_z orbitals, which are assumed to be delta-like $\langle\vec{r}|j\rangle = \delta(\vec{r} - \vec{R}_j)$ at the atomic position $\vec{R}_j$. This leads to the following expression for the tunneling amplitude:

$$t_{\alpha\vec{k}ml_z} = \epsilon_m\langle\alpha\vec{k}\sigma|ml_z\sigma\rangle = \epsilon_m\sum_j\int \mathrm{d}\vec{r}\langle\alpha\vec{k}\sigma|\vec{r}\rangle\langle\vec{r}|j\rangle\langle j|ml_z\sigma\rangle = \epsilon_m\sum_j\langle\alpha\vec{k}\sigma|\vec{R}_j\rangle\langle j|ml_z\sigma\rangle. \tag{2.56}$$

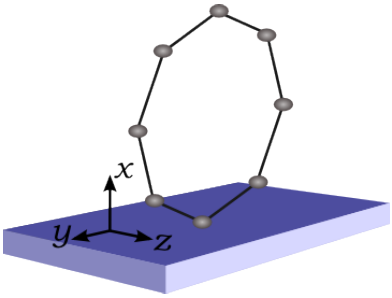

Figure 2.12: Sketch of a ring of carbon atoms standing on a metallic contact, in a way that only one atom touches the surface.

For zigzag-CNTs or carbon nanotubes with small chiral angles the wave function along the tube does not change in the small region of the contact. Therefore the tube can be simplified to a ring with radius R of N carbon atoms. The shell index m can be dropped which leads to $|ml_z\sigma\rangle \rightarrow |l_z\sigma\rangle$ and $\epsilon_m = \epsilon$. The ring Hamiltonian can then be expressed as:

$$\langle j|l_z\sigma\rangle = \frac{1}{\sqrt{N}}e^{i\frac{2\pi}{N}jl_z}. \tag{2.57}$$

The carbon ring is now placed standing on the lead in the y-z plane, as shown in Fig. 2.12. The wave function of the lead can be split into plane waves parallel to the surface and a perpendicular part which is exponentially decaying

$$\Psi_{\alpha\vec{k}\sigma}(\vec{r}) = \Psi^{||}_{\alpha k_y k_z\sigma}(y,z)\Psi^{\perp}_{\alpha k_x\sigma}(x) \propto e^{i(k_y y + k_z z)}e^{-\kappa^\alpha_x x}, \tag{2.58}$$

with $\kappa_x^\alpha = \sqrt{\frac{2m_{el}}{\hbar^2}(E_F^\alpha + \Phi_0^\alpha - k_x^2)}$, where E_F^α and Φ_0^α are the Fermi level and work function of lead α.

The single particle rate matrix for the two angular momentum degenerate states is of the form

$$\begin{aligned}\Gamma^\alpha_{l_z l_z'}(\Delta E) &= \frac{2\pi}{\hbar}\sum_{\vec{k}} t^*_{\alpha\vec{k}l_z} t_{\alpha\vec{k}l_z'}\delta(\epsilon_{\vec{k}} - \Delta E) \\ &= \frac{2\pi}{\hbar}\frac{\epsilon^2}{N}\sum_{jj'} e^{-i\frac{2\pi}{N}(jl_z - j'l_z')}\sum_{\vec{k}}\Psi_{\alpha\vec{k}\sigma}(\vec{R}_j)\Psi^*_{\alpha\vec{k}\sigma}(\vec{R}_{j'})\delta(\epsilon_{\vec{k}} - \Delta E) \\ &= \frac{2\pi}{\hbar}\frac{\epsilon^2}{N}\sum_{jj'} e^{-i\frac{2\pi}{N}(jl_z - j'l_z')}\sum_{\vec{k}} e^{ik_y(Y_j - Y_{j'}) + ik_z(Z_j - Z_{j'}) - \kappa_x^\alpha(X_j + X_{j'})}\delta(\epsilon_{\vec{k}} - \Delta E).\end{aligned} \tag{2.59}$$

Estimating $\kappa_x^\alpha = \sqrt{\frac{2m_{el}}{\hbar^2}(E_F^\alpha + \Phi_0^\alpha) - k_x^2} \geq \sqrt{\frac{2m_{el}}{\hbar^2}\Phi_0^\alpha} = \mathcal{O}(\text{Å}^{-1})$ for typical work functions $\Phi_0 = \mathcal{O}(eV)$ shows that the contribution to the rate matrix is reduced by one order of magnitude for an atom with a distance of 1Å to the lead surface.

Therefore the assumption that tunneling is perfectly local to the atom closest to the lead $j = j' = J$ at distance $X_J = d$ is a good approximation and the rate matrix is in the form of

$$\Gamma^\alpha_{l_z l_z'} = \frac{2\pi}{\hbar}\frac{\epsilon^2}{N} e^{-iJ\frac{2\pi}{N}(l_z - l_z')}\sum_{\vec{k}} e^{-2\kappa_x^\alpha d}\delta(\epsilon_{\vec{k}} - \Delta E) = \Gamma_1 e^{i2\phi^\alpha(l_z - l_z')}. \tag{2.60}$$

The tunneling is now given by the tunneling Hamiltonian

$$\boxed{H_{tun} = \sum_{\alpha\vec{k}ml_z\sigma} t_\alpha e^{il_z\phi_\alpha^m} d^\dagger_{ml_z\sigma} c_{\alpha\vec{k}\sigma} + h.c.,} \tag{2.61}$$

which includes the complex tunneling phases ϕ_α^m. This means that an electron obtains a phase ϕ_α^m by tunneling from (to) a lead α to (from) a state in shell m. These tunneling phases can vary for different shells and leads.

As seen in Eq. 2.60, the rate matrix contains these tunneling phases in the off-diagonal entries, due to the degenerate orbital structure of the system, which strongly affects the dynamics in the quantum dot.

For one electron in shell m one can now find a linear combination

$$\boxed{\left.\begin{matrix}|\mathrm{DS}\rangle \\ |\mathrm{CS}\rangle\end{matrix}\right\} = \frac{1}{\sqrt{2}}\Big(e^{i\ell\phi_\alpha^m}|L_z = \ell\rangle \mp e^{-i\ell\phi_\alpha^m}|L_z = -\ell\rangle\Big),} \tag{2.62}$$

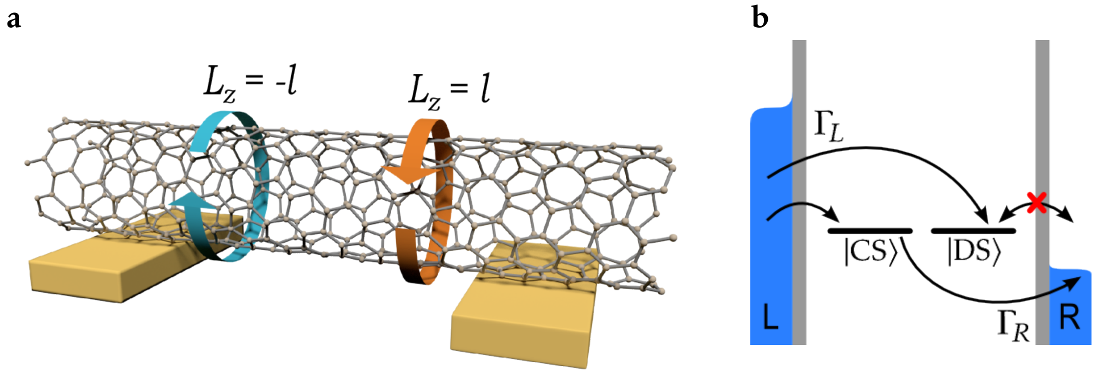

Figure 2.13: **a** Scheme of a CNT lying on top of contacts. The two orbital states of a carbon nanotube are represented as two angular momentum states $L_z = \pm l$. These are illustrated as blue and orange arrows going clockwise and anti-clockwise around the tube. Sketch made by Michael Niklas. **b** Scheme of chemical potentials of a CNT which form a dark state |DS⟩ and a coupled state |CS⟩. An electron can either tunnel from the left lead into the dark or coupled state. The transition from the dark state to the right lead is forbidden which traps an electron there. Therefore once an electron occupies the dark state the current through the dot is blocked.

which diagonalizes the rate matrix. The dark state |DS⟩ is decoupled from lead α through the requirement $\langle L_z = 0|d_{\alpha\sigma}|\mathrm{DS}\rangle = 0$ which means that the probability for the electron to escape the dark state and leave the system with an empty shell ($L_z = 0$) is zero. Here $d_{\alpha\sigma} = \sum_{ml_z} d_{l_z m\sigma} e^{il_z\phi^m_\alpha}$ removes the electron from shell m with spin σ to the lead α, which is where the electron obtains the angular momentum dependent tunneling phase $l_z\phi^m_\alpha$.
For slightly bent or twisted CNTs the tunneling can occur with different phases for the two leads $\phi^m_L \neq \phi^m_R$. This leads to the situation, depicted in Fig. 2.13b, where an electron can occupy the dark state by tunneling from the left lead. Since the electron cannot leave to both leads, it is trapped in the dark state and the current through the quantum dot is suppressed.

Similarly to the one electron case, dark states for two electrons occupying the CNT quantum dot can be found. The requirement $\langle 1, E_{1_0}, \frac{1}{2}, \pm\frac{1}{2}, \pm l|d_{\alpha\sigma}|2, DS\rangle = 0$ forbids the tunneling from the two electron dark state $|2, DS\rangle$ to the lead α leaving the system in the single electron ground state $|1, E_{1_0}, \frac{1}{2}, \pm\frac{1}{2}, \pm l\rangle$. The states are uniquely defined via $|N, E, S, S_z, L_z\rangle$ using the many body quantum numbers, where N is the total particle number, E the energy, S the total spin, S_z the total spin projection and L_z is the total angular momentum. These dark states are strongly dependent on the exchange energy J and can easily be destroyed for $J > 0$.

Considering the interacting of the CNT system with the leads, a Lamb shift Hamiltonian is introduced. It induces a precession between the degenerate angular momentum states and is expressed as

$$\begin{aligned} H_{LS} &= \frac{\hbar}{2\pi} \sum_{\alpha NEE'\sigma} \Gamma_\alpha \mathcal{P}_{NE} \left(p_\alpha(E-E') d^\dagger_{\alpha\sigma} \mathcal{P}_{N+1,E'} d_{\alpha\sigma} + p_\alpha(E'-E) d_{\alpha\sigma} \mathcal{P}_{N-1}, E' d^\dagger_{\alpha\sigma} \right) \mathcal{P}_{NE} \\ &= \hbar \sum_{\alpha NE} \mathcal{P}_{NE} \omega_\alpha^{NE} \mathcal{R}_\alpha^{NE} \mathcal{P}_{NE}, \end{aligned} \tag{2.63}$$

with $p_\alpha(\Delta E) = -\mathrm{Re}\psi[1/2 + i(\Delta E - \mu_\alpha)/2\pi k_B T]$ and ψ is the digamma function. $(\mathcal{R}_\alpha^{NE})_{L_z L_z'} = e^{i\alpha(L_z - L_z')\Delta\phi_\alpha}$ are matrices whose size depends on the angular momentum degeneracy of the state $|NE\rangle$. The precession frequencies ω_α^{NE} originate from the interaction with the leads. They allow an electron, which was originally trapped in the dark state, to precess into the coupled state and from there contribute to the current flow through the system (cf. Fig 2.14). Therefore $\omega_{L/R}$ partially lift the charge trapping in the dark state.

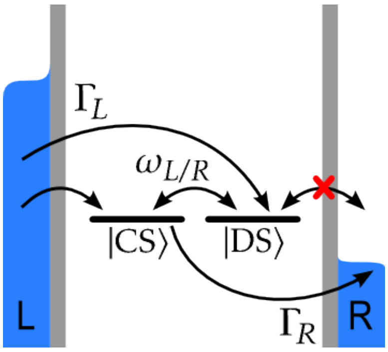

Figure 2.14: Scheme of chemical potentials of a CNT which form a dark state |DS⟩ and a coupled state |CS⟩. An electron can either tunnel from the left lead into the dark or coupled state. A Lamb shift introduces a precession between |DS⟩ and |CS⟩ which allows an electron to escape the dark state and contribute to the transport. The precession frequencies $\omega_{L/R}$ are gate and bias voltage dependent and influence how strongly the current is suppressed.

In order to compute the current numerically a master equation approach for the stationary reduced density matrix of the system ρ^∞ is performed:

$$0 = \mathcal{L}\rho^{\infty} = -\frac{i}{\hbar}[H_{CNT} + H_{LS}, \rho^{\infty}] + \mathcal{L}_{tun}\rho^{\infty} + \mathcal{L}_{rel}\rho^{\infty}. \tag{2.64}$$

Here $\mathcal{L}$ is the Liouville superoperator containing the systems internal dynamics, as well as the Lamb shift contribution H_{LS}, a tunneling part $\mathcal{L}_{tun}$ and a relaxation part $\mathcal{L}_{rel}$. The CNT quantum dot Hamiltonian

$$H_{CNT} = \sum_{ml_z}(m\epsilon_0 - \xi)\hat{n}_{ml_z} + \frac{U}{2}\hat{N}^2 + J\sum_{m}\left(\hat{S}_{ml}\cdot\hat{S}_{m-l} + \frac{1}{4}\hat{n}_{ml}\hat{n}_{m-l}\right) \tag{2.65}$$

includes a constant interaction U and an exchange coupling J.
Also $\hat{n}_{ml_z} = \sum_{\sigma} d^{\dagger}_{ml_z\sigma} d_{ml_z\sigma}$ and $\hat{S}_{ml_z} = \frac{1}{2}\sum_{\sigma\sigma'} d^{\dagger}_{ml_z\sigma}\sigma_{\sigma\sigma'} d_{ml_z\sigma}$ is employed. In the calculations 3 shells ($m \in 0,1,2$) are considered and $\xi = \epsilon_0/2 + 4UN_c + J/2 + e\alpha_g V_g$ ensures particle-hole symmetry when a gate voltage V_g with lever arm α_g is applied. This Hamiltonian can be diagonalized by using the many-body quantum numbers for the corresponding operators of the total particle number $\hat{N} = \sum_{ml_z}\hat{n}_{ml_z}$, the total spin $S^2 = \sum_{ml_z}\hat{S}^2_{ml_z}$, the total spin projection $S_z = \frac{1}{2}\sum_{ml_z\sigma}\sigma d^{\dagger}_{ml_z\sigma} d_{ml_z\sigma}$ and the total angular momentum $L_z = \sum_{ml_z} l_z\hat{n}_{ml_z}$. Therefore the operators are expressed in the subspace of fixed energy E and particle number N by using the projection operator $\mathcal{P}_{NE} = \sum_{L_z S S_z}|NE, SS_zL_z\rangle\langle NE, SS_zL_z|$. With $d^{\dagger}_{\alpha\sigma} = \sum_{ml_z} e^{il_z\Phi^m_{\alpha}} d^{\dagger}_{ml_z\sigma}$ the tunneling Liouvillian $\mathcal{L}_{tun} = \sum_{\alpha} = \mathcal{L}_{tun,\alpha}$ is defined as

$$\begin{aligned}\mathcal{L}_{tun,\alpha}\rho^{NE} = \Gamma_{\alpha}\sum_{E'\sigma}\mathcal{P}_{NE}\Big(& f^-_{\alpha}(E'-E)d_{\alpha\sigma}\rho^{N+1,E'}d^{\dagger}_{\alpha\sigma} - \frac{1}{2}f^-_{\alpha}(E-E')\left\{d^{\dagger}_{\alpha\sigma}\mathcal{P}_{N+1,E'}d_{\alpha\sigma}, \rho^{NE}\right\} \\ &+ f^+_{\alpha}(E-E')d^{\dagger}_{\alpha\sigma}\rho^{N-1,E'}d_{\alpha\sigma} - \frac{1}{2}f^+_{\alpha}(E'-E)\left\{d_{\alpha\sigma}\mathcal{P}_{N-1,E'}d^{\dagger}_{\alpha\sigma}, \rho^{NE}\right\}\Big)\mathcal{P}_{NE},\end{aligned} \tag{2.66}$$

where E' is the set of energies of $N \pm 1$ electrons and $\Gamma_{\alpha} = 2\pi|t_{\alpha}|^2 D_{\alpha}/\hbar$ are the single electron tunneling rates with the density of states at the Fermi energy D_{α}. The Fermi functions $f^{\pm}_{\alpha}$ are defined as $f^{+}_{\alpha}(\Delta E) = 1/[1 + \exp(\Delta E - \mu_{\alpha})/k_B T]$ and $f^-_{\alpha} = 1 - f^+_{\alpha}$.
The relaxation Liouvillian

$$\mathcal{L}_{rel}\rho^{NE} = -\Gamma_{rel}\left(\rho^{NE} - \rho^{NE}_{th}\mathrm{Tr}_N\rho^{NE}\right), \tag{2.67}$$

where Γ_{rel} is the relaxation rate and $\rho^{NE}_{th} = e^{-E/k_BT}/\left(\sum_{E'\in N} e^{-E'/k_BT}\right)$ is the thermal solution, leaves the particle number unchanged and is employed for numerical stability.
The current is then calculated as

$$I_{\alpha} = -e\mathrm{Tr}_{CNT}\hat{N}\mathcal{L}_{tun,\alpha}\rho^{\infty}. \tag{2.68}$$

Due to the orbital degeneracy the off-diagonal terms of the reduced density matrix have to be taken into account.

2.5 Noise

Noise is defined as the spontaneous and random fluctuations in time of a physical quantity around its mean value. For electrical systems, noise can be extrinsic or intrinsic. The former is generated by disturbances in the environment. It therefore does not carry information about the system and must be reduced as much as possible. Intrinsic noise instead depends on the characteristics of the transport process and is therefore an important tool to investigate the electronic properties of mesoscopic devices [12]. Combining conductance and noise measurements helps to gather more information about the charge and the statistics of the carriers involved in transport [12,13,62,63]. The deviations from the average current value $\Delta I(t) = I(t) - \langle I \rangle$ are called *current noise*. To characterize the noise one can define a current-current autocorrelation function

$$C(t) \equiv \langle \Delta I(t+t_0) \Delta I(t_0) \rangle \tag{2.69}$$

and its Fourier transform

$$S_I = \int_{-\infty}^{+\infty} \mathrm{d}t e^{i\omega t} C(t) = \int_{-\infty}^{+\infty} \mathrm{d}t e^{i\omega t} \langle \Delta I(t+t_0) \Delta I(t_0) \rangle. \tag{2.70}$$

This, so-called *power spectral density* (PSD), is the noise power per units of frequency. In the classical case the correlation function is symmetric in time $C(t) = C(-t)$ and therefore the PSD is symmetric in frequency $S_I(\omega) = I_I(-\omega)$. The symmetrized spectrum

$$S_I^{sym}(\omega) = S_I(\omega) + S_I(-\omega) = 2 \int_{-\infty}^{+\infty} \mathrm{d}t e^{i\omega t} C(t) \tag{2.71}$$

is the quantity detected in standard, low frequency noise measurements. In the quantum limit ($\hbar\omega \gg k_B T$), which will be discussed later, the spectrum is no longer symmetric $S_I(\omega) \neq S_I(-\omega)$ and therefore the classical description is not valid.

There are several mechanisms which cause noise in mesoscopic devices. Depending on the relation between thermal energy $k_B T$, the energy eV provided by the bias voltage and the photon energy $\hbar\omega$, which depends on the frequency at which the noise is measured, different noise mechanisms are dominant. In the following section the most relevant sources of noise are discussed [64,65].

2.5.1 Noise Sources

Thermal Noise

At finite temperature thermal fluctuations in the occupation number of the contacts lead to current and voltage fluctuation in the device in equilibrium ($V_{bias} = 0$). The first reports on this sort of noise were done experimentally by J.B. Johnson [66] and theoretically by H. Nyquist [67], therefore thermal noise is also called *Nyquist-Johnson noise*.
This is the dominant source of noise in the limit $k_B T \gg eV, \hbar\omega$. The power spectrum of thermal noise is frequency independent (white) up to the quantum limit $\omega = k_B T/\hbar$. The noise power magnitude is directly proportional to the conductance G of the system and is given by the *Nyquist-Johnson relation*:

$$S_I = 4k_B T G. \tag{2.72}$$

Equation 2.72 shows that besides the proportionality to the temperature and sample conductance, thermal noise does not contain additional information about the system besides what is already known from transport measurements. However it can be used for calibrating noise amplifier systems.

1/f Noise

These current fluctuations in the low frequency regime are found in most conducting materials and are caused by slow changes in the device resistance. This noise is proportional to the square of the injected DC current and decays inversely with the frequency, therefore the name *1/f noise*. No universal mechanism exists for the 1/f noise although many studies are available. At low frequencies 1/f noise is the dominant source of noise but is strongly suppressed for increasing frequencies. To neglect the influence of 1/f noise, the measurement frequencies in this thesis were chosen to be in the MHz regime. An extensive review of 1/f noise and other sorts of fluctuations in conductors are presented in [68].

Shot Noise

When out of equilibrium ($V_{bias} \neq 0$) current is passed through a conductor, charge carriers are transmitted or reflected randomly. This leads to fluctuations of this current (*shot noise* or *partition noise*) and is a consequence of charge quantization. This phenomenon was first described by W. Schottky [69] and is the dominant source of noise for $eV \gg k_B T, \hbar\omega$. The power spectrum is frequency independent (white).

An incident beam of n charge quanta, which is divided in a reflected and a transmitted beam by a barrier, can be described by a standard binominal distribution

$$P = \binom{n}{n_\Gamma} n_\Gamma \Gamma^{n_\Gamma}(1-\Gamma)^{n-n_\Gamma}, \tag{2.73}$$

where Γ is the transmission probability. The average number of transmitted charge quanta n_Γ is then

$$\langle n_\Gamma \rangle = n\Gamma. \tag{2.74}$$

The variance of the number of transmitted particles can be written as

$$\langle \Delta n_\Gamma^2 \rangle = \langle n_\Gamma^2 \rangle - \langle \Delta n_\Gamma \rangle^2 = n\Gamma(1-\Gamma) = \langle n_\Gamma \rangle (1-\Gamma). \tag{2.75}$$

The average current $\langle I \rangle$ is defined as

$$\langle I \rangle = q\frac{d}{dt}\langle n_\Gamma \rangle, \tag{2.76}$$

where q is the charge of the particles. Since the power spectral density S_I is proportional to the variance of the current ($S_I \propto \langle \Delta I \rangle^2$), shot noise can be described by the relation [12]:

$$S_I = 2e\langle I \rangle (1-\Gamma), \tag{2.77}$$

with e as the electron charge. For a small transmission probability ($\Gamma \rightarrow 0$) the transfer of electrons is uncorrelated and obeys the Poissonian distribution. In this *Poissonian limit* Eq. 2.77 is simplified to the *Schottky formula* [69]:

$$S_I = 2e\langle I \rangle. \tag{2.78}$$

Interactions in mesoscopic systems can introduce correlations between the charge carriers, which leads to a suppression or enhancement of the shot noise with respect to the Poissonian limit. Deviations from this limit are accounted by the *Fano factor*

$$F = \frac{S_I}{2e\langle I \rangle}, \tag{2.79}$$

which was introduced by U. Fano [70]. At zero temperature ballistic transport, where no scattering takes place, is noiseless. For instance in open quantum point contact devices (QPC) where each 1D subband provides $2e^2/h$ units of conductance, $\Gamma \rightarrow 1$ and S vanishes due to the $1-\Gamma$ term in Eq. 2.77 [71–73]. Quantum dot devices with a double barrier structure can also suppress noise, when the transport is dominated by Coulomb blockade [74–77]. Here the Fano factor is reduced to $F = \frac{1}{2}$, whereas in disordered wires it becomes $F = \frac{1}{3}$ [78, 79]. There are also circumstances in which the Fano factor is increased ($F > 1$). This *super Poissonian noise* can be a result of blocked channels which release more than one charge quantum in bundles or avalanche-like [80]. A possible cause for such blocked channels can be the Frank-Condon blockade [64].

Shot noise measurements can also give information about the nature of charge carriers in systems where current is not carried in units of electron charge. In the fractional quantum Hall regime shot noise measurements showed fractional charges corresponding to the quasiparticles [81, 82], whereas in superconducting systems noise was enhanced by a factor 2, attributed to the effective charge of Cooper pairs $q = 2e$ [83, 84].

Quantum Noise

In the limit of high frequencies ($\hbar\omega \gg k_B T$) zero point fluctuations make the noise spectrum asymmetric: $S(\omega) \neq S(-\omega)$. Emitted and absorbed noise are therefore different and the symmetrized approach, used for the other sources of noise, is no longer valid. A detailed discussion of quantum noise is beyond the scope of this thesis, since the performed measurements use frequencies of $f \sim 2$ MHz and the threshold for quantum noise is $f \geq 400$ MHz for a temperature of T = 25 mK. References [65, 85] give a deeper introduction to quantum noise.

2.5.2 Noise Measurement Techniques

Several existing setups for shot noise measurements will be discussed in this section, since the best noise detection technique varies depending on the setup, sample and the physical effects one wants to investigate.

Low Frequency Cross-Correlation Technique

Although current fluctuations of a sample $S_I = \langle \Delta I_S^2 \rangle$ is the desired quantity in shot noise measurements, since it directly provides information of the Fano factor (cf. Eq. 2.79), it is easier to derive S_I from the voltage fluctuations $S_V = \langle \Delta V_S^2 \rangle$. S_V is measured by using low noise voltage amplifiers and reading out the signal with a spectrum analyzer. The differential resistance $R_S = dV/dI$ of the sample is then used to convert the voltage power spectral density to current power spectral density $\langle \Delta V_S^2 \rangle = R_S^2 \cdot \langle \Delta I_S^2 \rangle$. In a setup, as sketched in Fig. 2.15, the spectral density of the total voltage fluctuations in a certain bandwidth Δf also includes current and voltage noise generated at the input of the amplifier $\langle\Delta I_A^2\rangle, \langle\Delta V_A^2\rangle$. Therefore the total voltage noise is expressed as

$$\langle V^2\rangle = \langle\Delta V_S^2\rangle + (R_S + R_L)^2\langle\Delta I_A^2\rangle + \langle\Delta V_A^2\rangle + 4R_L k_B T_L \Delta f, \tag{2.80}$$

where R_L and T_L is the resistance and the temperature of the leads, respectively. A precise determination of the noise generated from the sample requires an exact knowledge of all the other quantities of Eq. 2.80. Especially the temperature of the leads is hard to determine and the stability of the components is important for long acquisition times.

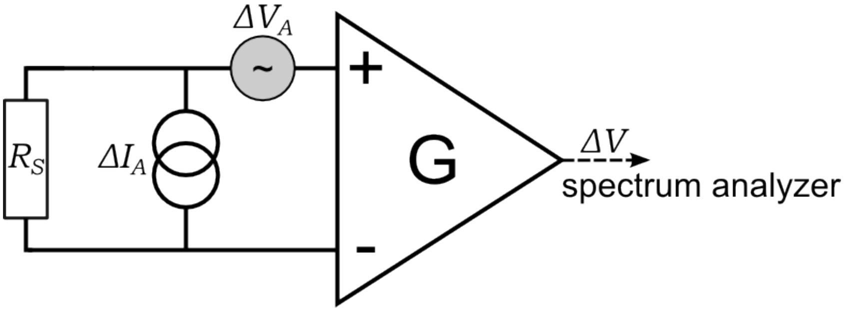

Figure 2.15: Noise measurement setup with a single amplifier. The resistor R_S generates current noise ΔI_A which is detected as voltage fluctuations ΔV_A across the resistor. These fluctuations are amplified by a voltage amplifier giving an output voltage ΔV.

These problems can be circumvented by using a cross-correlation method [13,86]. Two independent channels and voltage amplifiers are used to measure the same source of noise in parallel. These two signals are then multiplied eliminating uncorrelated contributions like the voltage noise of the amplifiers or the thermal noise of the leads:

$$\langle\Delta V_a \Delta V_b\rangle = \langle\Delta V_S^2\rangle + R_S(R_S + R_a)^2\langle\Delta I_a^2\rangle + R_S(R_S + R_b)^2\langle\Delta I_b^2\rangle. \tag{2.81}$$

A possible cross correlation setup is sketched in Fig. 2.16.
An initial calibration is needed to determine the current noise of the amplifier and the exact gain of the complete measurement circuit. Since current noise of an amplifier usually does not contain 1/f-noise [13], this setup is suitable for lower frequencies. However there is an upper frequency limit of $f_{max} = \frac{1}{2\pi RC}$, set by the combination of cable capacitances, filters, resistors, input capacitances of the amplifiers etc., which usually is in the range of several hundreds of kHz.

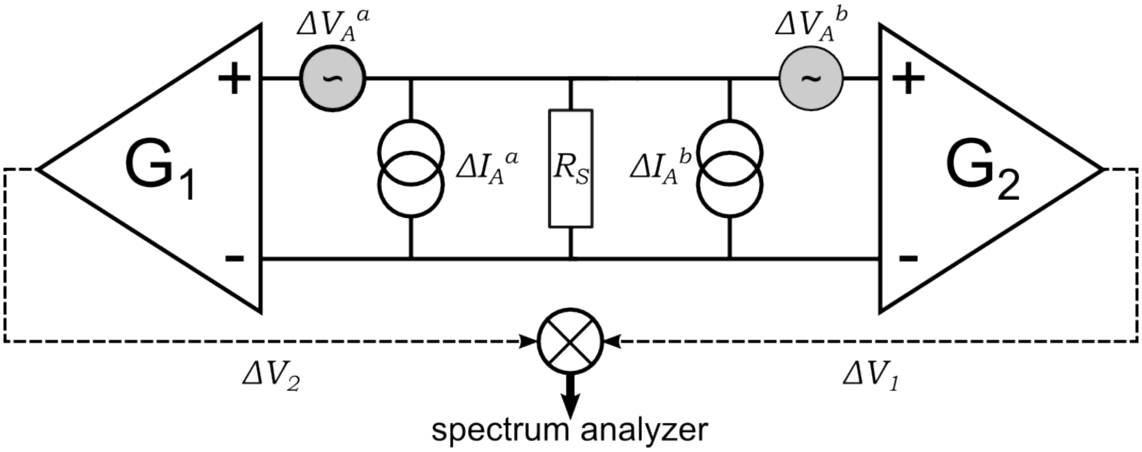

Figure 2.16: Noise measurement setup with two independent amplifiers connected in parallel to the same source of noise R_S. The amplified voltage signals ΔV_1 and ΔV_2 are sent to a spectrum analyzer. There the cross correlation of both signals is calculated, which cancels out differences of the two signals, like the intrinsic noise from the amplifiers and the leads. Therefore this setup yields a much cleaner signal than the single amplifier setup.

Resonant Scheme at MHz Frequencies

To perform measurements in the range of MHz a modified detection scheme like that presented in Ref. [72, 81, 87–90] can be used. The core principle of these setups is a RLC circuit formed by an inductance parallel to the capacitance of the coaxial measurement lines and the sample resistance. The impedance of the RLC circuit transforms current fluctuations of the device into voltage fluctuations at resonance frequency $f_{res} = \frac{1}{2\pi\sqrt{LC}}$. This voltage noise is proportional to the amplitude of the resonance peak. Figure 2.17 shows an exemplary setup where the amplification chain is divided in two parts. At low temperatures a FET is used as a preamplifier before the signal gets amplified again at room temperature. Since the noise characteristics of the cryogenic FETs are equal to those of room temperature amplifiers, the advantage of using two amplifiers is the reduced distance between the first amplification stage and the sample. This increases the applicable bandwidth for the measurement [13]. The resolution of these systems can be further increased by adding a second amplification chain and measuring the noise in a cross-correlation setup. Two independent amplification circuits are necessary if one wants to measure cross-correlation between different terminals [89, 91].

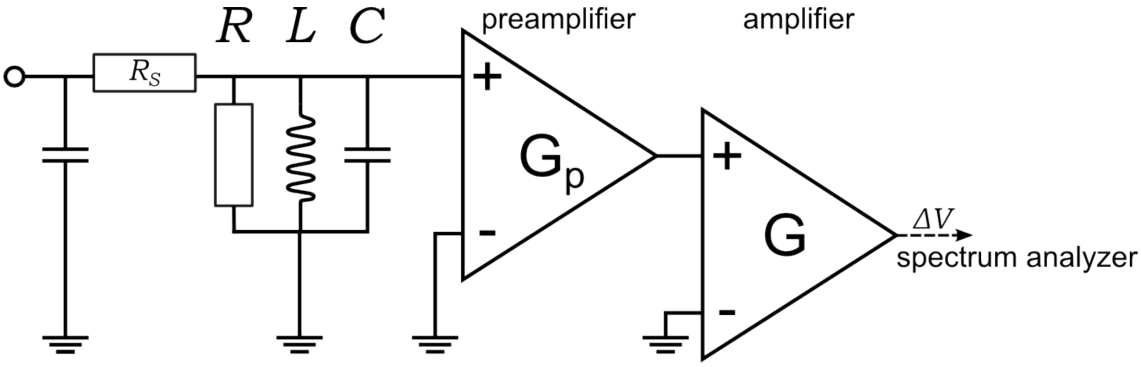

Figure 2.17: Setup using a resonant scheme for noise detection. Connecting a RLC circuit to the source of noise R_S confines the frequency independent noise to a Lorentzian shaped resonance curve which is determined by the components of the RLC circuit. The signal has its maximum at the resonance frequency $f_{res} = 1/2\pi\sqrt{LC}$. At f_{res} the impedance of the RLC circuit converts current noise S_I to voltage noise S_V which is amplified by a voltage amplifier. The signal-to-noise ratio can be increased by splitting the amplification chain into a preamplifier, located at low temperatures close to the sample, and a second amplifier outside the cryostat.

2.6 Nanoelectromechanical Properties of CNTs

In nanoelectromechanical systems (NEMS), the mechanical motion of an object influences its electrical properties and vice versa [92]. They can be used to study the fundamental limit of mechanical motions [93,94]. Due to their low mass, high stiffness and small cross-section, as well as their electronic properties, single-walled carbon nanotubes present ideal NEMS [95]. In the following section the different kinds of mechanical modes in suspended CNTs are presented and their influence on the electronic transport is discussed.

2.6.1 Mechanical Vibrations in Suspended Carbon Nanotubes

Carbon nanotubes, which are clamped on both ends, have several mechanical modes, which are briefly discussed in this section. The coupling strength between the electronic and the mechanical system can be characterized by a dimensionless parameter

$$g = \lambda^2 = \frac{1}{2}\left(\frac{x}{x_0}\right)^2. \tag{2.82}$$

Here x describes the shift of the ground-state position induced by adding one elementary charge and x_0 is the zero-point motion of the mechanical oscillator [96]. This parameter is referred to as *electron-vibron coupling constant*, *electron-phonon*

coupling constant or simply *coupling constant*.
An overview about the energies and corresponding length dependencies of the mechanical modes is given in Fig. 2.18.

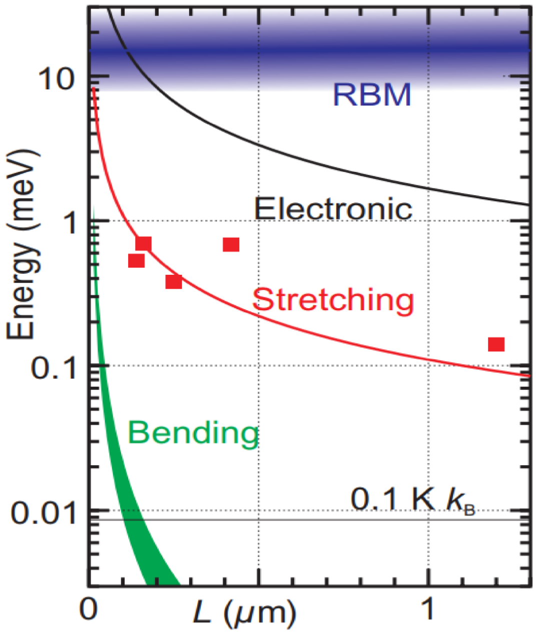

Figure 2.18: Energies for different vibration modes in dependence of the CNT resonator length L. The blue region indicates the length independent radial breathing mode. The longitudinal stretching mode (red line) scales with $\propto 1/L$, while the bending mode (green line) scales with $\propto 1/L^2$. The thermal energy in dilution refrigerators at T = 100 mK is indicated by the gray line. Taken from [96].

Radial Breathing Modes

The radial breathing modes of CNTs correspond to optical phonon branches. The tube diameter is expanding and shrinking around the equilibrium position, as depicted in Fig. 2.19a. Since their energy depends only on the tube radius and not its length, the breathing modes are used to identify the chirality of individual tubes with Raman spectroscopy [97, 98]. They were also probed in electronic transport by injecting current with a scanning electron microscope tip [99]. Their typical energy is around $hf_{breath} \simeq 10$ meV and the coupling constant $\lambda_{breath} \simeq 7 \cdot 10^{-2}/\sqrt{L[\mu\mathrm{m}]}$ depends on the tube length and is less sample specific [100].

Longitudinal Stretching Modes

The stretching modes describe the vibration of the CNT in axial direction, as depicted in Fig. 2.19b. Their vibration energy has a length dependence $\propto 1/L$. It typically lies between 0.1 meV $\leq hf_{stretch} \leq$ 1 meV for device sizes between 100 nm and 1 µm. In transport measurements these modes were observed as equidistant excitation lines [16, 49, 95, 101, 102]. The electron-vibron coupling for these modes varies strongly for different samples. It not only depends on the nanotube circumference, but also on size and location of the quantum dot, which is generally not related to the overall CNT length. For very clean CNTs the quantum dot size and the nanotube length coincide. The coupling constant can then be estimated as

$$\lambda_{stretch,clean} \simeq -\delta_{m,2n}\frac{1.5}{\sqrt{mL_{\perp}[\mathrm{nm}]}}, \tag{2.83}$$

where m is an integer wave number, n is the vibration mode and $L_{\perp}$ is the tube circumference [100]. The maximal coupling can be reached if the quantum dot lies in regions of the maximal strain in the tube. The coupling constant can be expressed as

$$\lambda_{stretch,max} \simeq \frac{3}{\sqrt{mL_{\perp}[\mathrm{nm}]}}. \tag{2.84}$$

For CNTs with small circumferences the coupling can become quite large.

Bending Modes

The bending modes are the energetically lowest mechanical excitations. Here the tube vibrates like a guitar string between the two contacts (cf. Fig. 2.19c). The vibration frequencies extend from 10 to 1000 MHz, depending on the length of the resonator with $\propto 1/L^2$ and on the mechanical tension. This corresponds to energies in the range of 1 to 1000 µeV. The frequency for a tube without tension is given by

$$f_{bend} = \frac{22.4}{2\pi}\frac{R}{2L^2}\sqrt{\frac{Y}{\rho}}, \tag{2.85}$$

where R is the tube radius, ρ the tube mass per volume unit and Y is the Youngs modulus, which is estimated to be 1 TPa [102,103]. The electron-vibron coupling is dependent on both the length L and the circumference $L_{\perp}$ of the carbon nanotube, as well as the quantum dot localization. The maximum coupling constant for the bending mode is given by

$$\lambda_{bend} \simeq \frac{40}{m^2}\frac{L[\mu\mathrm{m}]}{L_\perp^3[\mathrm{nm}]} \tag{2.86}$$

for the first bending mode and

$$\lambda_{bend} \simeq 10^{-4}\frac{n^2+1}{n^4}\frac{L_\perp[\mathrm{nm}]}{L[\mu\mathrm{m}]} \tag{2.87}$$

for higher modes with $n \geq 2$ [100].

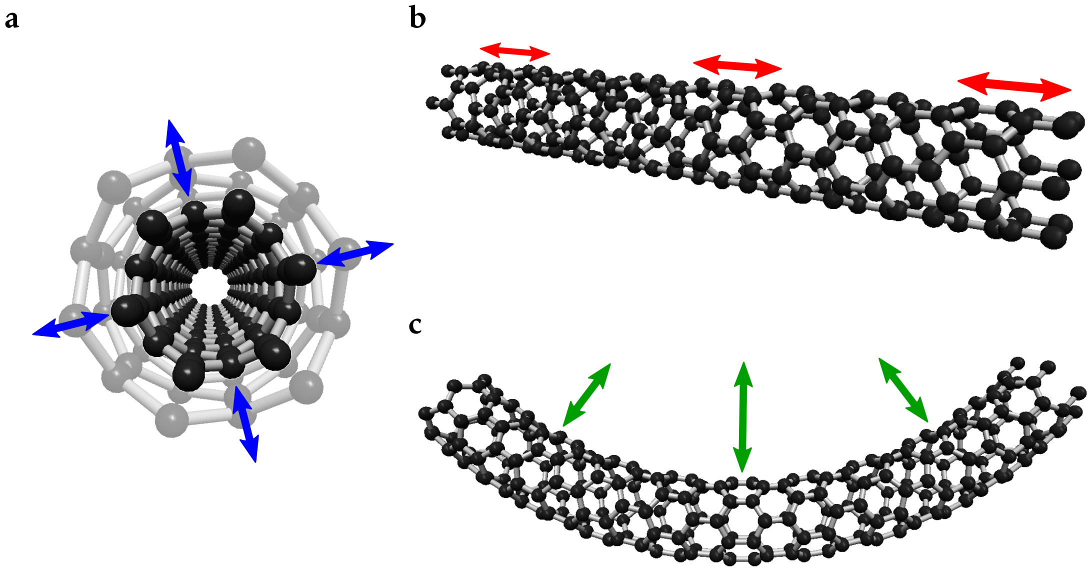

Figure 2.19: Sketch of different vibration modes of a carbon nanotube: **a** radial breathing mode, **b** longitudinal stretching mode, **c** bending mode. Created with *Nanotube Modeler 1.7.8.*(©JCrystalSoft 2015)

2.6.2 Effects of Vibration Modes on Electronic Transport

Performing transport measurements on suspended carbon nanotubes, effects of the mechanical modes become visible. In the following section the observed phenomena contributed to the mechanical modes are briefly discussed.

Vibrational Sidebands

For strong electron-vibron coupling ($g = \lambda^2 \geq 1$) additional excitation lines, parallel to the Coulomb diamond edges, appear in the stability diagram [16, 49, 101, 104, 105]. Their spacing is equidistant and about a magnitude smaller than the electronic level spacing of the CNT. In carbon nanotube quantum dots, these lines correspond to the excitation of vibration quanta of the longitudinal stretching mode, since the energy of the bending mode is too low to be resolved and the energy of the radial breathing mode is higher than the electronic level spacing (cf. Fig. 2.18). The occurrence of negative differential conductance between the vibration excitation lines, which was observed in [49, 64, 106] and theoretically explained by [107–109], is another indicator for the vibrational origin of those excitation lines. The Franck-Condon model can describe the coupling of the electronic levels with the vibrational modes. The principle, which was discovered by James Franck [110] and later theoretically described by Edward Condon [111], states that the electronic transitions happen much faster than the movement of the nuclei. Therefore the nuclear positions are the same before and after the electronic transition. In Fig. 2.20 the Franck-Condon principle is illustrated. The two parabolic potentials represent the effective nuclear potentials for two electronic states N and $N+1$. The ratio between the lateral displacement length of the potentials x and the quantum mechanical oscillator length $x_0 = \sqrt{\hbar/m\omega}$ is given by the electron-phonon coupling constant

$$g = \frac{1}{2}\left(\frac{x}{x_0}\right)^2. \tag{2.88}$$

The transition rates are proportional to the Franck-Condon factors, which are defined as the square of the overlap integral between the wave functions of the two vibration states [49]. The equidistant excitation lines correspond to steps in the current. For low damping of the oscillator, the current steps are equally spaced in energy, while for strong relaxation the normalized step heights are given by a Poissonian distribution [104]

$$P_n = \frac{e^{-g} g^n}{n!}, \tag{2.89}$$

where n is the number of the vibration mode and g the electron-vibron coupling.

Franck-Condon Blockade

The current suppression at low bias voltages in systems with a strong electron-vibron coupling is called Franck-Condon blockade and is a direct consequence of Eq. 2.89. For $g \gg 1$ the current step heights become very small for low vibration modes [112, 113]. This effect can also be visualized by the lateral displacement of the potentials, as depicted in Fig. 2.20. The more the two electronic levels

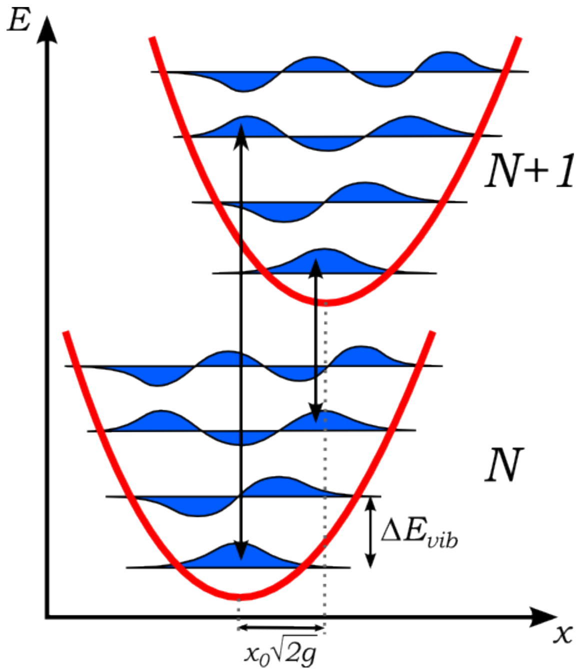

Figure 2.20: Visualization of the Franck-Condon principle: The vibrational modes of a quantum harmonic oscillator have an energy separation of $\Delta E_{vib} = \hbar\omega$. The probability for a transition between two electronic levels N and $N+1$ is given by the square integral of the overlapping wave functions. This leads to multiple steps in the current. The electron-vibron coupling is illustrated by the displacement of the two parabolas. In case of strong coupling, the lower wave functions have no overlap, which causes a suppression of current at low bias. This is called the Franck-Condon blockade.

are shifted from one another, the smaller the overlap of the wave functions and therefore the smaller the transition probability gets. The effect is strongly dependent on the electron-vibron coupling constant g. For $g \approx 1$, no current suppression was observed [49], while for $g \approx 4$ the Franck-Condon blockade was clearly visible [114]. In this transport regime, the current noise is supposed to be extremely large compared to the Poissonian shot noise, resulting in Fano factors in the order of $10^2 - 10^3$ [112]. This is due to an avalanche-like transport of electrons, which is interrupted by long times without charge transfer. These transferless phases are due to the suppressed transition rates for low vibron modes in the Franck-Condon blockage regime. The Fano factor can be estimated by the number of electrons transmitted during such an avalanche. In systems without electron-vibron coupling, the Fano factor is supposed to be below the Poissonian value [115,116].

Nanomechanical Current Blockade

The bending mode of the carbon nanotube changes the distance between the quantum dot and the gate electrode, as depicted in Fig. 2.21a, which modifies the gate capacitance. In the regime of strong electron-vibron coupling, this change of the capacitance can lead to a current blockade at the degeneracy point in the current voltage characteristics [96, 117]. The displacement of the average position leads to a shift of the gate voltage. The position of the Coulomb diamond changes with respect to the case of the undisplaced quantum dot. This is depicted in Fig. 2.21b. Here one can see that the displacement leads to an overlap of the regions where current is blocked by Coulomb blockade, opening a gap at the degeneracy point. At the border of the conducting region the current is continuously vanishing. It was observed in [106, 118] and can be seen as the classical counterpart of the Franck-Condon blockade [117].

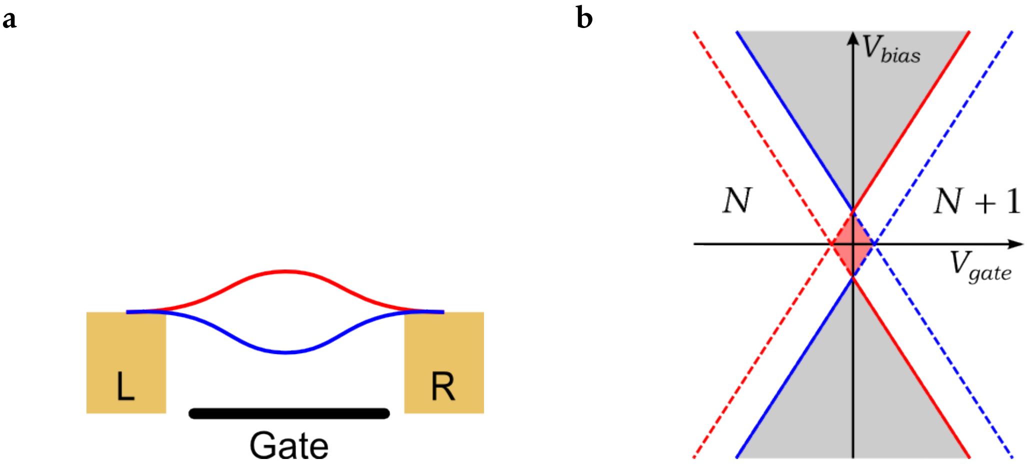

Figure 2.21: **a** Sketch of a carbon nanotube clamped on two contacts. The bending mode changes the distance between the quantum dot and the backgate. **b** This changes the gate capacity, which leads to a shift of the Coulomb diamonds in gate voltage. The current is therefore always blocked in the red area. Sketch adapted from [96, 117].

Current Modifications by Strong Feedback

The aforementioned effects occur in the limit of strong electron-vibron coupling ($g \gg 1$). But also in the weak coupling regime nanoelectromechanical systems can have a strong mechanical feedback [119]. The vibrating carbon nanotube can be assumed as a quantum dot, which is coupled to a mechanical oscillator with frequency ω_0, mass M and quality factor $Q \gg 1$ by a force F. Since the coupling is assumed to be weak, the parameter

$$\lambda \equiv F^2/\hbar M\omega_0^3 \ll 1 \tag{2.90}$$

must be smaller than one. The tunneling of electrons with the rate Γ produces a driving force on the oscillator. Many tunneling events happen during one oscillation period $\omega_0 \lesssim \Gamma$. Therefore the oscillator accumulates a typical energy

$$E \simeq \hbar\omega_0 Q\lambda(\omega_0/\Gamma). \tag{2.91}$$

For high quality factors, this leads to a oscillation amplitude

$$\zeta = \sqrt{\frac{2E}{M\omega_0^2}}, \tag{2.92}$$

which can get arbitrarily high. The tunneling rates are a function of the corresponding energy cost $\Delta E^{\pm}_{L,R}$ for adding (removing) an electron to (from) the quantum dot via the left ro right junction ($\Delta E^{+}_{L,R} = -\Delta E^{-}_{L,R}$) [120, 121]. These energy differences are affected by the x position of the oscillator

$$\Delta E^{+}_{L} = -W + W_L - Fx, \quad \Delta E^{-}_{R} = -W_R + W + Fx, \tag{2.93}$$

where the parameter W represents eV_{bias} and eV_{gate}. W_L and W_R are the boundaries of the Coulomb diamonds and $W_L < W < W_R$ lies in the transport region. The region in which the amplitude of the oscillator gives a strong feedback on the tunneling is defined by

$$W \lesssim F\zeta \simeq \hbar\omega_0\lambda\sqrt{\frac{Q\omega_0}{\Gamma}}. \tag{2.94}$$

The current noise in this region is estimated to be

$$S \simeq \frac{I^2 Q}{\omega_0} \simeq eI\frac{Q\Gamma}{\omega_0}, \tag{2.95}$$

which exceeds the Schottky value $S_P \simeq 2eI$ [119, 122]. The mechanical energy needed to modify the tunneling rates is given by

$$E \simeq M\omega_0^2\left(\frac{eV_{bias}}{F}\right)^2. \tag{2.96}$$

If the damping of the oscillator, which is determined by the tunneling rates only, becomes negative, the oscillation amplitude grows and becomes instable. The regions of different oscillation behavior are depicted in Fig. 2.22. In region (i) the

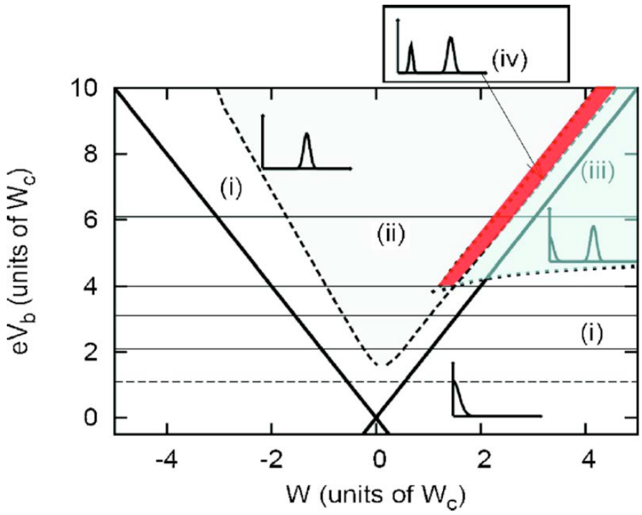

Figure 2.22: Four stability regions in the gate-bias voltage plane. (i) Positive damping, no strong mechanical feedback. (ii) Mechanical oscillations are generated. Bistability in region (iii) and (iv). Region (iii) can extend to the Coulomb diamond where no current flow should be possible. The insets show the probability distribution $P(E)$ in each region. Taken from [120].

damping is positive and the probability is maximal for $E = 0$. Strong mechanical feedback is present in regions (ii) - (iv). In region (ii) the oscillator has a finite amplitude. In region (iii) and (iv) there is a bistability of the system. It can either oscillate with two different amplitudes, like in region (iv), or switch between oscillating at a finite amplitude and no oscillation, as in region (iii). In that case, the generation of mechanical oscillation allows the system to be conducting even inside the otherwise blocked Coulomb diamonds. The bistability can lead to jumps in the current, when the probabilities of the two oscillation amplitudes are equal. The noise reaches its maximum near the current jumps and can be estimated by

$$\ln\left[\frac{S}{S_P}\frac{\hbar\omega_0\lambda}{W}\left(\frac{\omega_0}{\Gamma}\right)^2\right] \approx \frac{W}{\hbar\omega_0\lambda}. \tag{2.97}$$

3 Sample Fabrication and Experimental Setup

This chapter considers the necessary steps to produce and measure carbon nanotube quantum dots. At first the different fabrication processes, like lithography and carbon nanotube growth via CVD, are discussed. Then the experimental setup used to perform transport and Shot noise measurements is presented. Before the typical measurement routine is listed, the calibration measurement of the noise setup is shown.

3.1 Sample Fabrication

To obtain contamination-free, unperturbed single wall carbon nanotubes (SWCNTs), the CNT growth was performed as the last fabrication step [7]. With this technique, any contamination stemming from chemicals, used in the fabrication process as e.g. lithography resists, or amorphous carbon, deposited by scanning electron microscope (SEM) imaging, are avoided. In this section those fabrication steps are presented. It contains the preparation of the substrate material, the patterning of the contact structures by electron beam lithography (EBL), the metalization and finally the carbon nanotube growth via chemical vapor deposition (CVD). Detailed recipes of each process step are presented in App. A.

3.1.1 Substrate

For all experiments a highly boron doped (p++) silicon substrate with a thermally grown 500 nm thick oxide layer (SiO_2) was used. Due to the degenerate doping, the semiconducting silicon layer can be used as a global backgate even at very low temperatures (mK-range). Therefore the oxide layer is scratched away at a small region of the sample and the silicon is directly connected via bond wires.

3.1.2 Lithography and Metalization

After cleaning the surface of the substrate, a layer of PMMA is spun onto the chip, to define contact structures, leads and bondpads as well as alignment markers in one single electron beam lithography step. After developing the exposed structures the sample is metalized with e.g. titanium/platinum (Ti/Pt) afterwards. The chip is then put in hot acetone to remove the surplus metal on the undeveloped regions. The sample design is depicted in Fig. 3.1a-c. There are six squares with bondpads, each containing four ring-like contact structures. This structure (cf. Fig. 3.1c) consists of a 500 µm wide inner ring and four separate contacts with a width of 250 µm each. Since the CNT growth is arbitrary, this ring-like structure helps to get a higher chance of a CNT falling onto a contact pair and therefore increase the yield of working devices. There are 24 of these structures on a chip, which leads to a total amount of 96 contact pairs per sample. The distance between inner and outer contacts is 350 µm.

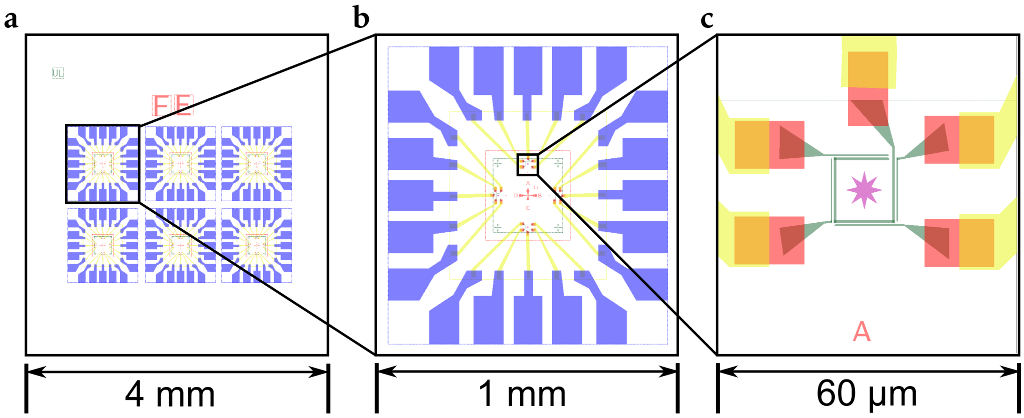

Figure 3.1: EBL design of sample structures: **a** 4 mm x 4 mm chip containing six squares with bondpads. **b** One square has four contact structures with five bondpads each. **c** Contact structure is built up by an inner ring connected to the middle bondpad and four separated electrodes.

3.1.3 CNT Growth

With the help of alignment markers, a second EBL step defines star shaped areas inside the ring-like contact structures, in which the catalyst is deposited. Therefore a two-layer PMMA mask is used to assure a large undercut. The exposed areas are developed and the sample is covered with a few drops of the catalyst suspension, using a pipette. For the exact composition of the suspension see

App. A.2.1. After a few seconds the chip is blown dry with N_2 and baked out at a hotplate at 150 °C for 5 minutes. A bath in 60 °C hot acetone removes the PMMA and leaves the catalyst dots. The actual carbon nanotube growth is a CVD process based on [123] and takes place in a quartz tube in a furnace heated up to 850 °C. Hydrogen and methane are used as process gases, which are fed into the furnace via mass flow controllers (MFCs) in order to control exactly the ratio between the two gases. The detailed recipe can be found in App. A.2.2. The methane decomposes at the catalyst and the carbon atoms crystallize, forming the CNT. It grows vertically until it tilts and falls onto the contacts and the substrate surface, where it is attached to via Van-der-Walls forces. To prevent a contamination with carbon, SEM imaging of the device is avoided. Therefore the electrical resistance between all 96 contact pairs needs to be measured to distinguish between the pairs connected by a CNT and the ones left open circuited. On the connected contact pairs a backgate-dependent measurement of the conductance is performed to identify the most promising devices. Those are then bonded and mounted into the cryostat system.

3.2 Experimental Setup

In this section the experimental setup, necessary for the performed measurements, is briefly presented. The first part describes the equipment used to reach low temperatures which are crucial to observe transport phenomena and suppress thermal noise, as explained in Ch. 2.3 and 2.5. The second part presents the electrical scheme used to carry out the transport and noise measurements.

3.2.1 Cryogenics

In order to reach sufficiently low temperatures a ^{3}He/^{4}He dilution refrigerator built by cryoconcept[1], which is shown in Fig. 3.2b was employed. In Fig. 3.2a the basic components of the dilution refrigerator are sketched.

The fundamental cooling mechanism is based on an incomplete phase transition between ^{3}He and ^{4}He for temperatures below $T \approx 870$ mK. Although the amount of ^{3}He in the ^{3}He-rich phase can become 100%, the concentration of ^{3}He in the heavy phase (^{4}He) cannot deceed 6.6%. Due to the higher vapor pressure, ^{3}He gas is pumped out of the still, cleaned in a nitrogen trap outside the cryostat and reentered through several heat exchangers. At about $T \approx 1.5$K, the ^{3}He gas condenses by e.g. a Joule-Thomson stage or a 1 K-pot. The now liquid ^{3}He enters

---

[1] http://www.cryoconcept.com

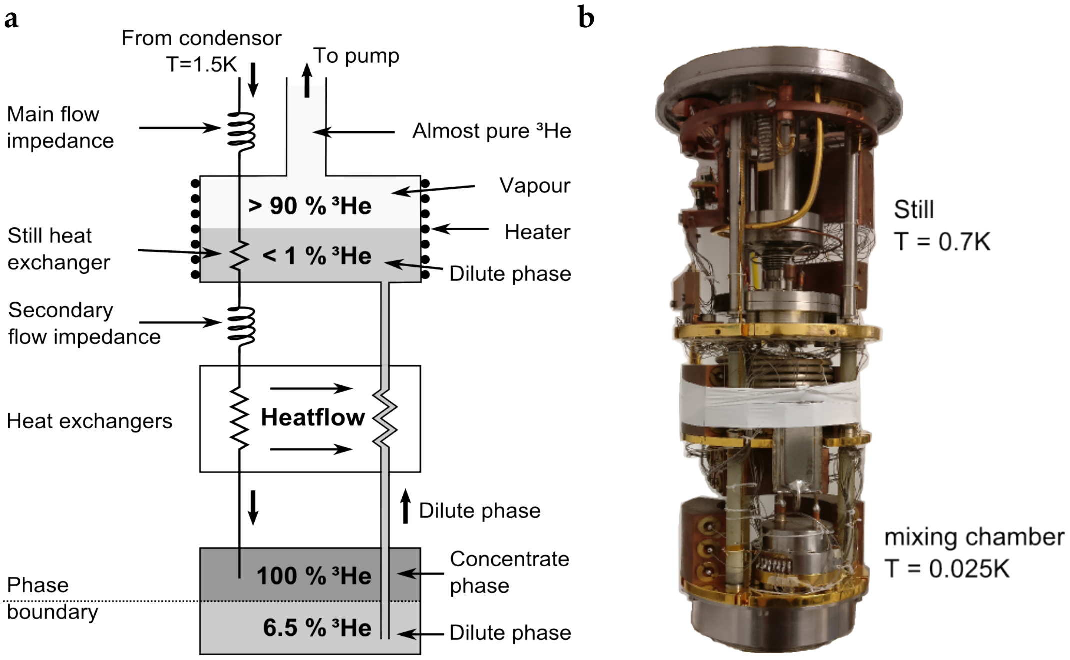

Figure 3.2: **a** Basic principle of a dilution refrigerator. Sketch adapted from [124]. **b** Photograph of the actual dilution refrigerator used in this work

through more heat exchangers and flow impedances the ^{3}He-rich phase in the mixing chamber. The return line, connecting the mixing chamber and the still, starts below the phase boundary in the heavy phase. Pumping of the still leads to an osmotic pressure which extracts ^{3}He from the dilute phase of the mixing chamber. Since the concentration of ^{3}He in ^{4}He cannot fall below 6.6%, ^{3}He from the concentrate phase is forced to make a phase transition. This process is endothermic, which leads to a cooling of the mixing chamber and therefore the sample. A more detailed description of the work mechanism of the dilution refrigerator and many other cooling techniques are presented in references [124–126].

The system used in this thesis reaches a base temperature of $T \approx 20$ mK.

3.2.2 Noise and Transport Measurement Setup

The setup used to perform transport and noise measurements simultaneously was mainly taken over from the work of Daniel Steininger. In his thesis [64] he describes in detail the construction of the cryogenic amplifier setup, inspired by experiments of other groups [78, 87–90, 127]. It was designed to measure noise in Cooper pair beam splitter devices, therefore two amplifier circuits, each for every quantum dot, were needed. Since only single quantum dot devices were investigated in this thesis, the setup was adjusted. With two amplifier setups there is the possibility to perform cross correlation experiments [90], which increase the noise resolution by canceling out unwanted noise from the amplifier themselves, or simply increase the number of samples per cooldown, on which it is possible to perform measurements. Since the low yield of satisfactory samples and the long preparation times needed to reach low temperatures, the latter option was chosen. Another change in the setup was the redesign of the sample holder. Previously a custom-built printed circuit board (PCB) with included RLC circuits was used, which made changing and especially bonding samples rather difficult. Therefore we switched to a standard 20 pin chip carrier and designed a PCB which fits to the sample holder, as depicted in Fig. 3.3.

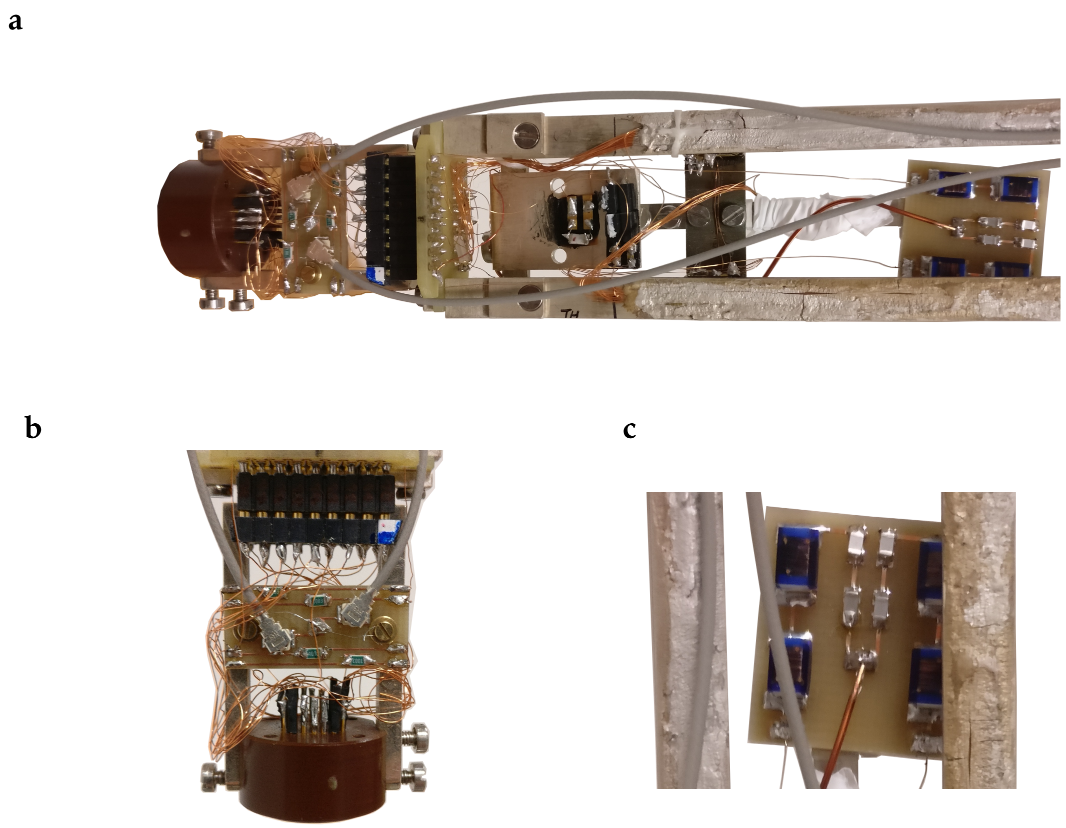

Figure 3.3: **a** Redesigned sample holder with standard 20 pin chip carrier. RLC circuit is printed on two PCB boards. **b** Close up of the first PCB board which contains the resistances in series to the sample and the coaxial measurement lines. **c** The second PCB board contains the inductors and capacitors, defining the resonance frequency $f_{res} = \frac{1}{2\pi\sqrt{LC}}$ at ≈ 1.9 MHz.

The whole measurement setup used in this work is depicted in Fig. 3.4. On one contact (source contact) a dc bias voltage from a dc voltage source, as well as a small ac voltage of about 10 µV from the signal output of a lock-in amplifier are applied. Both voltages are looped through a double voltage divider, with different divisions for the ac (1:1000) and dc (1:100) voltage, π-filters and a pre-resistor. A current-to-voltage converter provides the sample ground to the drain contact via the same filtering as used for the source line. There the sample current is converted into a voltage, whose ac and dc part are measured by the lock-in amplifier and a multimeter The cryo-amplifier chain necessary for the noise measurements is also connected to the drain contact. It consists of three parts located at different temperatures.

- **RLC-circuit**
  The resonant circuit is located next to the sample holder and therefore has the same temperature as the sample. The resonance frequency $f_{res} = \frac{1}{2\pi\sqrt{LC}} \approx 1.9$ MHz is given by the capacity and the inductance of the chosen components.

- **4K amplification stage**
  A field effect transistor is used to amplify the outgoing noise signal already at T = 4.2 K. Therefore it is connected to the helium bath via a sapphire chip, to assure a good thermal coupling while being electrically isolated. Resistors between the source contact and ground, as well as between the drain contact and ground set the FET in a self biasing mode with a fixed bias current $I_{\text{bias}} \approx 5.5$ mA. Therefore the input voltage signal on the gate contact is converted into fluctuations of the bias current.

- **frequency splitter**
  The frequency splitter box is mounted at room temperature on the outputs of the cryostat. It contains a circuit which splits the bias current fluctuations in a high and a low frequency part and allows to apply an external dc voltage to bias the FET. The output of the high frequency part is connected to a radio frequency (RF) amplifier before arriving at a spectrum analyzer which performs a Fourier transformation of the noise signal. The low frequency part can be connected to the input of a lock-in amplifier but in our case it was left unused.

The line connecting the global backgate is not depicted in Fig. 3.4 for clarity reasons. All measurement devices are connected via GPIB interface to a measurement PC. They are actuated by *Lab::Measurement*[2], which is a software stack using the programming language *Perl*[3]. The measurement sequence is structured by loops, written in simple scripts where the data is acquired, processed and written into files on the PC.

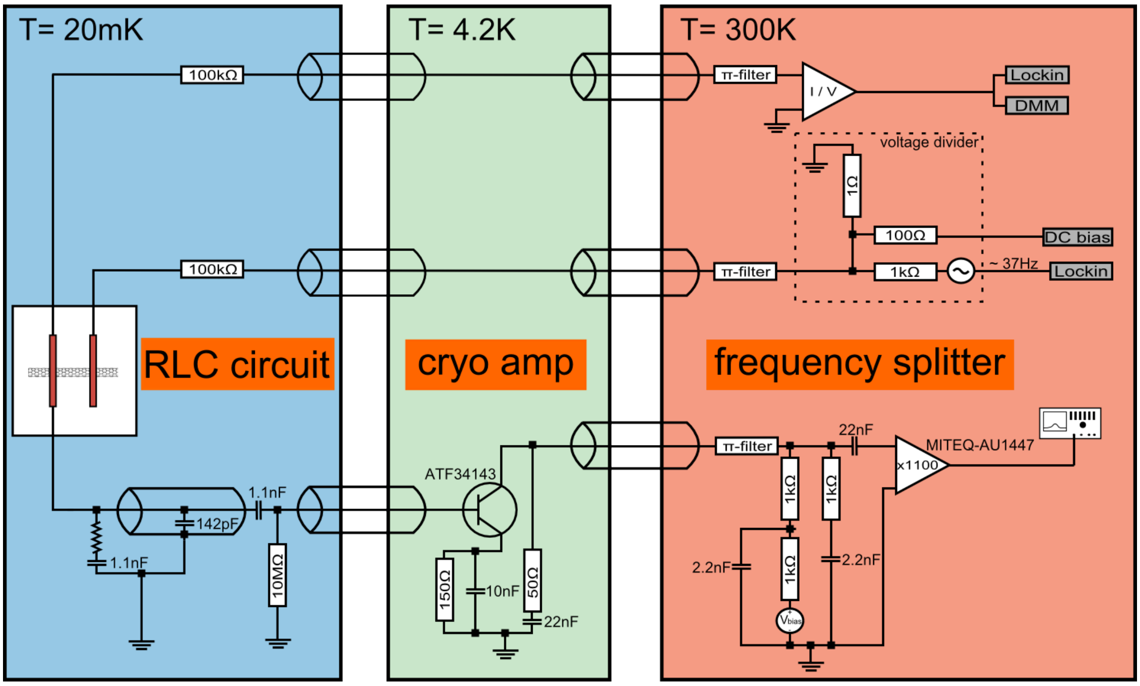

Figure 3.4: Basic sketch the measurement setup used in this work. It consists of a RLC circuit at base temperature, one amplification step at T = 4.2K and a second amplifier at room temperature. Adapted from [64].

3.2.3 Noise System Calibration

For noise measurements it is crucial to have very accurate values of the current noise in the sample since they are needed to calculate the Fano factor. Here small deviations in the measured noise can strongly influence the outcome and therefore the evaluation of the performed experiment. This is why, every time the system is altered, a careful calibration of the setup is needed. The redesigning of the sample holder, including the RLC-circuit board, gives cause to reperform a calibration measurement as done in Ref. [64].

For the calibration measurements a quantum point contact sample was used. A

---

[2] http://www.labmeasurement.de

[3] http://www.perl.org

split gate was patterned onto an AlGaAs/GaAs heterostructure[4], which contains a two dimensional electron gas (2DEG). By applying a negative voltage to the gate fingers, one can deplete the 2DEG beneath the split gate. This forms a conducting channel, whose width can be controlled by the applied voltage. By decreasing the width, the conductance decreases stepwise by units of the quantum conductance $G_0 = e^2/h$ until the conducting channel is completely pinched off and the conductance is zero [71]. Close to this pinch off point, where $T \rightarrow 0$, the Fano factor is supposed to be $F = 1.0$ [89].

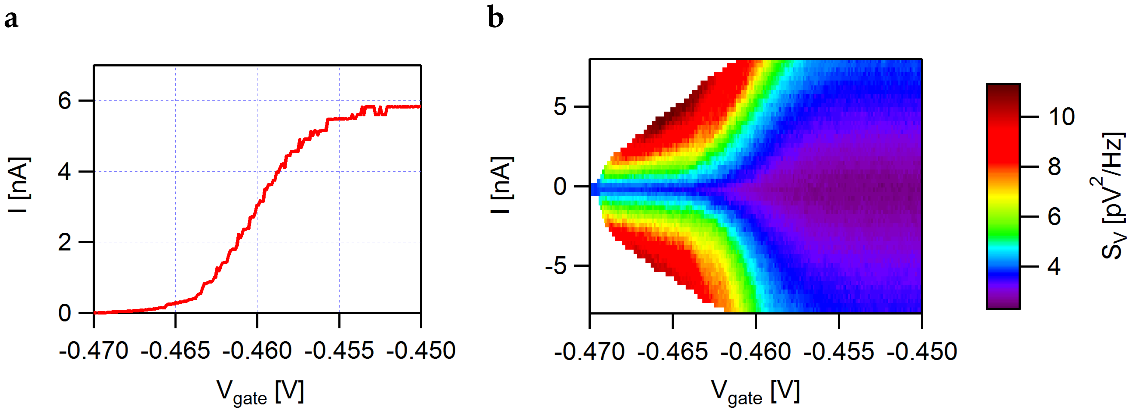

Figure 3.5: **a** Current versus gate voltage: Applying a negative gate voltage depletes the 2DEG and narrows the conducting channel. This leads to a decrease in the current. **b** Voltage noise versus current and gate voltage: Opening the conductance channel by reducing the gate voltage, the measured voltage noise decreases, as expected from Eq. 2.77.

In the following, only the calibration of the amplifier setup connected to the measurement lines 13 and 14 is shown. The calibration of the second noise setup (lines 8 and 9) was performed respectively. In Fig. 3.5a, the current through the QPC in dependence of the gate voltage at a fixed bias of $V_{bias} = 30$ µeV is shown[5]. Figure 3.5b shows the measured voltage noise S_V in dependence of current and gate voltage. The voltage noise shows a linear current dependence, which is depicted for different transmissions in Fig. 3.6. The maximum slope is observed close to the pinch off point at a gate voltage value of $V_{gate} = -0.48$ V. At this point it is assumed, that the Fano factor is $F = 1.0$ and therefore the voltage noise S_V to current noise S_I conversion factor $\alpha^2 g^2$ can be directly obtained by the slope of

---

[4] Heterostructure made by Dr. Dieter Schuh and patterned by Michaela Trottmann, chair of Prof. Dr. D. Bougeard.

[5] Calibration measurements performed by Christian Bäuml.

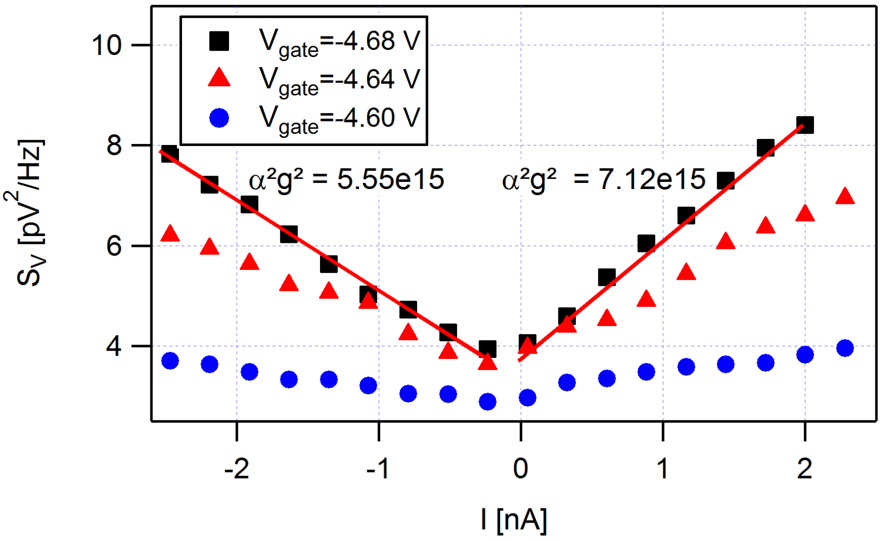

Figure 3.6: Voltage noise S_V versus current: Close to the pinch off point at $V_{gate} = 0.468$ V (black curve), the Fano factor is assumed to be $F = 1.0$ [89]. This allows a direct extraction of the conversion factor from S_V to S_I, following Eq. 3.1.

the $S_V(I)$ graph:

$$S_I = \frac{S_V}{\alpha^2 g^2} = 2e\langle I\rangle \cdot F. \tag{3.1}$$

Here g is the gain of the amplifier chain and α is the impedance of the RLC circuit.

Averaging over the slopes for positive and negative current values from the calibration measurement, a mean value for the conversion factor can be extracted. For the first noise setup (lines 13 and 14) one obtains

$$\mathrm{setup}_{13,14}: \quad \alpha^2 g^2 = 6.3 \times 10^{15}\Omega^2, \tag{3.2}$$

while for the second setup (lines 8 and 9) the value is

$$\mathrm{setup}_{8,9}: \quad \alpha^2 g^2 = 4.9 \times 10^{15}\Omega^2. \tag{3.3}$$

3.2.4 Measurement Routine

After the CNT growth, described in Ch. 3.1.3, resistance measurements at room temperature are performed on each of the 96 contact pairs by using a tip probe station. A bias voltage of 2 mV is applied on the contact pairs and the current through them is measured. If there is a finite resistance 50 kΩ ≤ R_S ≤ 500 kΩ a

CNT has shortened the contacts and the backgate dependence of the current is measured to identify the sort of CNT (e.g. metallic, small bandgap or semiconducting). The two most promising looking devices, usually low resistive small bandgap tubes, are bonded and the sample is mounted in the cryostat. Here the CNTs are checked again by measuring the current through the tubes, since they are easily destroyed by electrostatic charges. A last test is performed at liquid helium temperature $T = 4.2$ K before the sample is cooled further down to base temperature.

At first a gate sweep at zero bias is performed. This is needed to find regions of the gate voltage, where a bandgap or regular peaks in the differential conductance occur. The gate sweeps are performed in both directions to see if there is a strong gate hysteresis. If this is not the case, also the bias voltage is varied to get a stability diagram of the conductance. For this purpose the gate voltage is altered stepwise, while the bias voltage is swept continuously in one direction and back to the starting point. Differential conductance and current is only acquired in on sweep direction to avoid the hysteresis in the bias voltage. For the noise measurements, for each measurement point a noise spectrum is acquired. The spectrum analyzer has to integrate over many spectra for about ten seconds. In this time it is crucial that no communication via GPIB between the measurement devices or the PC takes places. Therefore waiting times had to be added to the measurement loop, which is briefly listed (adapted from [64]):

1. sweep gate voltage to starting value
2. sweep bias voltage to starting value
3. measure dc current/differential conductance from multimeter/lock-in and write to file
4. start averaging of spectrum analyzer
5. waiting time till averaging is finished (**no GBIP communication** during this time)
6. acquire complete noise spectrum from spectrum analyzer and write to file
7. increment bias voltage by one step
8. go back to step 3 until bias end value is reached
9. increment gate voltage by one step

10. go back to step 2 until gate end value is reached

11. measurement is finished

The resolution (step size) of the gate and bias voltage and the integration time of the spectrum analyzer, which sets the sensitivity of the noise setup, determine the measurement time:

$$t_{meas} \approx N_{gate} \cdot N_{bias} \cdot t_{int}$$

. This is just a rough estimation since the time needed for sweeping the bias to its start value is neglected. Since $\mathrm{t_{int}} = 10$ s, the measurement time can become longish. For instance a measurement with a resolution 200 points for gate as well as bias voltage will need more than 100 hours. Therefore artifacts in the measurement can occur due to refilling helium or temperature changes in the laboratory.

4

Dark States in Carbon Nanotube Quantum Dots

In this chapter the effect of destructive electron interference in a carbon nanotube single quantum dot is presented.
At first the sample is characterized extensively. The performed transport measurements reveal the presence of dark states. The results will be discussed and compared with numerical simulations[1].

4.1 Basic Sample Characterization

The investigated sample is a quantum dot, formed by a single walled carbon nanotube which is grown over a prepatterned contact structure on a SiO_2-capped p++ doped silicon chip. Figure 4.1 shows a colorized SEM image of a similar device.
The quantum dot is formed by the CNT segment which lies between the source and drain electrodes. They have a distance of 350 nm. On these contacts one can apply a bias voltage to change the chemical potentials of the source μ_s and drain μ_d. To alter the chemical potential of the quantum dot μ_{dot}, a voltage is applied to the conducting substrate which acts as a global backgate.

4.1.1 Contact Material

The electrode structure consists of a 20 nm Rhenium (Re) and 40 nm Cobalt (Co) bilayer. This material combination was originally chosen to perform TMR measurements on overgrown CNTs, since it should stay ferromagnetic after the CVD process of the nanotube growth [128]. However Magneto-Optic-Kerr-Effect (MOKE) measurements[2], which detect the change in polarization of a laser beam reflected from a magnetic surface, revealed that the surface of the contacts is

---

[1] Numerical simulations performed by Michael Niklas, chair of Prof. Dr. Milena Grifoni

[2] MOKE measurements performed by Tobias Weindler, chair of Prof. Dr. Christian Back

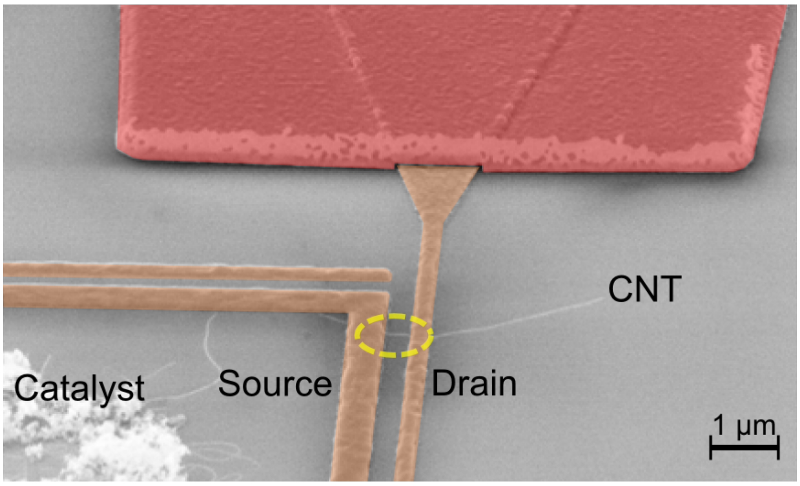

Figure 4.1: SEM picture of device structure: Catalyst is deposited in the middle of the ring-like source and drain contacts (orange). The yellow circle shows a CNT, grown over the pair of contacts and forming a quantum dot with a contact spacing of 350 nm.

no longer ferromagnetic after CVD (cf. Fig. 4.2) and also the transport measurements show no sign of ferromagnetic contacts. Thus the contacts can be treated as nonmagnetic metals.

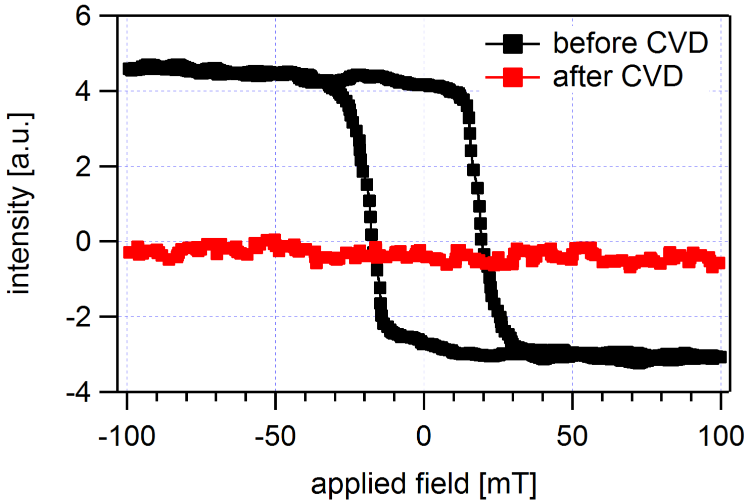

Figure 4.2: MOKE measurements on Re/Co (20/40 nm) contacts. After CVD process (red squares) the signal vanishes, indicating that the surface is no longer ferromagnetic.

4.1.2 Electronic Sample Characterization

As a first rough characterization of the electronic sample behavior, the conductance at 0 V dc bias with a small ac excitation of 10 µV was measured for a large gate voltage range. Figure 4.3 shows the measured conductance in the gate voltage range between -5 and +10 V. It features Coulomb peaks throughout the whole gate voltage range with a bandgap between 0 V and 1.1 V. The overall conductance of this sample is very low ($\sim 10^{-2}$ e^2/h) with a peak value of $\sim 8 \cdot 10^{-2}$ e^2/h on the hole side. To get higher conductances a higher gate voltage range was chosen to perform more precise measurements.

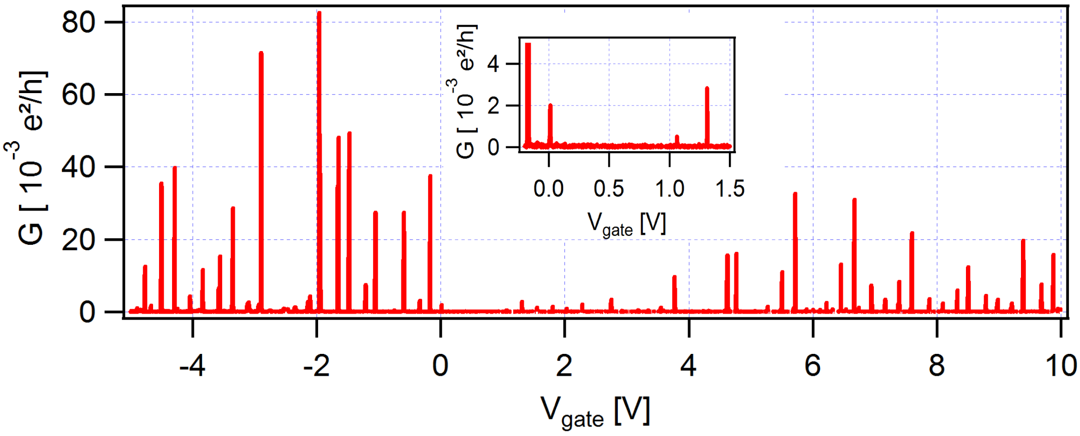

Figure 4.3: Differential conductance versus gate voltage: Coulomb peaks with low conductances visible. Inset shows a bandgap between 0 and 1.1 V.

A stability diagram with a bias voltage window from -20 to 20 mV was measured in the gate voltage range of 10.8 V to 12 V. Figure 4.4 shows the absolute value of current measured in this range. The Coulomb diamonds seem regularly spaced, which suggests that there is only a single carbon nanotube connecting the source and drain electrode, since more single tubes or a bundle of tubes would lead to additional overlapping Coulomb diamonds. Abstracting the slopes from the SET lines, highlighted by blue lines in Fig. 4.4, confirms the suspicion of a single CNT device. With help of the blue overlaying lines, one can see that every fourth Coulomb diamond is larger than the others. This indicates a four fold symmetry of the CNT and therefore one can assign the number of charge states per shell for each diamond, as described in Ch. 2.3.4. The slopes of the source and drain lines, acquired from different Coulomb diamonds, are presented in Tb. 4.1. With these one can calculate the gate conversion factor α_G for each diamond leading to an

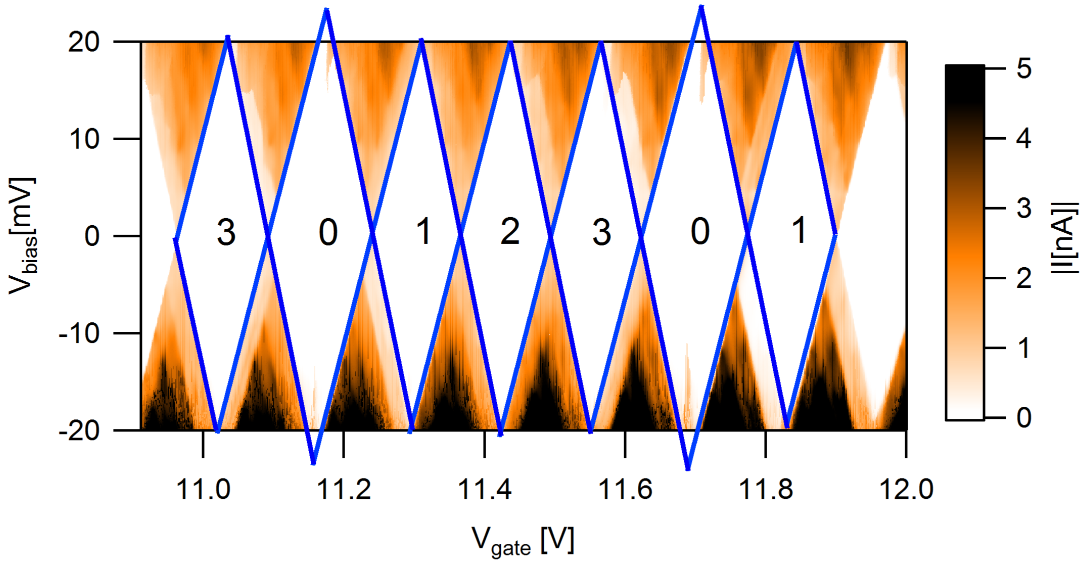

Figure 4.4: Absolute value of current versus gate and bias voltage: The regular Coulomb diamond pattern suggests the presence of a single CNT device. Slopes are highlighted by blue lines, forming the Coulomb diamonds. Every fourth diamond is larger indicating a four fold symmetry. This allows one to count the number of charges per shell, depicted with black numbers inside the diamonds.

average value for the gate conversion factor of

$$\bar{\alpha}_G = 0.158.$$

Charge state N	λ_d	λ_s	$\alpha_G = (\lvert\lambda_s\rvert + \lvert\lambda_d\rvert)^{-1}$
0	2.979	3.482	0.1548
1	2.931	3.33	0.1597
2	2.788	3.458	0.1601
3	2.798	3.408	0.1611
4 / 0	2.738	3.704	0.1552

Table 4.1: The slopes of the source and drain SET lines (λ_s and λ_d) for the different charge states are listed. With these slopes the gate conversion factor α_G can be calculated.

Extracting the width of each Coulomb diamond from Fig. 4.4 and multiplying it by the average gate conversion factor $\bar{\alpha}_G$, one gets the addition energy needed to further charge the quantum dot. The addition energy is plotted versus the charge number in Fig. 4.5. Here again the four fold symmetry is visible, since every fourth addition energy is higher than the others.

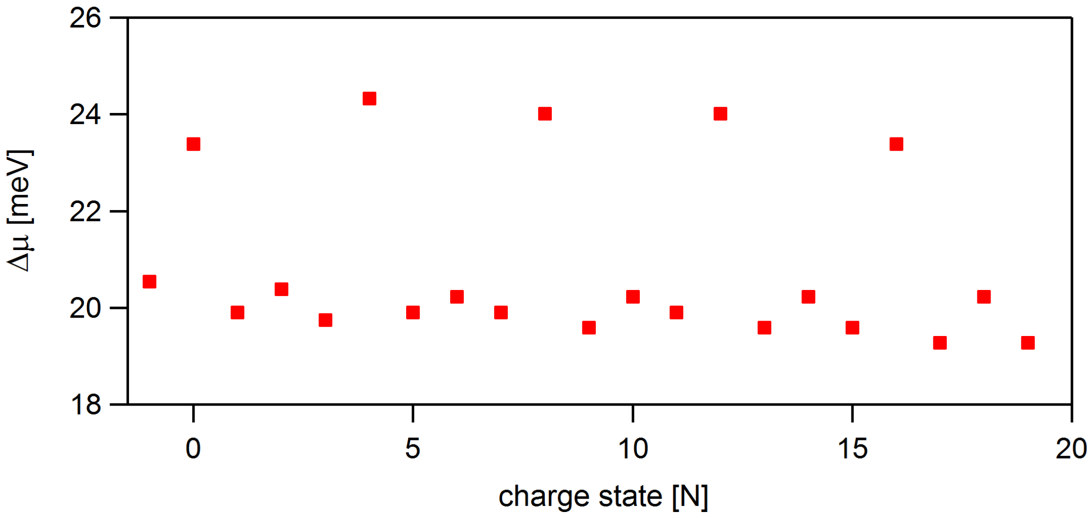

Figure 4.5: Addition energy $\Delta\mu$ versus charge states N: The addition energy is the distance between each crossing point of the Coulomb diamonds Δ_{Gate} multiplied with the average gate conversion factor $\bar{\alpha}_G$. Every fourth $\Delta\mu$ is increased, indicating a four fold symmetry.

The total capacitance of the CNT quantum dot is given by $C_\Sigma = C_{gate} + C_s + C_d = e^2/E_C$. Together with the slopes of the Coulomb diamonds $\lambda_s = \frac{C_\Sigma - C_s}{C_{gate}}$ and $\lambda_d = -\frac{C_s}{C_{gate}}$ one can calculate the values of the capacitances:

$$C_\Sigma = 7.69 \text{ aF}, \quad C_{gate} = 1.22 \text{ aF}, \quad C_s = 3.46 \text{ aF}, \quad C_d = 3.01 \text{ aF}.$$

Following the equations 2.32 one can extract important values of the CNT system, like the exchange coupling J, the band mismatch δ and the energy level separation $\Delta\epsilon$. These parameters are listed in Tb. 4.2, along with the average addition energies $\overline{\Delta\mu}_i$ for the different charge states. By measuring the bias voltage at which the line of the first excited state intersects the Coulomb diamond border (cf. Fig 4.6) one obtains an energy difference $\Delta E = 4.6 \pm 0.3$ meV. This value is similar to the previously extracted $\Delta\epsilon = 4.1 \pm 0.8$ meV, listed in Tb. 4.2. Therefore this excited state line is attributed to the shell spacing $\Delta\epsilon$. With this obtained $\Delta\epsilon$ one can estimate the length of the measured nanotube via

$$L = \frac{h v_F}{2\Delta\epsilon} \approx 379 \pm 27 \text{ nm}, \tag{4.1}$$

$\overline{\Delta\mu}_1$	19.7 ± 0.4 meV
$\overline{\Delta\mu}_2$	20.3 ± 0.2 meV
$\overline{\Delta\mu}_3$	19.8 ± 0.6 meV
$\overline{\Delta\mu}_4$	23.8 ± 0.4 meV
$\Delta\epsilon = \overline{\Delta\mu}_4 - \overline{\Delta\mu}_1$	4.1 ± 0.8 meV
$J = (\overline{\Delta\mu}_2 - \overline{\Delta\mu}_1)/2$	0.3 ± 0.3 meV
δ	0

Table 4.2: The average values for $\overline{\Delta\mu}_i$ with $i \in \{1,2,3,4\}$, extracted from the heights of the measured Coulomb diamonds, the calculated quantum energy level separation $\Delta\epsilon$, the exchange interaction J and the band splitting δ are listed.

where $v_F = 8.1 \cdot 10^5$ m/s is the Fermi velocity of electrons in carbon nanotubes. This result is in good agreement with the predicted length, since the distance between source and drain electrode is 350 nm.

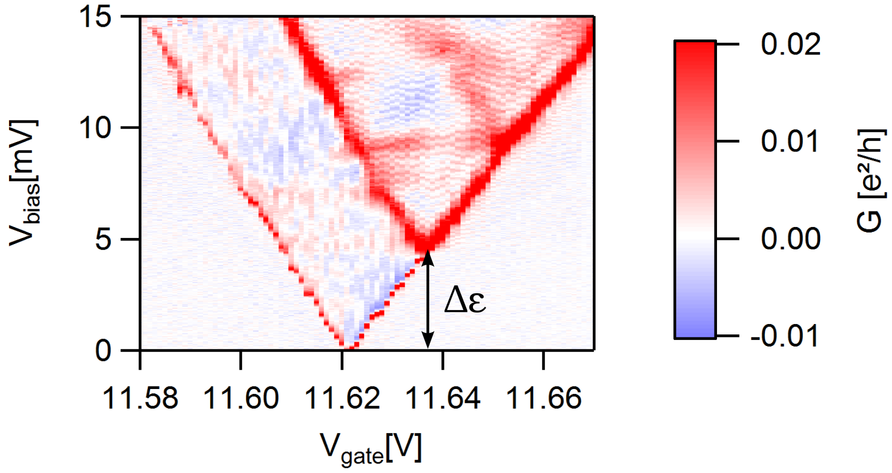

Figure 4.6: Differential conductance versus gate and bias voltage: a clear excitation line is visible in the stability diagram, which is assigned to the shell spacing $\Delta\epsilon$.

To get an estimate of the tunneling rates $\Gamma_{tot} = \frac{\Gamma_s \Gamma_d}{\Gamma_s + \Gamma_d}$ one has to investigate the current flowing through the quantum dot, since $I = e\Gamma$.

Figure 4.7 shows a line-cut through a Coulomb diamond at the $0 \rightarrow 1$ transition for $V_{bias} = 2$ mV. The bias voltage must be small, so no excited states contribute to the transport. Since the ground state (charge state 1) is four fold degenerate, the rate to tunnel into the dot is four times larger than the rate to tunnel out. Therefore the total tunneling rate becomes:

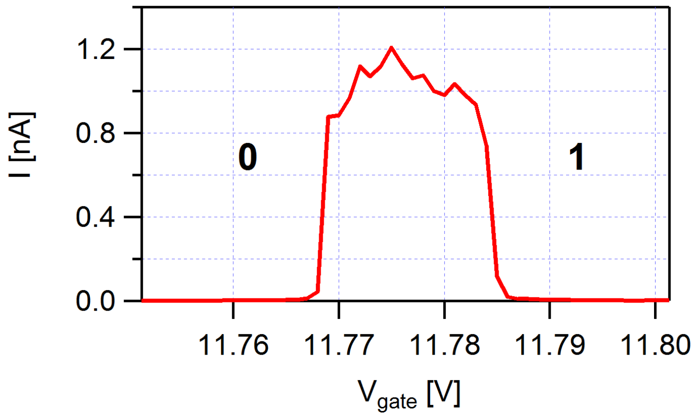

Figure 4.7: Current versus gate voltage: line-cut through Coulomb diamond of the 0 → 1 transition at 2 mV bias voltage.

$$\Gamma_{tot} = \frac{4\Gamma_s \Gamma_d}{4\Gamma_s + \Gamma_d} \xrightarrow{\Gamma_s = \Gamma_d = \Gamma} \frac{4}{5}\Gamma. \tag{4.2}$$

This alters the relation for the current to $I = \frac{4}{5}e\Gamma$. A current of about $I \approx 1.0$ nA, as in Fig. 4.7, leads to a coupling strength of $\hbar\Gamma \approx 5.1$ µeV.

4.2 Dark States

For gate voltages higher than 11.7 V, additional features appear in the stability diagram. Figure 4.8a shows the stability diagram for the next two shells. Some Coulomb diamonds seem to have missing resonant lines (red arrows in Fig. 4.8a) on one side and a negative differential conductance (blue arrows) on the opposing side of the Coulomb diamond. This happens at the 0 → 1 transitions for negative bias voltages and at the 3 → 4 transitions for positive bias voltages, which suggests a particle-hole symmetry of the underlying effect. This behavior is also clearly visible in Fig. 4.8b (indicated by black arrows), where the current is plotted versus the gate voltage at $V_{bias} = \pm 3.045$ mV. For positive bias, the fourth and the eighth transition shows no sudden jump, but an exponential-like increase of the current. For the negative bias value, the first and the fifth transition show this characteristic shape. However the 1 → 2 and 2 → 3 transitions are not affected, since they show the expected step-like behavior of the current for both signs of the bias voltage, as presented in Fig. 2.7c.

A possible explanation for these features in transport measurements is the current suppression by the formation of *dark states*, as described in Ch. 2.4.3.

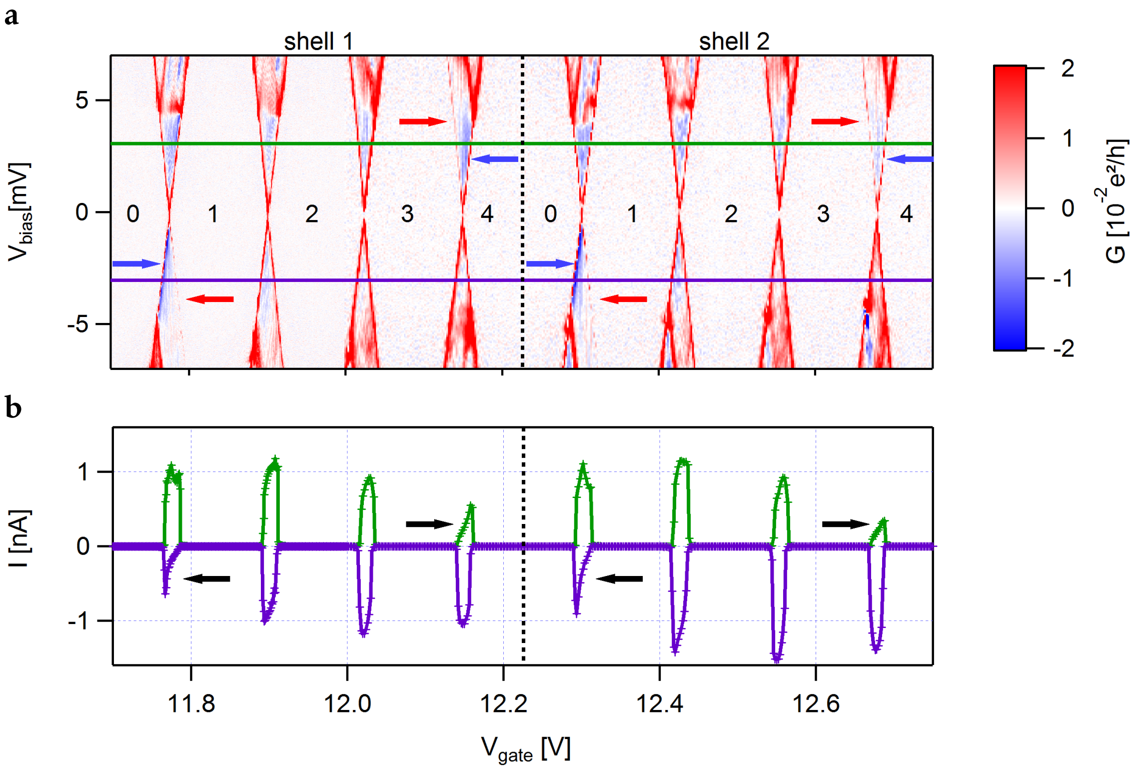

Figure 4.8: **a** Differential conductance versus bias and gate voltage: Stability diagram for two shells in the gate range between 11.7 and 12.75 V. Faint resonant lines (red arrows) and negative differential conductance (blue arrows) are observed. The green and purple lines show the line cut positions of Fig. 4.8b. **b** Current versus gate voltage: line cuts at $V_{bias} = \pm 3.045$ mV. Black arrows indicate regions of current suppression.

A dark state is a result of electron interference due to a coherent superposition of the two degenerate angular momentum states $L_z = \pm l$. Although the dark state can be entered by an electron, tunneling out is forbidden by the condition $\langle L_z = 0|d_{\alpha\sigma}|\mathrm{DS}\rangle = 0$. Therefore the transport is blocked and no current is flowing through the quantum dot. However this is not sufficient to explain the measured features since a dark state would block the transport completely and the whole conducting region of the charge transition should vanish. A lamb shift [129,130], which is a term in Eq. 2.64 originating from the interaction with the leads, causes a precession between the dark and the coupled state (cf. Eq. 2.63). Therefore an electron in the dark state is allowed to precess into the coupled state and from there it will eventually tunnel out to the lead (cf. Fig. 2.14). As a consequence this precession partially destroys the interference effect allowing current to flow through the dot. The precession frequencies $\omega_{L/R}$ are strongly gate and bias voltage dependent, which leads to the smooth negative differential conduc-

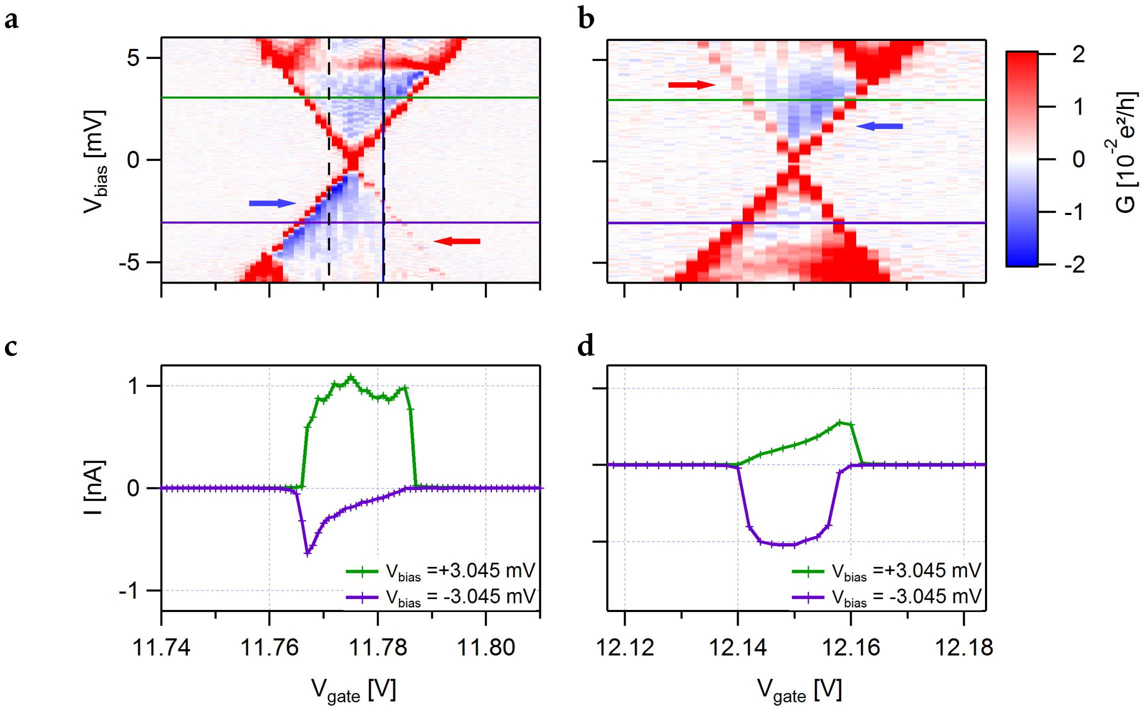

Figure 4.9: Detail view of Fig. 4.8a for **a** 0 → 1 and **b** 3 → 4 transition. The stability diagrams show faint resonance lines and areas with negative differential conductance. Green and purple lines indicate the positions for the current versus gate voltage plots shown in **c** and **d**. Exponential decrease of the current visible, due to gate voltage dependency of the precession frequencies $\omega_{L/R}$. The dashed lines in panel **a** mark the positions of the line cuts presented in Fig. 4.10.

tance, marked with blue arrows in Fig. 4.9a and b. For instance at the 0 → 1 transition, ω gets smaller with increasing gate voltage. This reduces the escape rate for the electron to leave the dark state and therefore the current is more strongly suppressed at higher V_{gate} (cf. red arrows in Fig. 4.9a and b). This results in an exponential decrease of the current as a function of the gate voltage, as shown in Fig. 4.9c. For the 3 → 4 transition, presented in Fig. 4.9d, the effect of the dark state is visible for positive bias voltages and the escape rate increases with increasing gate voltage due to the particle-hole symmetry. In Fig. 4.10 the current is plotted versus the bias voltage for $V_{gate} = V_{gate,0} \pm 5$ mV, where $V_{gate,0}$ is the gate voltage corresponding to the crossing point of the source and drain lines, as illustrated by the dashed lines in Fig. 4.9a. The graphs refer to the 0 → 1 transition for shell 1 and shell 2 respectively. On the left side of the transition, presented in Fig. 4.10a, the current shows an exponential-like decrease for negative bias voltages (blue arrow), while on the right side (Fig. 4.10b), the current is

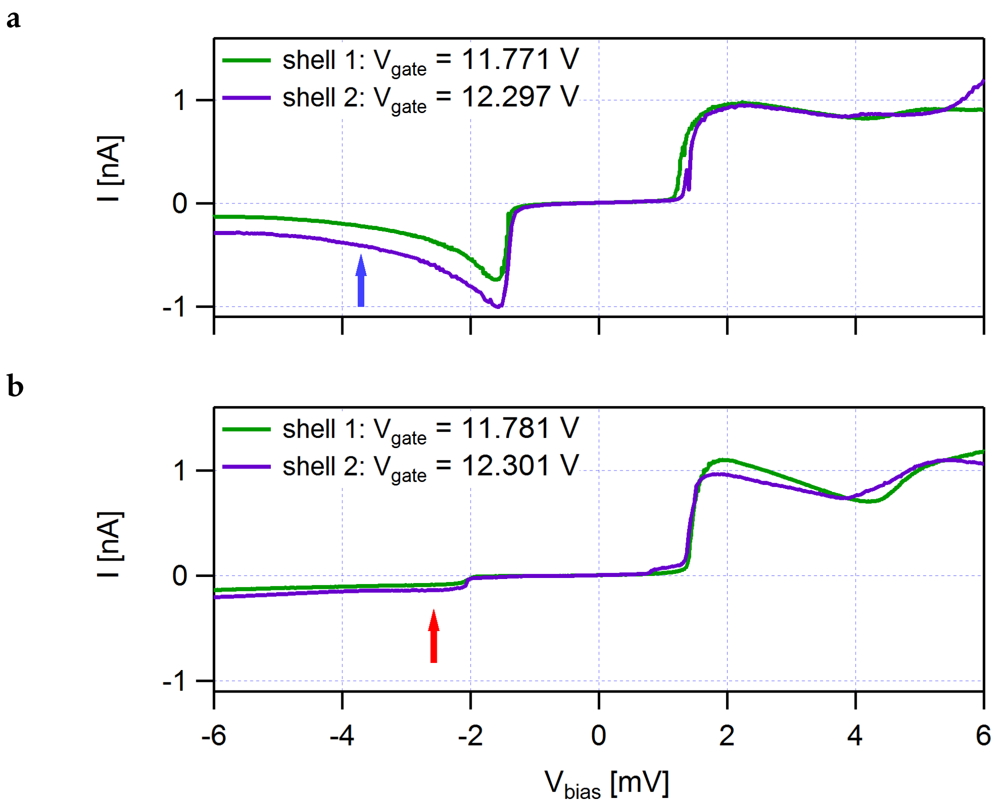

Figure 4.10: Current versus bias voltage: line cuts 5 mV **a** before and **b** after the crossing point of the source and drain lines of the 0 → 1 transition (indicated by the black dashed lines in Fig. 4.9a) of shell 1 (green) and shell 2 (purple). **a** At negative bias voltages a decrease in current, resulting in the negative differential conductance in Fig. 4.9a can be observed. **b** Current is strongly suppressed at negative bias voltages.

strongly suppressed (red arrow). For both sides of the transition the traditional step-like I-V characteristic is recovered at positive bias voltages. This implies that here the precession is strong and almost completely destroys the effect of the interference. This different behavior between positive and negative bias voltage is a result of a coupling asymmetry of the CNT with the contacts ($\Gamma_L > \Gamma_R$), since $\Gamma_{L/R}$ are prefactors of the precession frequencies $\omega_{L/R}$. Therefore the shape of the current profile, presented in Fig. 4.9c and d, changes with the bias direction.

4.3 Numerical Comparison

In order to proof the assumption that dark states in CNTs lead to these characteristic I-V features, the measured data has to be compared to the theoretical model by numerical calculations. These simulations were performed by Michael Niklas of the group of Prof. Dr. Milena Grifoni, by using the master equation approach for the stationary reduced density matrix, as described in 2.4.3:

$$0 = \mathcal{L}\rho^{\infty} = -\frac{i}{\hbar}[H_{CNT} + H_{LS}, \rho^{\infty}] + \mathcal{L}_{tun}\rho^{\infty} + \mathcal{L}_{rel}\rho^{\infty}. \tag{4.3}$$

In all calculations three shells of the carbon nanotube, one above and one below the reference shell, were considered and excited states with an energy difference larger than $1.5\epsilon_0$ were excluded.

In Fig. 4.11 a comparison between the experiment and the calculated current profile is presented. Figure 4.11a and c show the stability diagram of the $0 \rightarrow 1$ transition of shell 1. All the distinct features of dark states, formed in the CNT, are reproduced. The negative differential conductance at negative bias values on the left side of the transition (blue arrow in Fig. 4.11a), as well as the reduced conductance in the tunneling line of the source side (red arrow), are clearly visible. For positive bias values the conductance shows a typical behavior for a quantum dot, both in the experiment and in the calculation. Only the horizontal cotunneling line between the two excited states at $V_{bias} \approx 4.74$ mV, marked with a black arrow in Fig. 4.11a, is not present in the numerical stability diagram, since only sequential tunneling is considered in the simulation.

For the $3 \rightarrow 4$ transition, displayed in Fig. 4.11b and d, the features of the dark state appear at positive bias values due to particle-hole symmetry. Here the source line shows reduced conductance values (red arrow in Fig. 4.11b) while the right side features the negative differential conductance (blue arrow). At negative bias values the standard conductance behavior is recreated. The negative differential conductance at the excited state transition at negative bias voltages is the result of a broken particle-hole symmetry in the calculations.

The good agreement between experiment and calculation is also visible if one compares the resulting I - V curves. In Fig. 4.11e and f the current profile of the $0 \rightarrow 1$ and the $3 \rightarrow 4$ transition is displayed at $V_{bias} = \pm 3.045$ mV respectively. For positive bias voltages in the $0 \rightarrow 1$ transition, the calculated current values, depicted as red line, follows the ordinary step-like behavior of a transition where no dark state is present. On the other hand, the $3 \rightarrow 4$ transition shows no step in the current but a smooth exponential increase with increasing gate voltage, which is well reproduced by the simulation. At $V_{bias} = -3.045$ mV the current

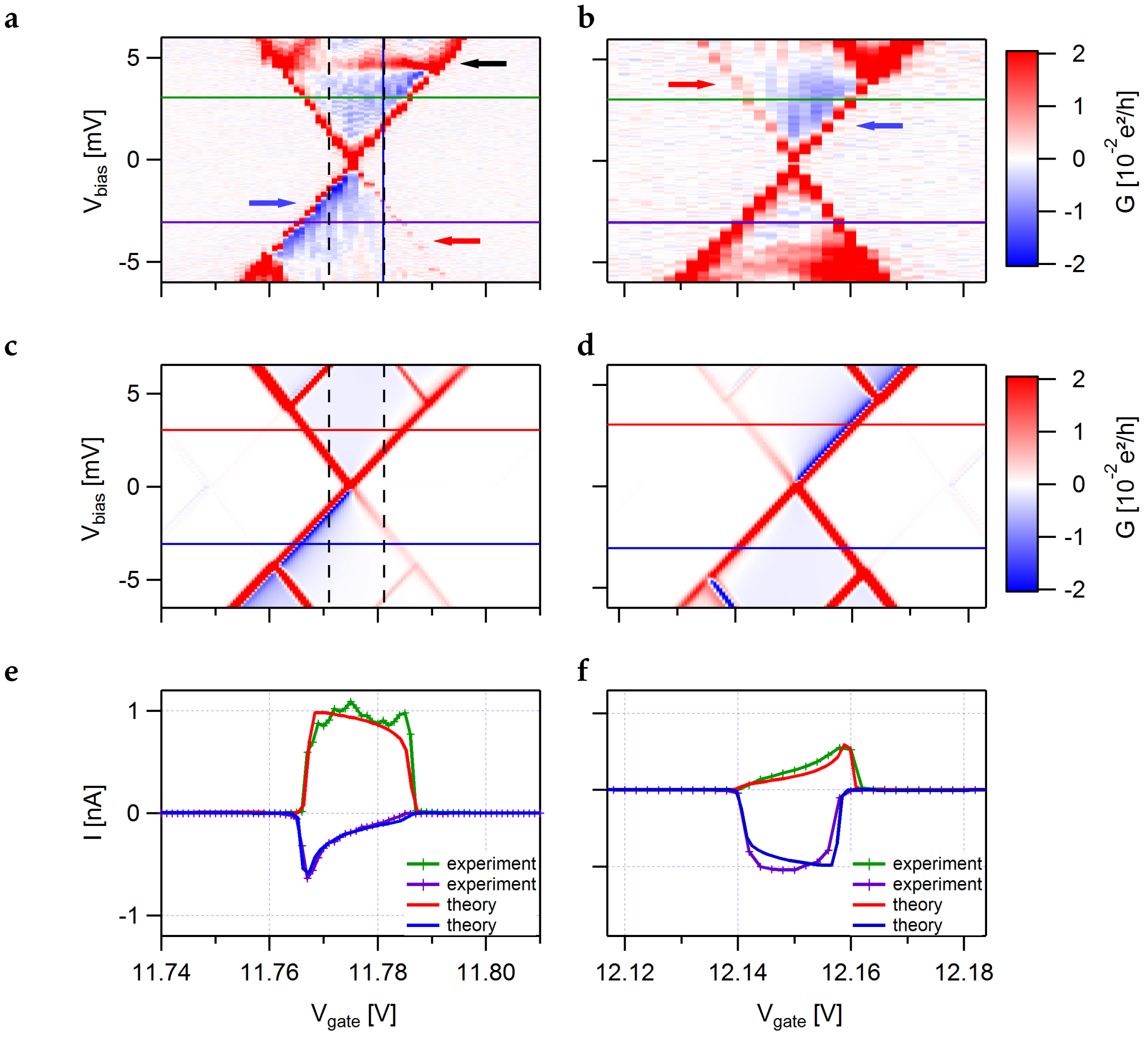

Figure 4.11: Comparison of 0 → 1 and 3 → 4 transition: **a**, **b** experimental stability diagram of shell 1. **c**, **d** corresponding numerical stability diagrams. **e**, **f** experimental and numerical current traces at $V_{bias} = \pm 3.045$ mV. The measured dark state features are well reproduced by the theoretical calculations.

suppression happens at the 0 → 1 transition while the other transitions show no blocking feature. There the precession frequency ω is so large, that the electron can escape the dark state fast enough to destroy the effect of the current blockade completely.
The effect of the precession frequencies on the current blockade can be shown

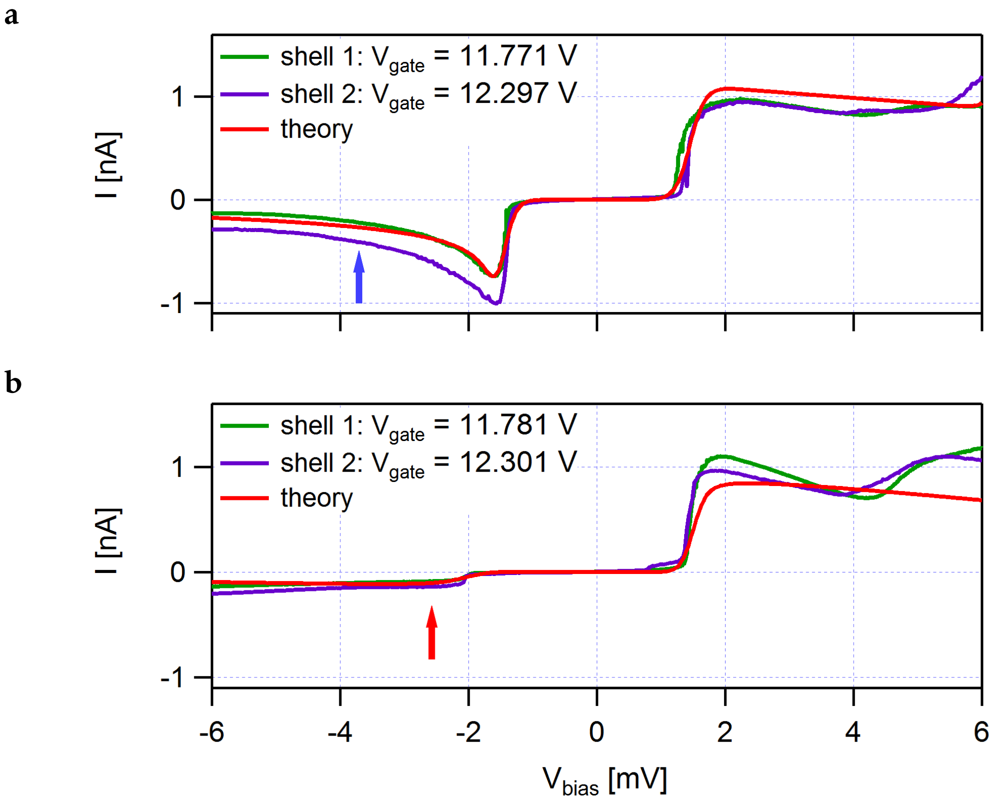

Figure 4.12: Current versus bias voltage: line cuts 5 mV **a** before and **b** after the crossing point of the source and drain lines of the 0 → 1 transition of shell 1 (green) and shell 2 (purple) in comparison with numerical calculations (red).

again by comparing current versus bias voltage plots at fixed gate voltages, as depicted in Fig. 4.12. The bias cuts are taken 5 mV before and after the crossing point of the tunneling lines of the 0 → 1 transition for shell 1 and shell 2, marked as black dashed lines in Fig. 4.11a and c. At positive bias values the current suppressing effect of the dark states is missing due to the high precession frequency, leading to the normal step-like form of the current. On the left side of the charge transition, the current decreases exponentially (cf. blue arrow in Fig. 4.12a) when going to more negative bias voltages. On the right side, depicted in Fig. 4.12b, the current is already nearly zero (red arrow), since the precession frequency is very low, which traps the electron in the dark state and blocks the transport. Again the theoretical model is in very good agreement with the measured data.

Although the effects of dark states are only observed at the one-electron ground states of the CNT, the formation of dark states is not limited to these states. The two-electron ground state can form dark states itself, with $\langle 1, E_{1_0}; \frac{1}{2}, \pm\frac{1}{2}, \pm l | d_{\alpha\sigma} | 2, DS \rangle = 0$ and $\langle 1, E_{1_0}; \frac{1}{2}, \pm\frac{1}{2}, \pm l | d_{\bar{\alpha}\sigma} | 2, DS \rangle \propto sin(l(\phi_R^n - \phi_L^n)) \neq 0$. However the interference at the $1 \rightarrow 2$ and $2 \rightarrow 3$ transition strongly depends on the exchange energy J. By using $J \approx \Gamma_\alpha$, the splitting of ground and excited state is large enough to partially destroy interference without observing additional excitation lines. Therefore the $1 \rightarrow 2$ and $2 \rightarrow 3$ transitions show no features of dark states in their transport behavior.

parameter	shell 0	shell 1	shell 2
ϵ_0		4.35 meV	
U		20 meV	
J		10 µeV	
$k_B T$		0.5 meV	
$\hbar\Gamma_L$	2 µeV	10 µeV	10 µeV
$\hbar\Gamma_R$		4 µeV	
$\hbar\Gamma_{rel}$		0.1 µeV	
$\Delta\phi$	0.01π	0.22π	0.13π
η		0.45	

Table 4.3: Numerical parameters used to fit all three shells of the experiment, with $\Delta\phi = \phi_R - \phi_L$.

In Tb. 4.3 the numerical parameters to fit all three shells of the experiment are listed. Here ϵ_0 corresponds to the shell spacing $\delta\epsilon$. The numerical value $\delta\epsilon = 4.35$ meV is in good agreement with the extracted value of $\delta\epsilon = 4.1 \pm 0.8$ meV, listed in Tb. 4.2. The charging energy $U = 20$ meV also fits the average values of $\overline{\Delta\mu_i}$ with $i \in \{1, 2, 3\}$, which were gathered from the heights of the Coulomb diamonds. Although the numerically calculated exchange energy $J = 10$ µeV is smaller than the experimentally extracted $J \approx 0.3 \pm 0.3$ meV, it is only used as a lower limit, big enough to destroy the interference effect at the two-electron transitions $1 \rightarrow 2$ and $2 \rightarrow 3$. Since it is not possible to determine the individual coupling strengths of the different leads, the total tunneling rate Γ_{tot}, defined in Eq. 4.2, must be used for comparison. The extracted coupling strength $\hbar\Gamma \approx 5.1$ µeV is in the same order as $\hbar\Gamma_L$ and $\hbar\Gamma_R$, used in the numerical calculations.

4.4 Chapter Summary

In this chapter a suspended carbon nanotube quantum dot was investigated. The tube was grown over two Re/Co contacts with a distance of 350 µm. Electronic characterization of the device revealed a clear four fold periodicity in the Coulomb diamond pattern. At gate voltages higher than $V_{gate} = 11.7$ V the $0 \rightarrow 1$ and $3 \rightarrow 4$ transitions showed distinct features in the transport behavior. A smooth negative differential conductance, leading to a exponential decrease in current, and suppressed tunneling lines on the other side of the transition were found at negative bias voltages for the $0 \rightarrow 1$ and at positive bias voltages for the $3 \rightarrow 4$ transition. These features disappeared at bias voltages large enough for the first excited state to enter. This transport behavior was assigned to the formation of dark states in the carbon nanotube quantum dot (see Ch. 2.4.3). This is possible when the orbital states are degenerate and the tunneling between the leads and the tube happens locally, allowing an angular momentum depended tunneling phase $l_z\phi_\alpha$ to be acquired. Therefore an antibonding linear combination can be found in which an electron can tunnel into, but is not allowed to tunnel out through the requirement $\langle L_z = 0|d_{\alpha\sigma}|\mathrm{DS}\rangle = 0$. Due to the interaction of the CNT system with the leads a Lamb shift introduces a precession between the coupled and the dark state. This allows electrons to escape the dark state and contribute to transport, partially lifting the current blocking. The rates at which electrons can escape the dark state are described by the precession frequencies $\omega_{L/R}$. The bias and gate voltage dependence of these precession frequencies leads to the observed features in the single-electron states. The exchange energy J destroys the interference effect, therefore the $1 \rightarrow 2$ and $2 \rightarrow 3$ transitions show the normal transport behavior. The experimental data was compared with numerical calculations which were able to reproduce all observed features. The fitting parameters used in the simulations are in good agreement with the ones extracted from the measurements, which leads to the conclusion that the observed transport features can indeed be attributed to dark states, formed in a carbon nanotube quantum dot.

5 Electromechanical Instabilities

In this chapter the nanoelectromechanical effects on the transport behavior in a carbon nanotube single quantum dot are presented.
At first the device is characterized, then occurring nanomechanical features in the stability diagram are presented. The magnetic field dependence of those features, as well as the noise behavior is shown and discussed.

5.1 Basic Device Characterization

The carbon nanotube quantum dot fabrication followed the same design as shown in Fig. 4.1, merely the contact material was altered. For this device the contacts consist of an alloy of $Re_{80}Mo_{20}$ with a thickness of 100 nm. The distance between the two contacts was left unchanged at 350 nm.

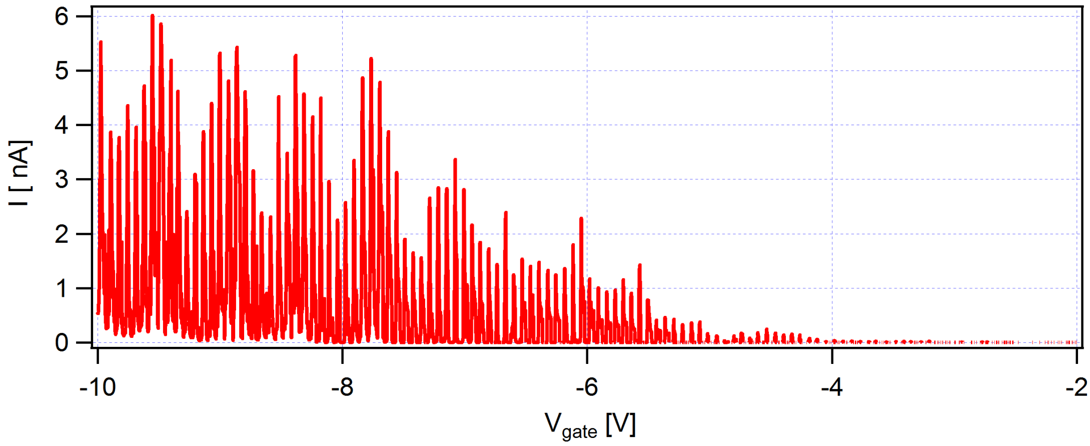

Figure 5.1: Current versus gate voltage at $V_{bias} = 1$ mV: Coulomb peaks are gradually appearing on the hole-side for negative gate voltages around $V_{gate} \approx -2.5$ V.

To get a first overview of the sample, the current was measured in dependence of the backgate voltage at a fixed bias voltage $V_{bias} = 1$ mV, as shown in Fig. 5.1.

The device shows only conductance on the hole-side of the CNT. The current increases with higher negative gate voltages and reaches values of $I_{max} \approx 6$ nA. The device shows clear and regular Coulomb peaks, which appear gradually for $V_{gate} \approx -2.5$ V. This makes it impossible to identify the first hole of the nanotube.

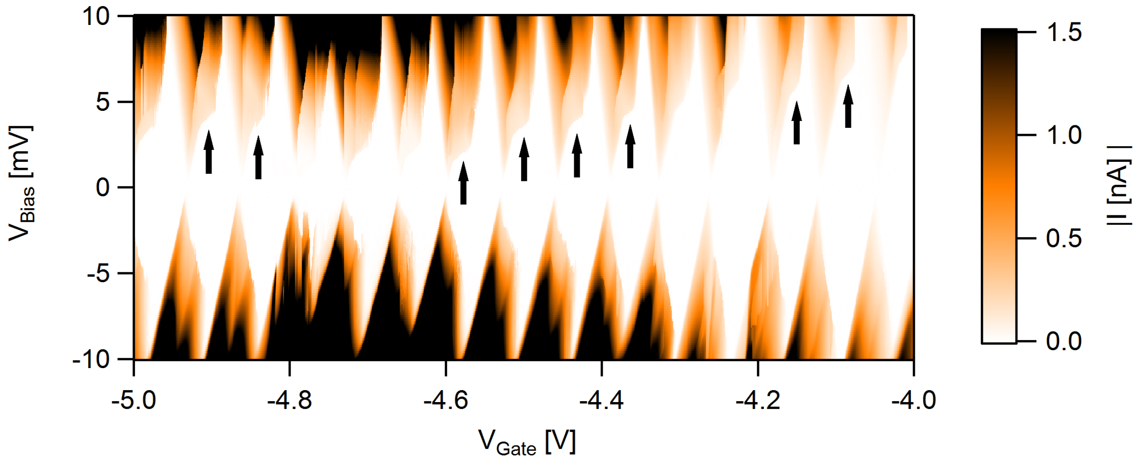

Figure 5.2: Absolute value of current versus bias and gate voltage: The Coulomb diamonds do not overlap, suggesting a single CNT device. Arrows indicate regions where the source and drain lines are bent and the conducting region is extended. Sudden current changes inside the charge transitions are visible. For small bias voltages a gap in transport is observed.

A stability diagram with a bias voltage window from -10 to 10 mV was measured in the gate voltage range of -5 to -4 V. Figure 5.2 shows the absolute value of current measured in this range. The stability diagram does not show overlapping Coulomb diamonds, which suggests that this device consists of a single carbon nanotube connecting the source and drain electrodes. In order to obtain the gate conversion factor $\bar{\alpha}_G$ the slopes of the Coulomb diamonds have to be extracted. However most of the Coulomb diamonds have no straight source or drain lines, but the charge transitions reach into regions where the current is usually blocked. This is eminently visible on the right side of the charge transitions for positive bias values, marked by black arrows Fig. 5.2. This circumstance makes it difficult to extract the slopes. The extraction was limited to Coulomb diamonds with mainly straight SET lines.

Table 5.1 presents the obtained values for the slopes of the source and drain lines λ_s and λ_d.

N	λ_d	λ_s	$\alpha_G = (\lvert\lambda_s\rvert + \lvert\lambda_d\rvert)^{-1}$
1	2.057	4.235	0.159
2	1.677	4.625	0.159
3	1.550	4.625	0.162
4	1.793	4.828	0.151
5	2.182	4.258	0.155
mean	1.852	4.514	0.157

Table 5.1: This table shows the slopes of the source- and drain SET lines (λ_s and λ_d) for different Coulomb diamonds. With these slopes the gate conversion factor α_G can be calculated.

A mean value for the gate conversion factor of

$$\bar{\alpha}_G = 0.157$$

was gathered, which is almost identical to the gate conversion factor extracted for the device investigated in Ch. 4. Since the sample design is almost unchanged, this value is in good agreement.

In Fig. 5.3 the charging energies, which are obtained by multiplying the distance between two Coulomb oscillations with the average gate conversion factor $\bar{\alpha}_G$, are compared. There is a two fold pattern visible concerning the number of charges. Only charge states 6 and 10 do not follow the even-odd pattern. The CNT shows no four fold symmetry and therefore no complete analysis about the charge state or the addition energy can be made. The absence of this four fold symmetry is not surprising since the K and K' are likely to be mixed by defects or at the contacts. This causes a lift of their degeneracy [50]. Following Eq. 2.28 and 2.29, the capacitances of the system can be calculated:

$$C_\Sigma = 15.1 \text{ aF}, \quad C_{gate} = 2.37 \text{ aF}, \quad C_s = 10.71 \text{ aF}, \quad C_d = 2.02 \text{ aF}.$$

Another feature visible in Fig. 5.2 is the current suppression for small bias voltages. A zoom into this region is presented in Fig. 5.4a. Here one transition in a bias region of $V_{bias} = \pm 2.5$ mV is shown. The edges of the Coulomb diamonds are highlighted by blue lines. One can see that in addition to a gap between the transition for positive and negative bias values, the transitions seem to be shifted in gate voltage. By comparing the difference in bias voltage between the two tips a gap energy of $E_{gap} \approx 250$ µeV can be extracted. There are different possibilities why this gap in the stability diagram may occur. Nanomechanical current

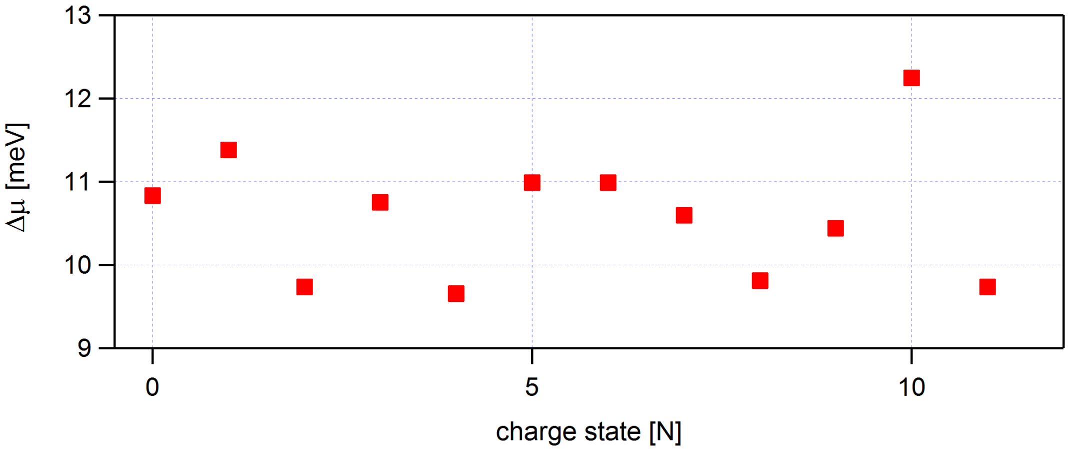

Figure 5.3: Addition energy E_C versus charge state N: charge states 6 and 10 do not follow the otherwise visible two fold periodicity.

blockade, as described in Ch. 2.6.2, could be one reason. Here the bending of the tube changes the distance between the quantum dot and the backgate, which leads to a change in the gate capacitance. Therefore the gate voltage value, at which the Coulomb oscillation takes place, changes with the distance of the oscillating tube to the backgate, resulting in a region where the current is always blocked (cf. Fig. 2.21). One indication of this effect is the continuous increase of the current at the boundary of the conducting region [117] as opposed to the expected step-like current behavior. Figure 5.4b shows a line cut through the conducting region at a bias voltage of $V_{bias} = -1.5$ mV. Here the deviation from a step-like current profile can be observed. The effect that the conducting regions for positive and negative bias values are shifted with respect to each other is not predicted by this model, but was observed experimentally [118]. The gap energy is given by $E_{gap} = \lambda^2 hf$ [96], where λ is the electron-vibron coupling and f the frequency of the oscillator. Here the bending mode of the CNT is the responsible oscillation, because it changes the position of the quantum dot with respect to the backgate. For a carbon nanotube with a length of $L = 350$ nm, a Youngs modulus of $Y = 1$ TPa, a mass density of $\rho = 1.3$ g/cm^3 and a radius of $R = 1$ nm, the frequency of the bending mode, given by Eq. 2.85, results in $f_{bend} \approx 0.4$ GHz. Therefore a coupling constant of $\lambda \approx 12.3$ would be needed for a gap of 250 μeV to occur. Since the maximum coupling constant for the bending mode (given by Eq. 2.86) is predicted to be $\lambda = 1.75$, it is unlikely that this form of current blockade is responsible for the gap. Other nanomechanical modes which might block the current for small bias voltage values are described

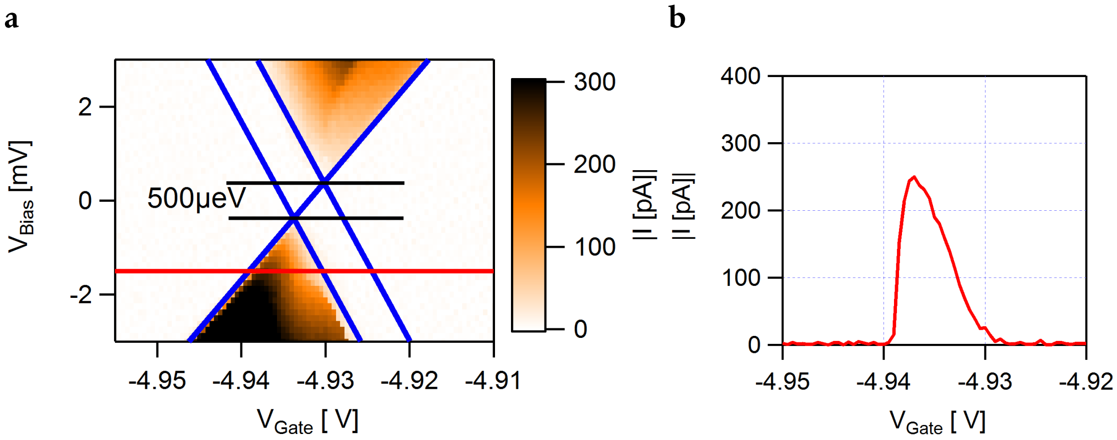

Figure 5.4: **a** Zoom into a region of small bias voltage. Positive and negative bias voltage regions of the charge transitions are shifted in gate voltage with respect to another. A gap with an extracted gap energy of $E_{gap} \approx 250$ µeV is visible between positive and negative bias voltage. **b** Gate voltage cut at $V_{bias} = -1.5$ mV, indicated by the red line in **a**.

by the Frank-Condon blockade (cf. Ch. 2.6.2). Here the probability for a transition between two electronic levels strongly decreases for low vibrational modes and a high enough coupling constant. From Fig. 2.18 one can extract that the energy of the stretching mode lies between $0.1 \leq E_{stretch} \leq 1$ meV. Therefore the coupling constant $\lambda^2 = E_{gap}/E_{stretch}$ is in the range of $0.5 \leq \lambda \leq 1.6$. The maximum coupling constant can be approximated by Eq. 2.84 and is $\lambda \approx 2.12$ for a nanotube with a radius of 1 nm. This coupling constant would be large enough for a gap with $E_{gap} = 250$ µeV to occur. However one would expect the appearance of vibrational sidebands in the stability diagram, which is not the case in our measurement.

The gap in the transport measurements could also be caused by the contact material. The $Re_{80}Mo_{20}$ alloy is supposed to be superconducting even after the CVD process, needed for the CNT growth [131]. Since the excitation spectrum of a superconductor is gapped by 2Δ, where Δ is the superconducting gap, the stability diagram of a quantum dot connected by superconducting leads also shows a gap. If the chemical potential of the dot lies in between the superconducting gap, the electron occupying the dot cannot tunnel out and no current is flowing. The gap size can be estimated by the critical temperature T_C of the superconductor [132]

$$\Delta(T = 0) \approx 1.764 k_B T_C. \tag{5.1}$$

The measured gap of $E_{gap} = 250$ µeV would correspond to a critical temperature of the superconducting leads of $T_C \approx 1.64$ K. Before CVD the $Re_{80}Mo_{20}$ alloy has a critical temperature of approximately $T_C \approx 8$ K [131]. The effect of the CVD nanotube growth process on the superconducting properties of the contact material can strongly vary. It can alter the critical temperature of the alloy and even destroy its superconducting behaviour [133]. Therefore a value of $T_C \approx 1.64$ is consistent. In order to explain the shift of the conducting regions in gate voltage, one of the two contacts must act as a non-superconducting metal. In Fig. 5.5a a diagram of a quantum dot connected to one superconducting and one metallic lead is shown. If the chemical potential of the dot lies inside the gap of the superconductor, no current is flowing. Figure 5.5b shows the calculated stability diagram of such a N-QD-S device. Since one of the two contacts does not have a superconducting gap anymore, the SET line for the normal metal stays unchanged. This results in a shift of the two conducting regions by $e\Delta V_{gate} = 2\Delta/\beta_-$, where $\beta_- = C_{gate}/C_d$ is the slope of the line where the chemical potentials of the dot and the normal metal are aligned $\mu_{NM} = \mu_{dot}$. Calculating the superconducting gap $\Delta = e\Delta V_{gate} * \beta_-/2$ from the shift in gate voltage $e\Delta V_{gate} = 472 \pm 79$ µeV, one obtains $\Delta = 276 \pm 46$ µeV, which is in good agreement with the measured gap

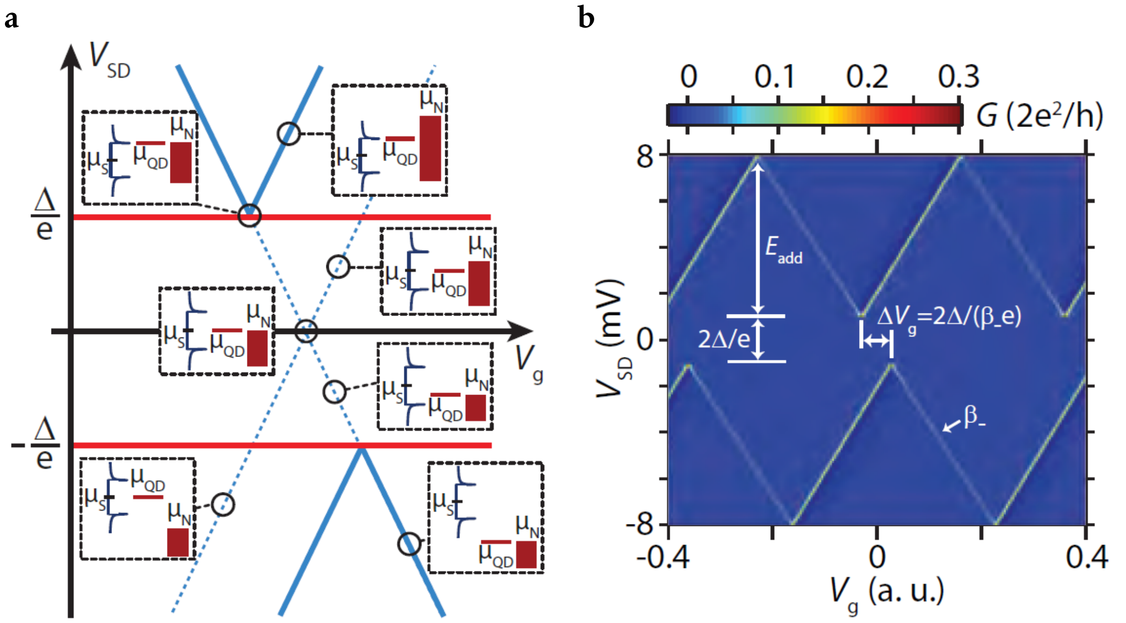

Figure 5.5: **a** Scheme of a stability diagram for a N-QD-S device. If the chemical potential of the dot μ_{QD} lies in the gap, no current can flow (dashed lines). A gap of 2Δ is visible in the transport and the conducting regions, restricted to the blue solid lines, are shifted. **b** Conductance versus gate and bias voltage: calculated for one superconducting lead with $\Delta = 1$ meV. Taken from [132]

of $E_{gap} = 250\ \mu\text{eV}$.
Superconducting leads, affected by the CVD process to form a N-QD-S device seem to be the most reasonable explanation for the observed gap in the transport data.

5.2 Instabilities

By further investigating the stability diagram, shown in Fig. 5.2, one notices that for positive bias voltages the conducting regions form "shoulders" which extend in the normally current-blocked regions of the Coulomb diamonds. These are emphasized by black arrows in Fig. 5.6. The blue lines indicate the shape of the Coulomb diamonds, if the SET lines where straight and no current would flow inside the usually blocked region. The bias voltage at which the current of the charge transitions reaches into the Coulomb diamond is marked as V_{onset}, as depicted in Fig. 5.7a. In Fig. 5.7b bias traces are depicted for four transitions at the gate position where the shape of the conducting region starts to reach in the Coulomb diamond. The height of the sudden current increase is referred to as I_{step}. The current jumps from 0 in the Coulomb diamond to values between $30\ \text{pA} \leq I_{step} \leq 152\ \text{pA}$. The step height of the current increases with more negative gate voltages and therefore with higher charge numbers, as shown in Fig. 5.7b. The values of the bias voltage at which the conducting region starts

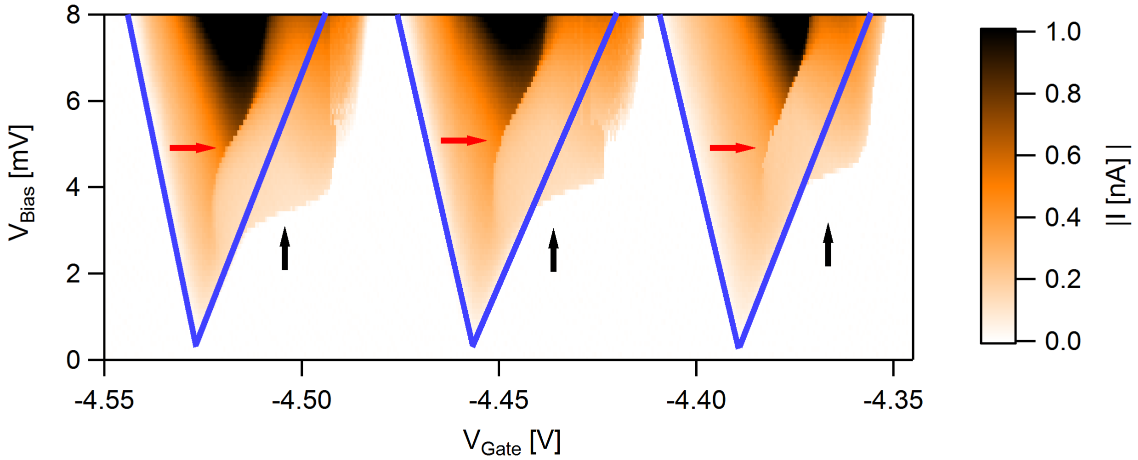

Figure 5.6: Detail view of Fig. 5.2. Blue lines highlight the source and drain lines of usual Coulomb diamonds. Right side of charge transition reaches into Coulomb diamonds (marked with black arrows). Red arrows indicate current jumps inside the conducting regions.

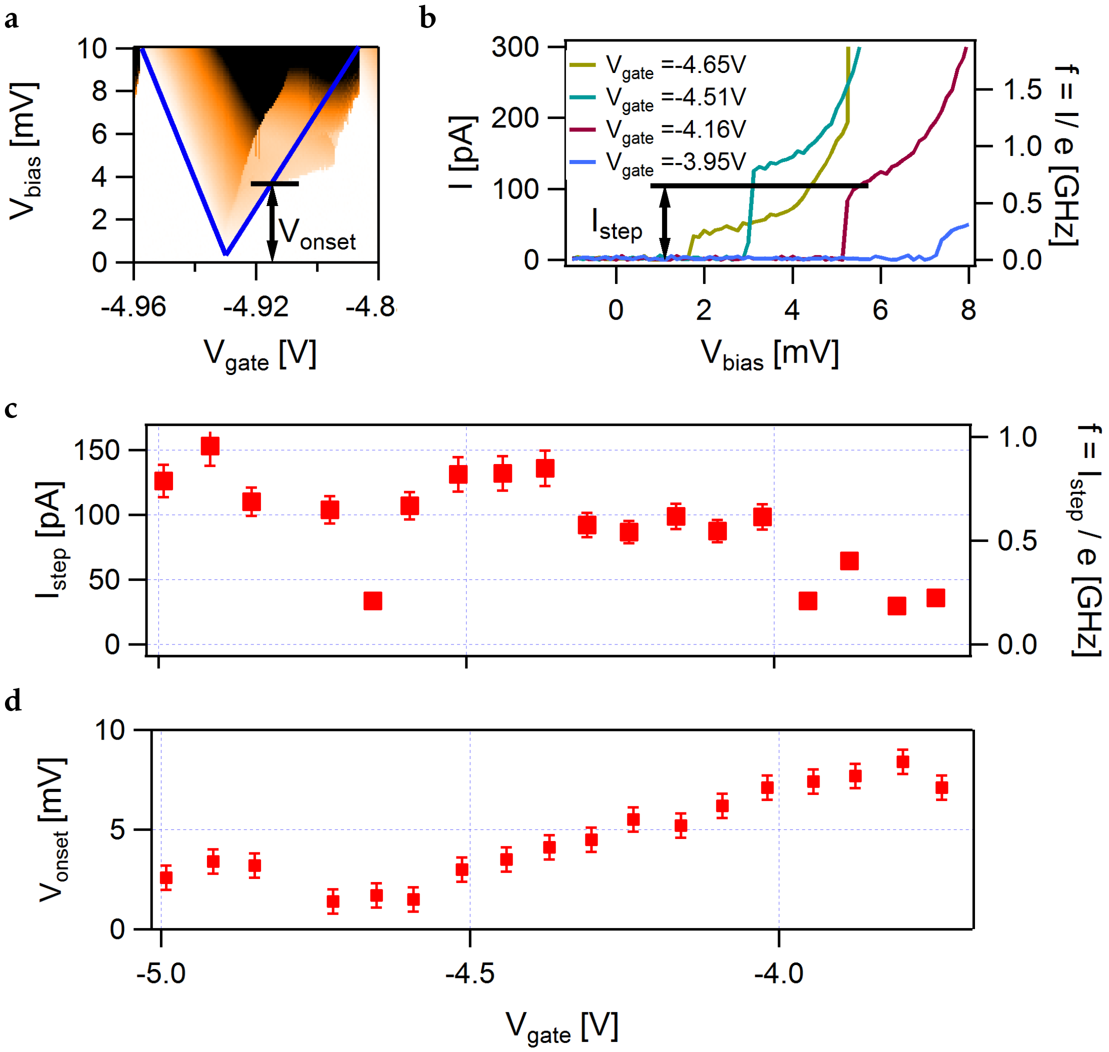

Figure 5.7: **a** Absolute value of current versus bias and gate voltage: Bias voltage at which the current reaches inside the Coulomb diamond is labeled as V_{onset}. **b** Current versus bias voltage: Line traces at gate voltage positions where current starts to reach into Coulomb diamonds for some charge transitions. Step-like increase of current with step heights between 30 and 152 pA. **c** I_{step} and $f = I_{step}/e$ versus gate voltage: Current step height increases with the number of holes occupying the dot. **d** V_{onset} versus gate voltage: Bias voltage at which the conducting region reaches into Coulomb diamonds V_{onset} decreases with more negative gate voltage.

to reach into the Coulomb diamonds is referred to as V_{onset}. Figure 5.7c shows the gate voltage dependence of V_{onset}. The bias voltage needed for the current to break into the otherwise blocked region decreases with increasing charge number. Comparing V_{onset} with the maximum current of the Coulomb oscillations (cf. Fig. 5.8) one notices that V_{onset} scales inversely with the tunneling rate Γ of the system.

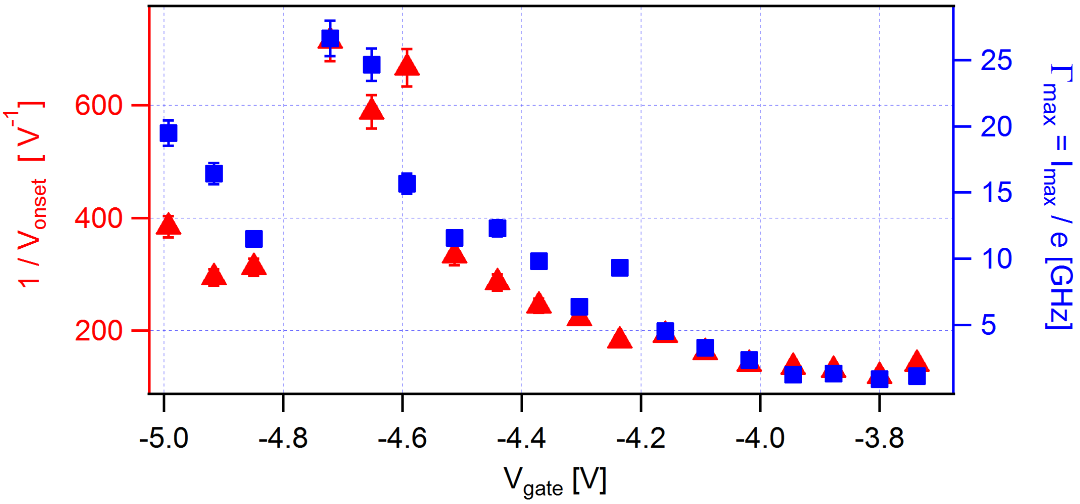

Figure 5.8: Comparison of V_{onset} with Γ: The inverse of the onset voltage $1/V_{onset}$ (red triangles) and the maximum current I_{max} divided by the elementary charge e (blue squares) are plotted for each charge transition. The curves follow the same gate voltage dependence, concluding $V_{onset} \propto 1/\Gamma$.

Additionally to the borders of the conducting regions, the shape inside is altered as well. Almost all charge transitions in Fig. 5.2 show a sudden jump of the current for positive bias voltages. The abrupt change in current is marked by red arrows in Fig. 5.6. Figure 5.9 gives a comparison between a weakly affected charge transition (cf. panel a) and one which is strongly altered (cf. panel c). For both transitions line cuts at different bias voltages are presented in Fig. 5.9b and d respectively. As described in Ch. 2.3.3 a rectangular current shape is expected for systems with low Γ and only one level contributing to the charge transport. However the current smoothly increases with increasing gate voltage, leading to round current profiles for all bias voltages, as depicted in Fig. 5.9b. Also the current is not constant in V_{bias} but increases continuously with increasing bias voltage. At a bias voltage of $V_{bias} = 9$ mV the current trace (orange line) runs through the region where current is flowing in the otherwise blocked region, leading to an increase of the transition width. For the second charge transition, the current

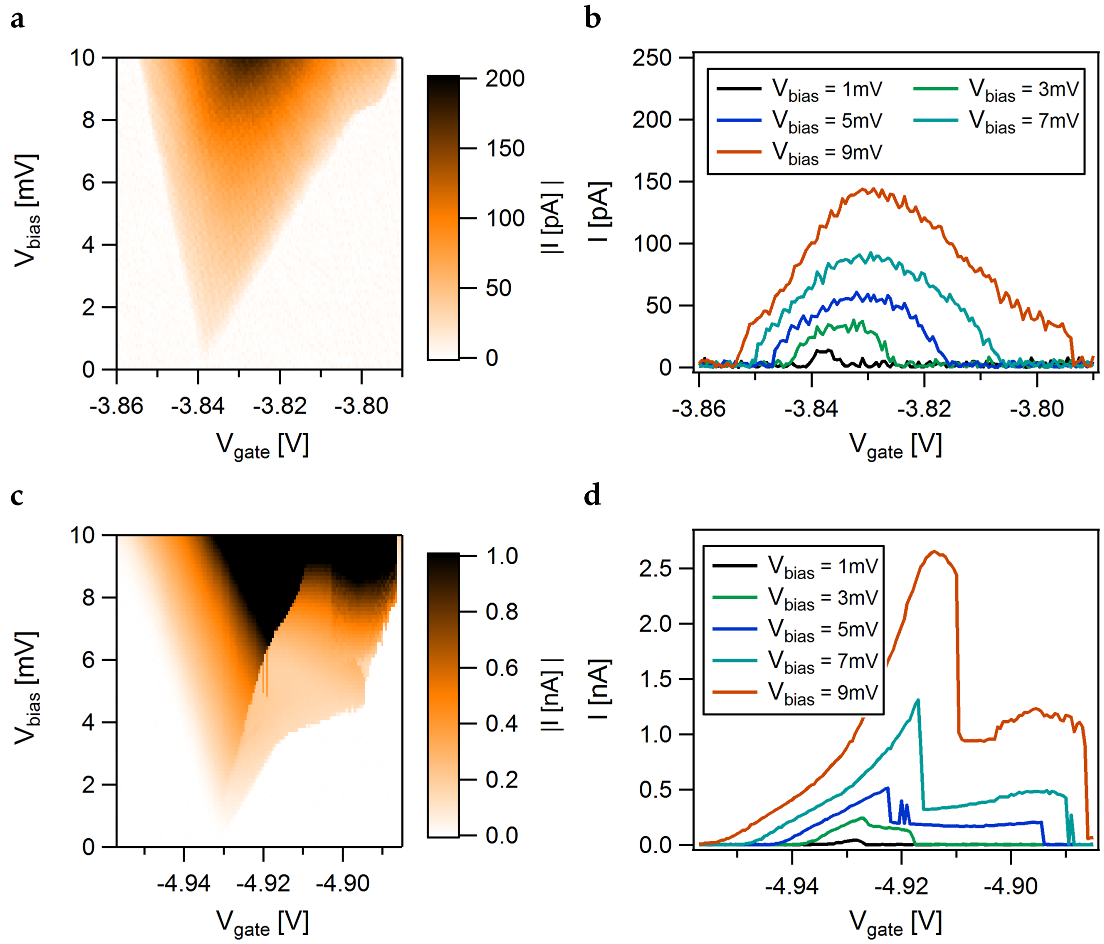

Figure 5.9: **a** Stability diagram of quasi unaffected charge transition. **b** Current versus gate voltage for different bias voltage values for the unaffected charge transition. **c** Stability diagram of a strongly modified charge transition. **d** Current versus gate voltage for different bias voltage values for the modified charge transition.

profiles differ more dramatically from the expected rectangular shape (cf. panel d). For small bias values (blue and green lines in Fig. 5.9d) the current increases almost linearly. At $V_{bias} = 3$ mV (green line) a small dent in the current profile is visible at $V_{gate} = -4.927$ V. With increasing bias voltage, this dent evolves into a drop of current. The position at which this current drop appears shifts to smaller gate voltages for increasing bias values. For $V_{bias} \geq 3.75$ mV (blue, green and orange lines) the line traces cut the region where the current extends into the Coulomb diamond, leading to prolonged plateaus in the current profiles.

A possible explanation for these distinct features in the transport measurements is current modifications due to strong feedback in nanoelectromechanical devices. As described in Ch. 2.6.2 the tunneling of electrons can act as a driving force for mechanical oscillations (e.g. the bending of the CNT). If these oscillations are underdamped, the amplitudes can become large enough to affect the current through the system [119–121]. Figure 5.10 shows a theoretical prediction from Ref. [120] for the current through a quantum dot device, modified (dashed lines) and unmodified (solid lines) by mechanical motion, in dependence of the gate voltage at different bias voltages. For small bias voltages (cf. panel a and b) the vibration only leads to a small dent in the current profile, which was also observed in Fig. 5.9d. Panel c and d of Fig. 5.10 show that for higher bias voltages the small dent becomes a jump in the current profile. In these regions the model predicts that the system is bistable, which means it can switch between oscillating with a finite amplitude and no oscillation, or it can oscillate with two different

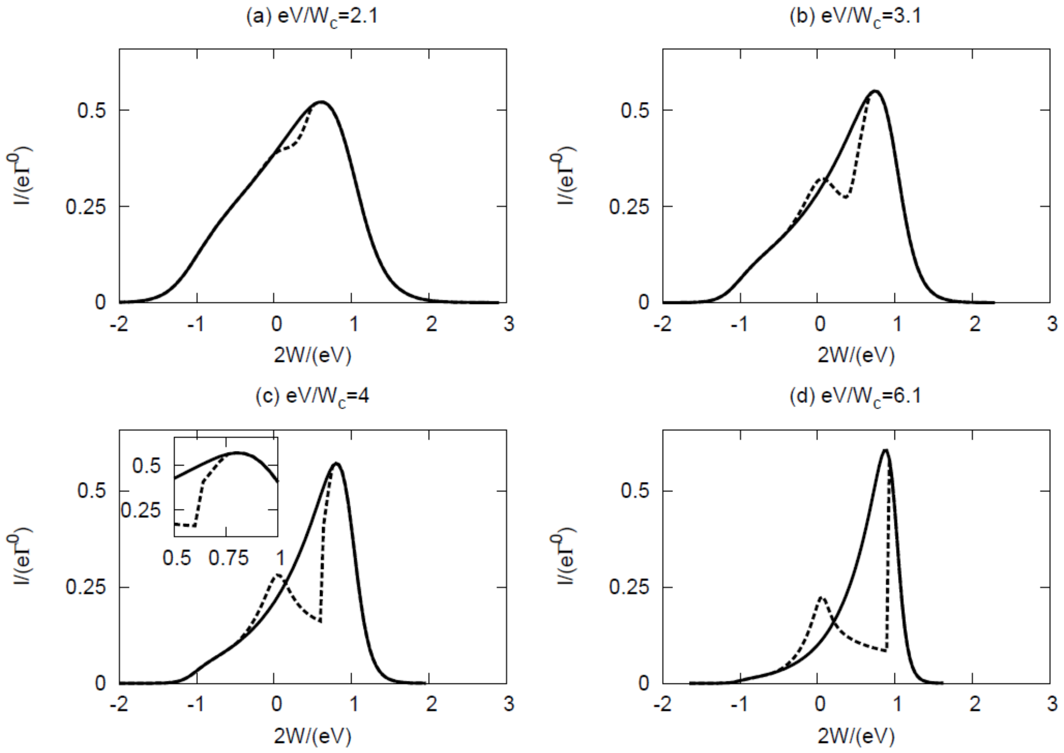

Figure 5.10: Model calculation by Usmani et. al: The dashed (solid) lines show the current modified (unmodified) by mechanical motion in dependence of the gate voltage for different bias voltages. In **a** and **b** generation of oscillation takes place. In **c** and **d** the system is bistable. Current jumps occur where the probabilities of two stable amplitudes are equal. Taken from [121].

amplitudes. The current jumps occur at positions where the probabilities of two stable amplitudes are the same. Also these features are well reproduced in the transport measurements. The current, modified by the generation of mechanical motion can extend in the normally blocked region [121], as shown in Fig. 2.22. Since the current flows only due to the oscillation, the assumption can be made that the current is limited by the frequency $I = e \cdot f_{bend}$ [102]. The current values 30 pA $\leq I_{step} \leq$ 152 pA are extracted from Fig. 5.7a. This leads to a bending frequency of $f_{bend} = 0.56 \pm 0.37$ GHz, which is in the same order as the previously calculated frequency $f_{bend} \approx 0.4$ GHz (cf. Eq. 2.85).
This agreement leads to the conclusion that the observed features, namely the extension of the conducting region into the Coulomb diamonds and the current jumps inside the charge transitions, are caused by mechanical oscillations of the carbon nanotube. These oscillations are not driven by an externally applied frequency but originate from the electron transfer through the device.

5.3 Magnetic Field Dependence

In this section the influence of a magnetic field on the nanomechanical oscillations of the carbon nanotube quantum dot is investigated. The applied magnetic field is perpendicular to the substrate surface and therefore also perpendicular to the CNT length.
The measurement focuses on the charge transition already presented in Fig. 5.9a, where the effects of the oscillations are barely visible. Figure 5.11 shows this stability diagram for increasing magnetic field values. For fields up $B = 2.5$ T, the presence of the magnetic field does not seem to have any influence on the shape of the charge transition (cf. panel a - c). For $B \geq 5.0$ T (cf. panel d-f) the magnetic field seems to enhance the current modifications caused by the nanomechanical oscillations. The conducting region which reaches into the otherwise blocked region of the Coulomb diamond grows with increasing magnetic field. Also the current profile inside the charge transition is altered. This can be better observed by taking cuts through the stability diagram at certain bias voltages. Figure 5.12 presents the current in dependence of the gate voltage at a fixed bias voltage of $V_{bias} = 7$ mV (9 mV) in panel a (b). For clarity reasons each current profile was shifted about 50 pA with respect to the previous one, which leads to these so called waterfall plots. In both panels one can see that the shape of the current profile basically stays the same for magnetic fields around $B \leq 2.5$ T. A second maximum at $V_{gate} = -3.816$ V for $V_{bias} = 7$ mV and $V_{gate} = -3.82$ V for $V_{bias} = 9$ mV is emerging for magnetic fields higher than $B = 5$ T and increases

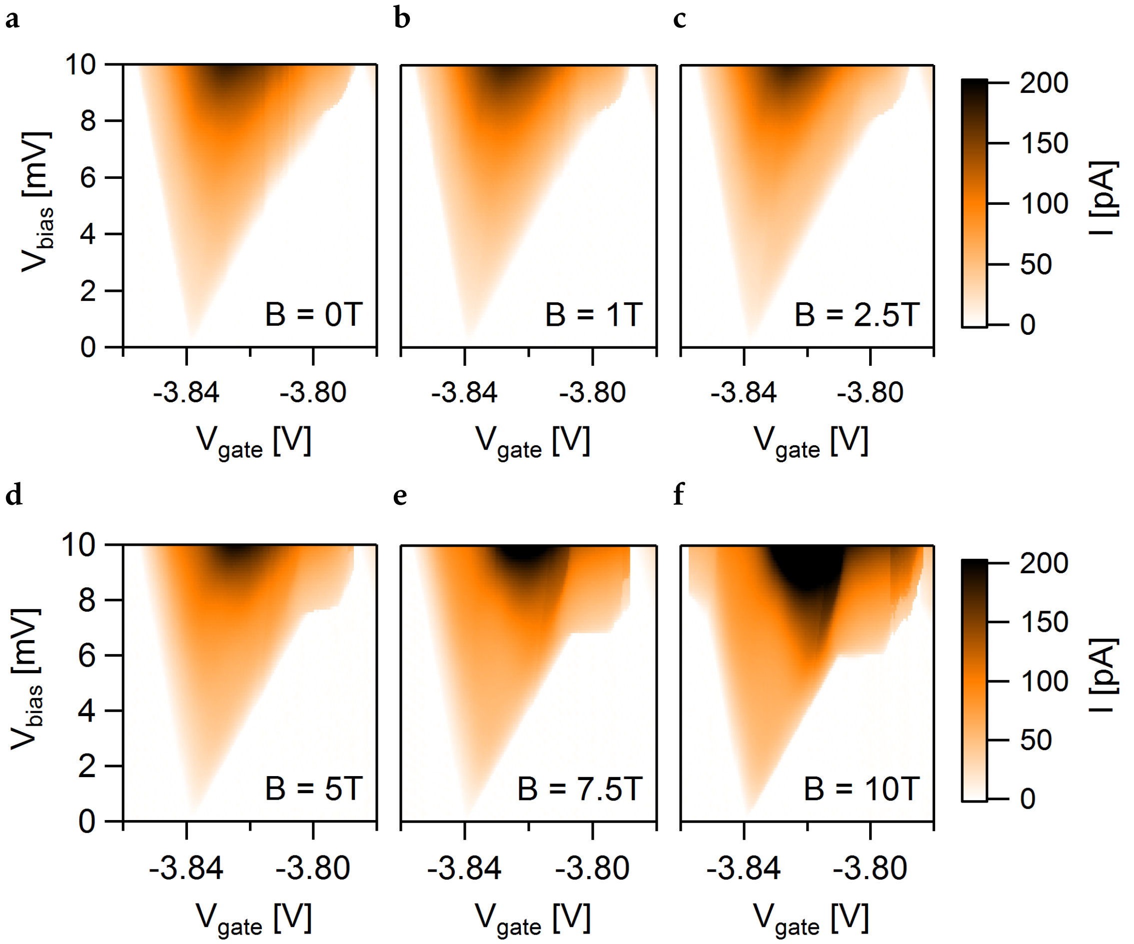

Figure 5.11: Stability diagram for different magnetic fields. **a** $B = 0$ T, **b** $B = 1$ T, **c** $B = 2.5$ T, **d** $B = 5$ T, **e** $B = 7.5$ T and **f** $B = 10$ T applied perpendicular to the sample surface. For $B \geq 5$ T the current modifications due to nanomechanical oscillations increase.

with increasing B fields. For $B \geq 7.5$ T the influence of the magnetic field on the oscillation is large enough, so that the line-cut at $V_{bias} = 7$ mV passes through the extended conducting region, which leads to the increased width of the current profiles. For $B = 10$ T at $V_{bias} = 9$ mV the charge transition also starts to extend on left side. This is visible as the step in the current at $V_{gate} = -3.857$ V for the black line in Fig. 5.12. The current profile through this extended conducting region at $V_{gate} = -3.8$ V is shown in Fig. 5.13. The current step becomes less distinct with higher magnetic fields and the step height increases slightly. Since mechanical oscillations are the cause for the current to reach into the Coulomb diamonds one can assume that in these extended conducting regions the current is limited by the oscillation frequency $I = e \cdot f_{bend}$ and not by the tunneling rate $I = e\Gamma$. Con-

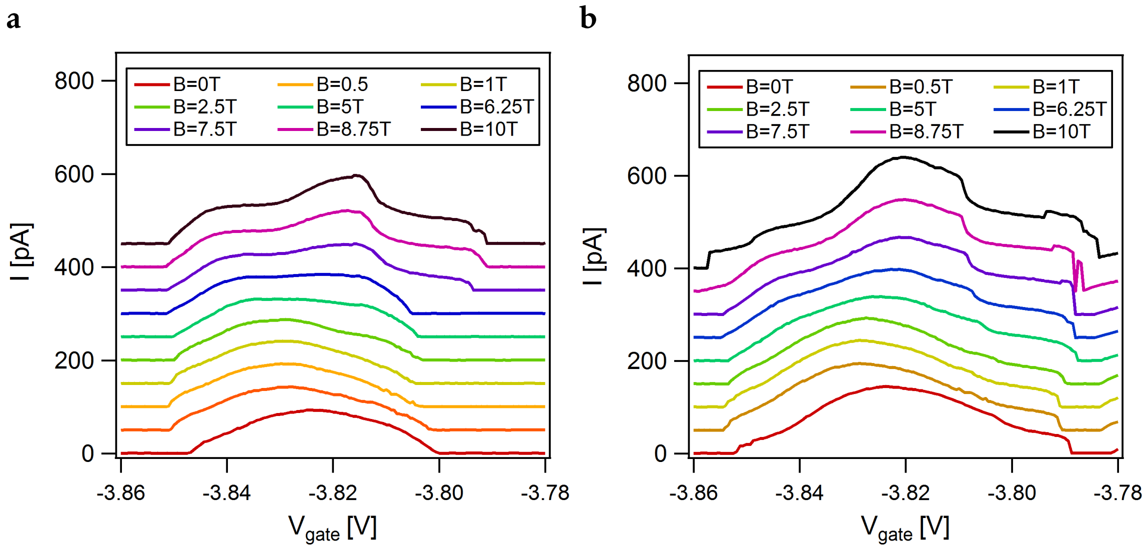

Figure 5.12: Current versus gate voltage at **a** $V_{bias} = 7$ mV and **b** $V_{bias} = 9$ mV for different magnetic fields $0\text{T} \leq B \leq 10\text{T}$. An enhancement in current emerges for $B \geq 5$ T.

sequently the increase of current in the data can be attributed to an increase of the bending frequency f_{bend} with the magnetic field. The measurements show that the applied magnetic field enhances the current modifications caused by the feedback of the nanomechanical oscillations. This contradicts previous findings, where the magnetic field was used to increase the damping in the system [134] and the quality factor decreases with increasing magnetic field [135]. A possible explanation for the observation of this opposite effect in our measurements

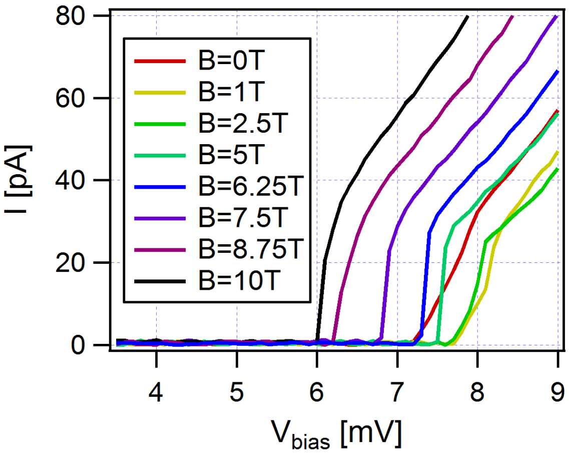

Figure 5.13: Current versus bias voltage at $V_{gate} = -3.8$ V: Current step becomes less distinct with increasing magnetic field. Step size increases only slightly.

is a magnetic field dependence of the tunneling rates. The nanomechanical feedback is strongly dependent on the energy-dependent tunneling rates [121] and the magnetic field seems to increase the transparency of the CNT-contact interface. This is shown in Fig. 5.14a where the maximum current is plotted versus the applied field. The current strongly increases for fields of $B \geq 5$ T. This increase is independent of the bias voltage, since it occurs for $V_{bias} = 9$ mV as well as $V_{bias} = 0.2$ mV. This increase of the tunneling rates for magnetic fields higher than 5 T gives also an explanation for the magnetic field behavior of V_{onset} in Fig. 5.14b, since V_{onset} is inversely proportional to Γ, as already shown in Fig. 5.8.

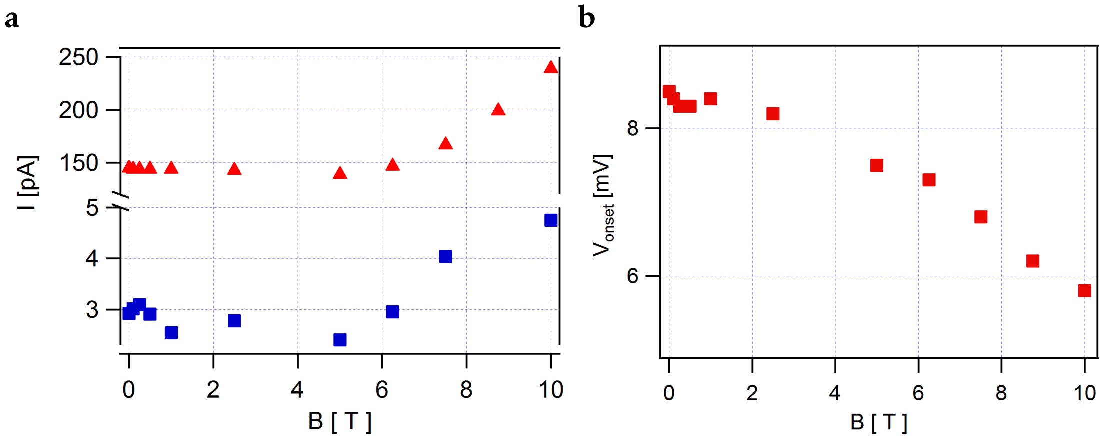

Figure 5.14: **a** Maximum current versus magnetic field for $V_{bias} = 9$ mV (red triangles) and $V_{bias} = 0.2$ mV (blue squares): The maximum current increases for $B \geq 5$ T. **b** Bias voltage versus magnetic field: Bias voltage at which the conducting region reaches into Coulomb diamonds (V_{onset}) decreases for $B \geq 5$ T. The relation $V_{onset} \propto 1/\Gamma$, found in Fig. 5.8, is confirmed.

5.4 Noise Measurements

The features in the investigated CNT device, namely continuously increasing current at the boundaries of the Coulomb diamonds, current jumps inside the charge transitions and areas where the conducting region is extended inside the Coulomb diamonds, can be attributed to a strong feedback between the mechanical CNT-oscillations and the electrical transport behavior. In these nanoelectromechanical systems, super-Poissonian noise with large Fano factors are expected [112,119,121]. The following measurements combine transport and noise measurements, using the setup described in Ch. 3.2. Figure 5.15 shows the data

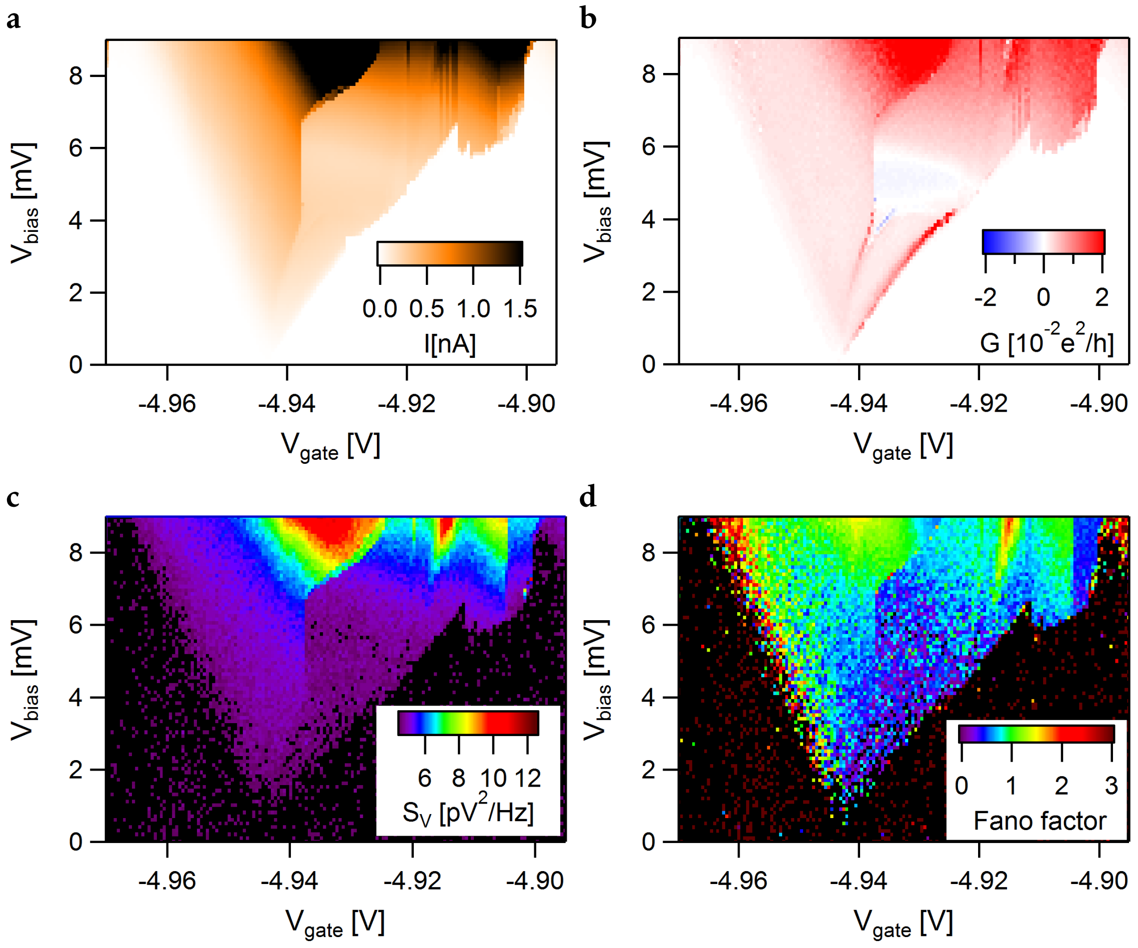

Figure 5.15: Stability diagram of the strongly modified charge transition with no applied magnetic field: **a** Current versus gate and bias voltage. **b** Differential conductance versus gate and bias voltage. **c** Voltage noise S_V versus gate and bias voltage. **d** Fano factor F versus gate and bias voltage.

set obtained by a combined dc, low-frequency conductance and noise measurement on the charge transition shown in Fig. 5.9c for zero magnetic field. Since the measurement time for noise measurements is extremely long, these measurements are more susceptible to gate fluctuations, which might distort the measured data. In this case the resolution was 100×170 pixels with an averaging time of $t = 15$ s, including the time required by the instruments to sweep back to the start values, the total measurement time amounted to 95 hours.

The noise measurements show that the voltage noise S_V (cf. Fig. 5.15c) follows the features, seen in the low frequency transport data (cf. Fig. 5.15a). It shows the current jump inside the charge transition and the extension of the conducting region inside the Coulomb diamond. The measured voltage noise S_V mainly increases with increasing current. Inside this extended region, sharp jumps of the voltage noise are observed. The Fano factor $F = S_I/2eI$, which is the ratio between the current noise S_I and the current I, is displayed in Fig. 5.15d. The most part of the conducting region shows sub Poissonian noise $0.5 \leq F \leq 1$ as expected for sequential tunneling in quantum dot systems [115, 136]. The left side of the transition shows super-Poissonian values with $F \geq 2$, which is a sign of electron bunching [137]. In the conducting region, which reaches into the Coulomb diamonds, the Fano factor jumps from 0.5 to 1. The large current noise and therefore large Fano factors, as reported in [112,119,121], are not observed in our measurements.

The same parameter region was measured again with a magnetic field of $B = 10$ T applied perpendicular to the sample surface. The results are shown in Fig. 5.16. At first one recognizes that the features of the mechanical oscillations are more distinct compared to the case of zero magnetic field. The conducting region reaches further into the Coulomb diamond and the current is larger inside the conducting region with respect to the case without applied magnetic field. This enhancement of the nanomechanical oscillations was already observed in Ch. 5.3. The sudden current jump, on the other hand is no longer visible. The differential conductance is also larger, especially at the right border of the charge transition (cf. Fig. 5.16b). Comparing the measured voltage noise at $B = 10$ T with the zero magnetic field case, one notes a decrease of the maximum value of the voltage noise from 11 $\mathrm{pV}^2/\mathrm{Hz}$ ($B = 0$ T) to 9 $\mathrm{pV}^2/\mathrm{Hz}$ ($B = 10$ T). The sharp current jump feature inside the charge transition as well as the one inside the extended region are not observed at $B = 10$ T. Some disturbances occurred during the measurement, resulting in vertical lines with increased noise (e.g. at $V_{gate} \approx -4.948$ V). The increased differential conductance on the right side of the charge transition border is reappearing as a small line with increased noise in Fig. 5.16c. The Fano factor shows a similar behavior as in the case of no applied magnetic field. Most of the charge transition shows sub-Poissonian noise. At a gate voltage of $V_{gate} \approx -4.93$ V the Fano factor increases to 1 and even gets super-Poissonian on the left border of the charge transition, with values up to 3. As already observed for the voltage noise, the Fano factor is constant inside the extended region of conductance. As stated in Ref. [119, 122], $S_I \simeq I^2 Q/\omega_0$ (Eq. 2.95) gives an estimation of the current noise in the strong feedback region. By plotting S_I/I^2 versus gate and bias value, the behavior of the ratio between the quality factor and the oscillation frequency Q/ω_0 can be examined. In Fig. 5.17 the result is shown. For zero and ten Tesla applied, the values for S_I/I^2 are mostly lower

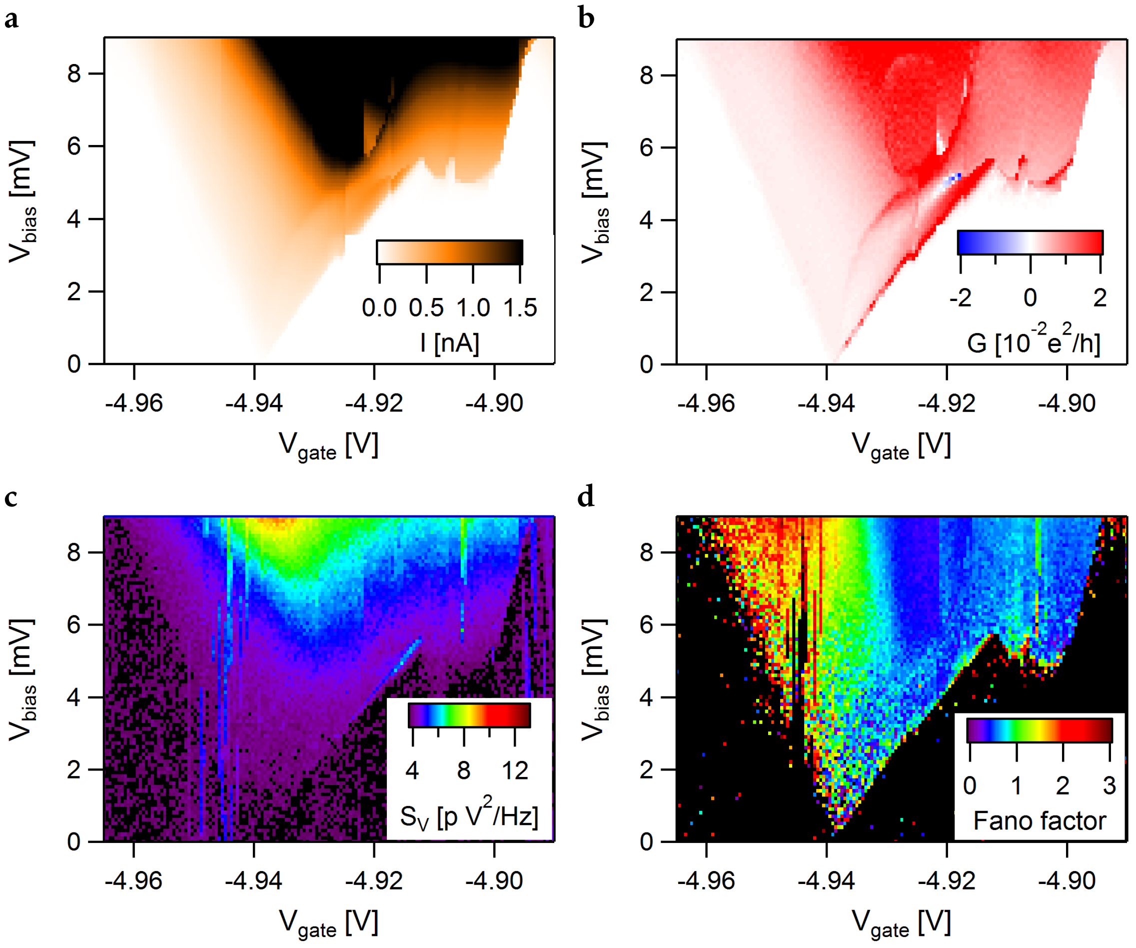

Figure 5.16: Stability diagram of the strongly modified charge transition with an applied magnetic field of $B = 10$ T: **a** Current versus gate and bias voltage. **b** Differential conductance versus gate and bias voltage. **c** Voltage noise S_V versus gate and bias voltage. **d** Fano factor F versus gate and bias voltage.

than $1 \cdot 10^{-9}$ in the conducting region, only at the boundary of the conducting region, the values increase. The reason for this is the smoothly vanishing current at the borders. By assuming again an oscillation frequency in the order of $f_{bend} \approx 0.56$ GHz as extracted in Ch. 5.2, the obtained quality factor is in the order of 1, which is too low since the quality factor has to be sufficiently high to observe effects of the mechanical feedback [119]. Typical quality factors of suspended CNT devices are $Q \geq 10^4$ [102, 134]. Therefore either the assumed frequency is too high or, as already mentioned, the measured current noise is too low. Although the values don't seem to fit, at least a trend can be extracted by comparing the data for $B = 0$ T and $B = 10$ T. In Fig. 5.17c line cuts at a bias

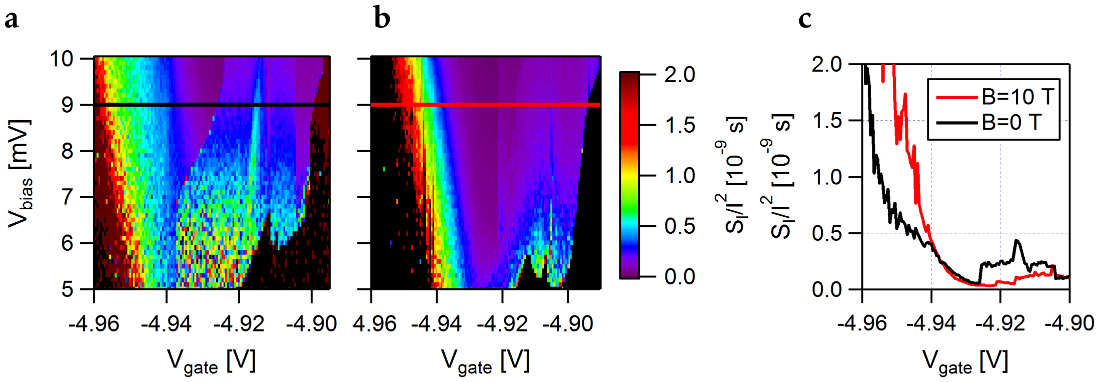

Figure 5.17: Current noise S_I divided by the current squared I^2 versus gate and bias voltage for **a** $B = 0$ T and **b** $B = 10$ T. **c** Line cuts at $V_{bias} = 9$ mV. Inside the conducting region the values of S_I/I^2 are smaller for $B = 10$ T (red line) than for $B = 0$ T (black line), but exceeds at the edge of the charge transition.

value of $V_{bias} = 9$ mV are plotted. For $B = 10$ T (cf. red line) the values of S_I/I^2 lie below the ones for $B = 0$ T. At $V_{gate} \approx -4.93$ V the curves increase for more negative gate voltages, with the red curve increasing faster. The fact, that S_I/I^2 and therefore Q/ω_0 is smaller inside the charge transition if a magnetic field is applied can result from a reduction of the quality factor, as already reported in [134, 135]. In Ref. [120] an exponential increase of the current noise with its

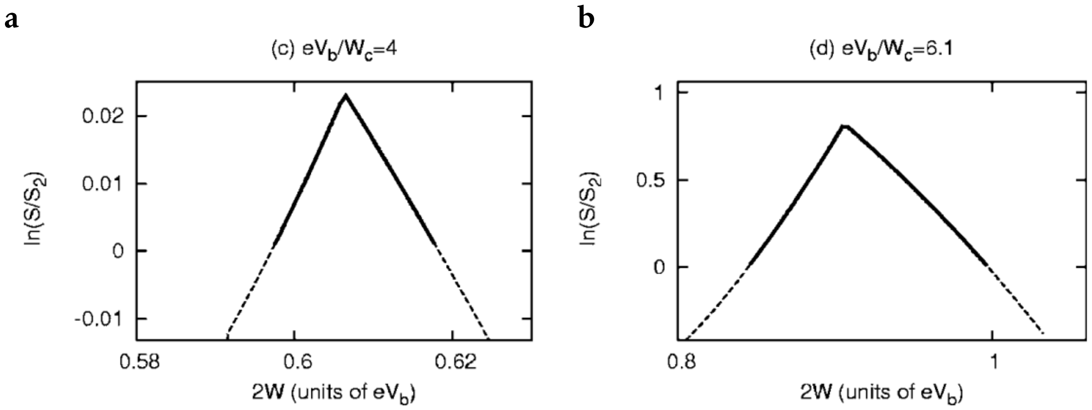

Figure 5.18: Scale of current noise in bistable region at **a** $eV_b/W_c = 4$ and **b** $eV_b/W_c = 6.1$. Solid lines indicate where the telegraph noise is exponentially large. The maximum is at the position where two stable amplitudes have equal probabilities and the current gives a jump. $S_2 = (\Gamma^0)^3 W_c/\lambda\hbar\omega^3 \exp(W_c/\lambda\hbar\omega)$. Maxium value increases stronlgy with eV_b. Taken from [120].

maximum at the position of the current jump is expected. The bistability in this region leads to a telegraph noise since the system randomly switches between two amplitudes, which correspond to distinct values of current. This behavior of the noise is presented in Fig. 5.18a and b for different bias voltage values eV_b/W_c. Here the logarithm of the noise S, scaled by $S_2 = (\Gamma^0)^3 W_c/\lambda\hbar\omega^3 \exp(W_c/\lambda\hbar\omega)$, is plotted versus $2W$, which basically represents eV_{gate}. The noise increases exponentially to its maximum value, where the probabilities for the system to oscillate with the stable amplitudes are equal. At this gate voltage position the current can jump, as described in Ch. 2.6.2. The position of the noise maximum shifts in gate voltage for different bias voltages and the maximum value increases strongly with increasing eV_b. Although the measured values of the current noise are smaller than expected, the overall behavior follows the predictions, depicted in Fig. 5.18. Plotting the current noise S_I in a logarithmic scale with and without applied magnetic field respectively (cf. 5.19a and b), the exponential increase of the noise can be observed. In the case of $B = 0$ T, where a current jump occurs inside the charge transition (cf. Fig. 5.15a), the measured noise has its maximum at the position of these jumps. This maximum shifts from $V_{gate} = -4.937$ V at $V_{bias} = 7$ mV to $V_{gate} = -4.933$ V for $V_{bias} = 9$ mV. The maximum value of the measured current noise increases from $S_I = 2.77 \cdot 10^{-27}$ A^2/Hz at $V_{bias} = 7$ mV to $S_I = 8.46 \cdot 10^{-27}$ A^2/Hz at $V_{bias} = 9$ mV. In the case of $B = 10$ T, no current jumps

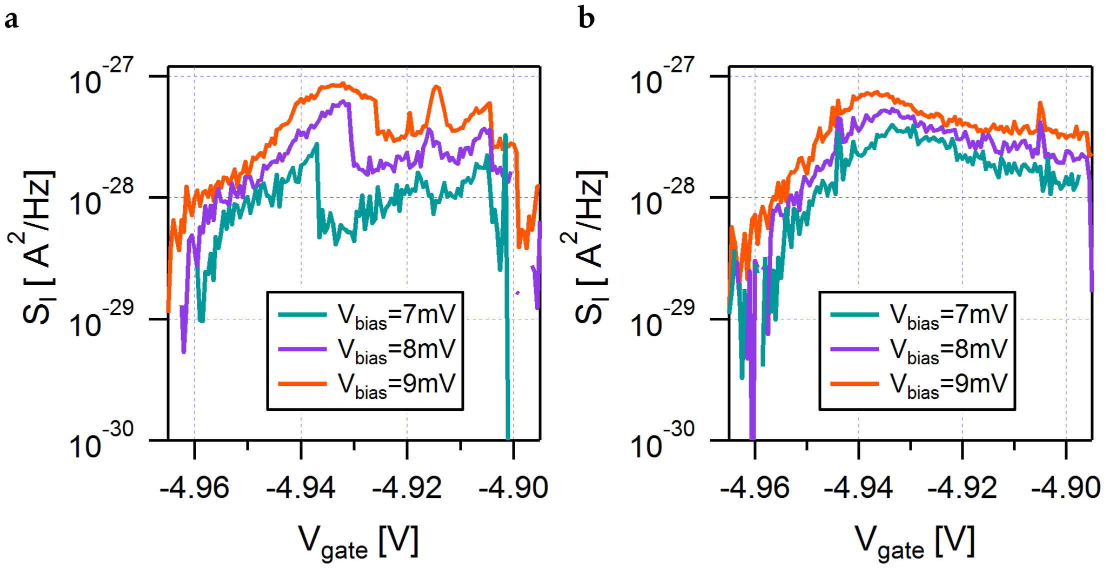

Figure 5.19: Current noise versus gate voltage for different bias voltages. **a** At $B = 0$ T the current noise S_I increases exponentially until V_{gate} reaches the position of current jumps. A sudden reduction of the current leads to a drop in S_I. **b** $B = 10$ T. The maximum current noise is obtained at $V_{gate} \approx -4.935$ V.

occured inside the conducting region (cf. Fig. 5.16), however an exponentially increasing current noise is observed. Here the maximum shifts only slightly from $V_{gate} = -4.934$ V at $V_{bias} = 7$ mV to $V_{gate} = -4.937$ V for $V_{bias} = 9$ mV and increases from $S_I = 3.95 \cdot 10^{-27}$ A^2/Hz at $V_{bias} = 7$ mV to $S_I = 7.42 \cdot 10^{-27}$ A^2/Hz at $V_{bias} = 9$ mV.

5.5 Chapter Summary

In this chapter the influence of nanomechanical oscillations on the transport behavior of a carbon nanotube quantum dot was investigated. For this purpose a CNT was suspended over $Re_{80}Mo_{20}$ contacts, which have a thickness of 100 nm. The investigated sample was only conducting at the hole-side of the CNT and showed a two-fold symmetry. A gap with an energy of $E_{gap} \approx 250$ µeV was observed for bias voltages around zero. Possible reasons for this gap were discussed and the gap was then attributed to the superconducting leads. For positive bias voltages the stability diagram showed that the charge transitions reached into the Coulomb diamonds, where the current is normally blocked. The bias voltage V_{onset}, at which the conducting region reaches into the Coulomb diamonds, decreases with more negative gate voltages. Many charge transitions showed sudden jumps in the current inside the conducting region. The position at which the current drops shifts to smaller gate voltages for higher bias voltages. These current modifications were explained by strong mechanical feedback in the device, caused by nanomechanical oscillations. A frequency of the bending mode was extracted $f_{bend} = 0.56 \pm 0.37$ GHz, which is in agreement with the theoretical estimation for the bending frequency $f_{bend} \approx 0.4$ GHz of a carbon nanotube with a length of $L = 350$ nm. The current jumps are caused by a bistability of the system and occur at positions where the probabilities of two stable oscillation amplitudes are the same. Applying a magnetic field perpendicular to the sample surface showed that for fields higher than $B \geq 5$ T the nanoelectromechanical current modifications get stronger. V_{onset} decreases for $B \geq 5$ T and the height of the current steps increases slightly. This is in contrast to previous findings that show a damping of the nanomechanical oscillations by applying a magnetic field [134] and a decrease of the quality factor [135]. In our measurements a magnetic field dependence of the tunneling rates drastically increases the current for $B \geq 5$ T, which can enhance the current modifications caused by the nanotube's oscillations.

Also noise measurements were performed for $B = 0$ T and $B = 10$ T. These did not show super-Poissonian noise with huge Fano factors as expected in systems with nanomechanical oscillations [112, 119, 121]. For the most part of the conducting region Fano factor values of $0.5 \leq F \leq 1$ were obtained, which are typical for sequential tunneling in quantum dot systems [115, 136]. However an exponential increase of the current noise in dependence of the applied gate voltage was observed, as predicted in Ref. [119–121]. The maximum of the measured current noise S_I was found at the gate position where the current jump occurs. This is also in agreement with the theoretical prediction of [119–121].

6 Summary and Outlook

In this thesis carbon nanotube quantum dots were investigated, where the CVD growth process was performed as the last fabrication step. This method protects the CNT from any contamination caused by the fabrication progress and ideally results in ultra clean samples, as the one presented in Ch. 4. The sample showed a four fold symmetry in the transport data, allowing to count the number of electrons per shell. Suppressed tunneling lines at negative bias voltages for the transition of charge state $0 \rightarrow 1$ and at positive bias voltages for the $3 \rightarrow 4$ transition were observed in combination with a smooth negative differential conductance. These features were attributed to the formation of a dark state in the CNT quantum dot. This is possible when the orbital states are degenerate and the tunneling between the leads and the tube happens locally, allowing an acquisition of an angular momentum dependent tunneling phase. The electrons tunneling from one orbital can interfere destructively with the ones tunneling from the other, leading to a blocked current flow. A Lamb shift-like interaction with the contacts leads to a precession between the coupled and the dark state. This allows electrons to escape the dark state and contribute to transport. Numerical simulations showed an excellent agreement between the measured data and the theoretically predicted effect on the transport behavior.

Growing the carbon nanotubes over a predefined contact structure can also lead to other effects in the transport behavior. Since the CNT is suspended between the two leads, different vibrational modes can be excited, which have different signatures in the transport data. The effect of a strong nanomechanical feedback on electrons tunneling in a quantum dot was investigated in Ch. 5. In this case the carbon nanotube was grown over superconducting contacts. The device showed only conductance at the hole side of the CNT. The measured stability diagram showed that the conducting region of almost all charge transitions is extended into the Coulomb diamonds, where the current is usually blocked. Also sudden jumps in the current were observed. These features were amplified when

a magnetic field higher than $B \geq 5$ T was applied, which contradicts previous findings of magnetic damping of nanomechanical oscillations [134]. The performed noise measurements on these nanomechanical effects did not show the anticipated huge Fano factors [119–121], although the exponential shape of the current noise and the position of its maximum matches the predictions.
These measurement results indicate, that there is more research to be done, experimentally and theoretically. From an experimental point of view, being able to measure directly the bending frequency, its change inside the charge transitions, as well as the quality factor of the nanomechanical system would allow a more detailed analysis and a better comparison with the existing theoretical models. This can be achieved in a setup, as described in [95], where the carbon nanotube is externally driven by a RF antenna and the resonance frequency is measured with a spectrum analyzer.

In case the nanomechanical oscillations are an inconvenient side-effect of the attempt to produce ultra clean carbon nanotube devices, several alternative sample fabrication techniques were proposed lately. One example is the growth of carbon nanotubes on hexagonal boron nitride flakes [138]. The boron nitride is used to prevent substrate induced electrical potential fluctuations, while the remaining sample fabrication is done in the standard top-down fashion. Therefore there are no limitations for the applicable contact materials since no CVD process might alter the properties of the desired materials.
Another promising fabrication method is the stamp transfer of CNTs onto predefined contacts [139, 140]. Here the carbon nanotubes are grown on one chip and are stamped onto another where the desired contact structure was already produced. This way, the contact materials do not need to withstand the CVD process of the nanotube growth. Additionally the nanotubes are not contaminated by any fabrication step. This allows to create complex nanostructures with no restriction on the usable contact materials.
By exploiting one of these fabrication techniques the cleanness of the CNTs and the lack of material restrictions, caused by the CVD process, can be combined. This allows the realization of many interesting experiments. Using ferromagnetic leads with different coercive fields allows the realization of a spin valve device to observe tunneling magneto resistance effects in CNTs [141]. Adding the possibility to perform Shot noise measurements can give even more insight in the investigated systems. Cross correlation experiments on superconductor-hybrid devices like carbon nanotube based Cooper pair splitters, as proposed in [142], might allow to prove the electron entanglement.

A Recipes

In this appendix, the recipes for each sample fabrication step are listed.

A.1 Contact Fabrication

All samples were produced on boron-doped (p++) silicon substrates with an oxide layer of 500 nm. These substrates are bought as typical 4" wavers. With a diamond scraper the waver is cleaved in 9 mm x 9 mm sized chips. All lithography steps are done on these chips, before they are cleaved again in four samples with 4.5 mm x 4.5 mm. This drastically reduces the time needed to produce samples.

- Chip cleaning:
  - oxygen plasma exposure: 1.3 bar for 5 min
  - ultrasonic bath in acetone: 1 min
  - rinse with isopropanol (IPA)
  - blow dry with N_2
- Spin coating:
  - PMMA 200k/3.5% (solvent: anisol)
    Step 1: 3000 rpm, acceleration time:0 s, duration: 5 s
    Step 2: 8000 rpm, acceleration time: 9 s, duration: 30 s
  - bake out on hot plate: 6 min at 150 °C
- Contact lithography:
  - acceleration voltage: V_{acc} = 30 kV
  - contacts:

    - area dose: 250 µC/cm^2
    - spacing: 8 nm
    - aperture: 20 µm
  - leads and bond pads:
    - area dose: 400 µC/cm^2
    - spacing: 30 nm
    - aperture: 120 µm
  - development: MIBK:IPA (3:1) for 2 min, IPA for 30 s
  - blow dry with N_2
- Metalization:
  - DC sputtering of Re:
    - sputtering power: 75 W
    - rate: ~1.5 Å/s
    - thickness: 20 nm
  - DC sputtering of Ti:
    - sputtering power: 25 W
    - rate: ~0.13 Å/s
    - thickness: 4 nm
  - DC sputtering of Pt:
    - sputtering power: 50 W
    - rate: ~1.47 Å/s
    - thickness: 80 nm
  - electron beam evaporation of Co:
    - current: ~225 mA
    - rate: ~0.42 Å/s
    - thickness: 40 nm
- Lift-off:
  - bath in 60 °C warm acetone for several hours
  - rinse with isopropanol (IPA)
  - blow dry with N_2

A.2 CNT synthesis

A.2.1 Catalyst dots

- Chip cleaning:
    - bath in acetone: 1 min
    - rinse with IPA
    - blow dry with N_2
- Spin coating:
    - layer 1: PMMA 200k/9% (solvent: anisol)
      Step 1: 3000 rpm, acceleration time: 0 s, duration: 5 s
      Step 2: 8000 rpm, acceleration time: 9 s, duration: 30 s
    - prebaking on hot plate: 6 min at 150 °C
    - layer 2: PMMA 950k/2% (solvent: anisol)
      Step 1: 3000 rpm, acceleration time: 0 s, duration: 5 s
      Step 2: 8000 rpm, acceleration time: 9 s, duration: 30 s
    - prebaking on hot plate: 6 min at 150 °C
- Catalyst dot lithography:
    - acceleration voltage: $V_{acc} = 30$ kV
    - area dose: 350 µC/cm^2
    - spacing: 8 nm
    - aperture: 30 µm
    - development: MIBK:IPA (3:1) for 90 s, IPA for 30 s
    - dry blowing with N_2
- Cleave the chip in 4 pieces with 4.5 mm x 4.5 mm each
- Catalyst deposition:
    - catalyst suspension:
        - $(Fe(NO_3)_3) \cdot 9H_2O$: 40 mg
        - Al_2O_3 nanoparticles (diameter 14 nm): 30 mg
        - $[CH_3COCH{=}C(O\text{-})CH_3]_2MoO_2$: 10 mg

    - methanol: 30 ml
  - catalyst deposition:
    - mix in ultrasonic bath for at least 1 hour
    - deposite few drops of suspension on sample
    - blow dry with N_2 after 2-3 seconds
    - bake out on hot plate: 5 min at 150 °C
  - catalyst lift-off:
    - heat a beaker with acetone to 60 °C
    - put a magnetic stirrer inside
    - hold the sample upside-down in the acetone while stirring for 2 min
    - rinse with IPA
    - blow dry with N_2

A.2.2 CVD growth

- mount the sample on a quartz holder and place it the middle of a 2" quartz tube. Assure that the sample is positioned where the temperature sensor of the CVD furnace is.
- connect quartz tube with gas lines by cups
- open gas bottles and valves for methane, hydrogen and argon gas
- flush the tube with all valves open and manual scale set at maximum values for 2 min
- reduce argon flow to 14 on the manual scale
- set the flow rates for methane and hydrogen using computer controlled MFCs:
  - CH_4: 20 sccm
  - N_2: 10 sccm
- close the valve for methane gas
- set temperature of the furnace to 850 °C and close the lid

- when the furnace reached 850 °C, close the valve for argon and open the valve for methane
- growth time: 20 min
- when the CNT growth is finished, close methane and open argon
- all valves can be closed and the sample can be demounted, once the temperature of the furnace is below 100 °C

Bibliography

[1] S. Iijama, “Helical microtubules of graphitic carbon,” *Nature*, vol. 354, no. 6348, p. 56, 1991.

[2] D. S. Bethune, C. H. Kiang, M. S. de Vries, G. Gorman, R. Savoy, J. Vazquez, and R. Beyers, “Cobalt-catalysed growth of carbon nanotubes with single-atomic-layer walls,” *Nature*, vol. 363, no. 6430, p. 605, 1993.

[3] S. J. Tans, M. Devoret, H. Dai, a. Thess, R. Smalley, L. J. Geerligs, and C. Dekker, “Individual Single-Wall Carbon Nanotubes As Quantum Wires,” *Nature*, vol. 386, p. 474, 1997.

[4] S. J. Tans, A. R. M. Verschueren, and C. Dekker, “Room-temperature transistor based on a single carbon nanotube,” *Nature*, vol. 393, no. 6680, p. 49, 1998.

[5] M. W. Bockrath, D. H. Cobden, J. Lu, A. G. Rinzler, R. E. Smalley, L. Balents, and P. L. McEuen, “Luttinger-liquid behaviour in carbon nanotubes,” *Nature*, vol. 397, no. 6720, p. 598, 1999.

[6] H. W. C. Postma, “Carbon Nanotube Single-Electron Transistors at Room Temperature,” *Science*, vol. 293, no. 5527, p. 76, 2001.

[7] J. Cao, Q. Wang, and H. Dai, “Electron transport in very clean, as-grown suspended carbon nanotubes.,” *Nat. Mater.*, vol. 4, no. 10, p. 745, 2005.

[8] W. Liang, M. Bockrath, D. Bozovic, J. H. Hafner, M. Tinkham, and H. Park, “Fabry-Perot interference in a nanotube electron waveguide,” *Nature*, vol. 411, no. 6838, p. 665, 2001.

[9] A. Jensen, J. R. Hauptmann, J. Nygård, and P. E. Lindelof, “Magnetoresistance in ferromagnetically contacted single-wall carbon nanotubes,” *Physical Review B*, vol. 72, p. 035419, 2005.

[10] A. F. Morpurgo, "Gate-Controlled Superconducting Proximity Effect in Carbon Nanotubes," *Science*, vol. 286, no. 5438, p. 263, 1999.

[11] A. Y. Kasumov, "Supercurrents Through Single-Walled Carbon Nanotubes," *Science*, vol. 284, no. 5419, p. 1508, 1999.

[12] Y. M. Blanter and M. Buttiker, "Shot noise in mesoscopic conductors," *Physics Reports*, vol. 336, no. 1, pp. 1–166, 2000.

[13] C. D. Glattli, "Quantum shot noise of conductors and general noise measurement methods," *European Physical Journal: Special Topics*, vol. 172, no. 1, p. 163, 2009.

[14] Y. M. Blanter, *Recent Advances in Studies of Current Noise*. Berlin, Heidelberg: Springer Berlin Heidelberg, 2011.

[15] J. P. Lu, "Elastic properties of carbon nanotubes and nanoropes," *Phys. Rev. Lett.*, vol. 79, p. 1297, 1997.

[16] A. K. Hüttel, G. A. Steele, B. Witkamp, M. Poot, L. P. Kouwenhoven, and H. S. J. van der Zant, "Carbon Nanotubes as Ultrahigh Quality Factor Mechanical Resonators," *Nano Letters*, vol. 9, no. 7, p. 2547, 2009.

[17] J. Moser, A. Eichler, J. Güttinger, M. I. Dykman, and A. Bachtold, "Nanotube mechanical resonators with quality factors of up to 5 million," *Nature Nanotechnology*, vol. 9, no. 12, p. 1007, 2014.

[18] B. Lassagne, D. Garcia-Sanchez, A. Aguasca, and A. Bachtold, "Ultrasensitive Mass Sensing with a Nanotube Electromechanical Resonator," *Nano Letters*, vol. 8, no. 11, p. 3735, 2008.

[19] D. Mamaluy and X. Gao, "The fundamental downscaling limit of field effect transistors," *Applied Physics Letters*, vol. 106, no. 19, p. 193503, 2015.

[20] G. E. Moore, "Cramming More Components onto Integrated Circuits," *Electronics*, vol. 38, no. 8, pp. 114–117, 1965.

[21] C. Qiu, Z. Zhang, M. Xiao, Y. Yang, D. Zhong, and L.-M. Peng, "Scaling carbon nanotube complementary transistors to 5-nm gate lengths," *Science*, vol. 355, pp. 271–276, 2017.

[22] A. Graham, G. Duesberg, W. Hoenlein, F. Kreupl, M. Liebau, R. Martin, B. Rajasekharan, W. Pamler, R. Seidel, W. Steinhoegl, and E. Unger, "How

do carbon nanotubes fit into the semiconductor roadmap?," *Applied Physics A*, vol. 80, no. 6, pp. 1141–1151, 2005.

[23] R. Saito, G. Dresselhaus, and M. S. Dresselhaus, *Physical Properties of Carbon Nanotubes*. London: Imperial College Press, 1998.

[24] S. Ilani and P. L. Mceuen, "Electron Transport in Carbon Nanotubes," *Annu. Rev. Condens. Matter Phys*, vol. 1, pp. 1–25, 2010.

[25] E. A. Laird, F. Kuemmeth, G. A. Steele, K. Grove-Rasmussen, J. Nygard, K. Flensberg, and L. P. Kouwenhoven, "Quantum transport in carbon nanotubes," *Reviews of Modern Physics*, vol. 87, no. 3, p. 703, 2015.

[26] J. C. Charlier, X. Blase, and S. Roche, "Electronic and transport properties of nanotubes," *Reviews of Modern Physics*, vol. 79, no. 2, p. 677, 2007.

[27] K. S. Novoselov, A. K. Geim, S. Morozov, D. Jiang, Y. Zhang, S. V. Dubonos, I. V. Grigorieva, and A. A. Firsov, "Electric Field Effect in Atomically Thin Carbon Films," *Science*, vol. 306, no. 5696, p. 666, 2004.

[28] M. S. Dresselhaus, G. Dresselhaus, and P. Avouris, *Carbon Nanotubes - Synthesis, Structure, Properties, and Applications*. Berlin: Springer Verlag, 2001.

[29] M. Büttiker, Y. Imry, R. Landauer, and S. Pinhas, "Generalized many-channel conductance formula with application to small rings," *Physical Review B*, vol. 31, no. 10, p. 6207, 1985.

[30] A. Dirnaichner, M. del Valle, K. J. G. Götz, F. J. Schupp, N. Paradiso, M. Grifoni, C. Strunk, and A. K. Hüttel, "Secondary Electron Interference from Trigonal Warping in Clean Carbon Nanotubes," *Phys. Rev. Lett.*, vol. 117, p. 166804, 2016.

[31] Z. M. Wang, *Self-Assembled Quantum Dots*. No. 1, 2008.

[32] A. Wild, J. Sailer, J. Nützel, G. Abstreiter, S. Ludwig, and D. Bougeard, "Electrostatically defined quantum dots in a Si/SiGe heterostructure," *New Journal of Physics*, vol. 12, no. 11, p. 113019, 2010.

[33] M. T. Björk, C. Thelander, A. E. Hansen, L. E. Jensen, M. W. Larsson, L. R. Wallenberg, and L. Samuelson, "Few-Electron Quantum Dots in Nanowires," *Nano Letters*, vol. 4, no. 9, p. 1621, 2004.

[34] A. K. Hüttel, *Gekoppelte Quantenpunkte im Bereich niedrigster Elektronenzahlen*. PhD thesis, Ludwig-Maximilians-Universität München, 2005.

[35] C. W. J. Beenakker, "Theory of Coulomb-blockade oscillations in the conductance of a quantum dot," *Physical Review B*, vol. 44, no. 4, p. 1646, 1991.

[36] L. P. Kouwenhoven and C. Marcus, "Quantum dots," *Physics World*, vol. 11, no. 6, p. 35, 1998.

[37] L. P. Kouwenhoven, N. C. van der Vaart, A. T. Johnson, W. Kool, C. J. P. M. Harmans, J. G. Williamson, A. A. M. Staring, and C. T. Foxon, "Single electron charging effects in semiconductor quantum dots," *Zeitschrift für Physik B Condensed Matter*, vol. 85, p. 367, 1991.

[38] M. Gaaß, *The Kondo effect in single wall carbon nanotubes with ferromagnetic contacts*. PhD thesis, Universität Regensburg, 2011.

[39] U. Meirav, P. L. McEuen, M. A. Kastner, E. B. Foxman, A. Kumar, and S. J. Wind, "Conductance oscillations and transport spectroscopy of a quantum dot," *Zeitschrift für Physik B Condensed Matter*, vol. 85, no. 3, p. 357, 1991.

[40] H. Grabert, "Single charge tunneling: A brief introduction," *Zeitschrift für Physik B Condensed Matter*, vol. 85, no. 3, p. 319, 1991.

[41] K. Grove-Rasmussen, H. I. Jørgensen, and P. E. Lindelof, "Fabry-Perot interference, Kondo effect and Coulomb blockade in carbon nanotubes," *Physica E: Low-Dimensional Systems and Nanostructures*, vol. 40, no. 1, p. 92, 2007.

[42] D. R. Schmid, P. L. Stiller, C. Strunk, and A. K. Hüttel, "Liquid-induced damping of mechanical feedback effects in single electron tunneling through a suspended carbon nanotube," *Applied Physics Letters*, vol. 107, no. 12, p. 123110, 2015.

[43] D. R. Schmid, S. Smirnov, M. Margańska, A. Dirnaichner, P. L. Stiller, M. Grifoni, A. K. Hüttel, and C. Strunk, "Broken SU(4) symmetry in a Kondo-correlated carbon nanotube," *Physical Review B*, vol. 91, p. 155435, Apr 2015.

[44] M. Gaaß, A. K. Hüttel, K. Kang, I. Weymann, J. Von Delft, and C. Strunk, "Universality of the Kondo effect in quantum dots with ferromagnetic leads," *Physical Review Letters*, vol. 107, no. 17, p. 2, 2011.

[45] P. Lindelof, J. Borggreen, A. Jensen, J. Nygård, and P. Poulsen, "Electron spin in single wall carbon nanotubes," *Physica Scripta*, no. T-102, p. 22, 2002.

[46] T. S. Jespersen, K. Grove-Rasmussen, J. Paaske, K. Muraki, T. Fujisawa, J. Nygård, and K. Flensberg, "Gate-dependent spin–orbit coupling in multielectron carbon nanotubes," *Nature Physics*, vol. 7, no. 4, p. 348, 2011.

[47] S. Sapmaz, P. Jarillo-Herrero, J. Kong, C. Dekker, L. P. Kouwenhoven, and H. S. J. van der Zant, "Electronic excitation spectrum of metallic carbon nanotubes," *Physical Review B*, vol. 71, no. 15, p. 4, 2005.

[48] Y. Oreg, K. Byczuk, and B. I. Halperin, "Spin configurations of a carbon nanotube in a nonuniform external potential," *Physical Review Letters*, vol. 85, no. 2, p. 365, 2000.

[49] S. Sapmaz, P. Jarillo-Herrero, L. P. Kouwenhoven, and H. S. J. van der Zant, "Quantum dots in carbon nanotubes," *Semiconductor Science and Technology*, vol. 21, no. 11, p. S52, 2006.

[50] D. H. Cobden and J. Nygård, "Shell Filling in Closed Single-Wall Carbon Nanotube Quantum Dots," *Physical Review Letters*, vol. 89, no. 4, p. 046803, 2002.

[51] M. Niklas, S. Smirnov, D. Mantelli, M. Margańska, N.-V. Nguyen, W. Wernsdorfer, J.-P. Cleuziou, and M. Grifoni, "Blocking transport resonances via Kondo many-body entanglement in quantum dots," *Nature Communications*, vol. 7, p. 12442, 2016.

[52] M. A. Kastner, "Artificial Atoms," *Physics Today*, vol. 46, no. 1, p. 24, 1993.

[53] T. Brandes and F. Renzoni, "Current switch by coherent trapping of electrons in quantum dots," *Physical Review Letters*, vol. 85, no. 19, p. 4148, 2000.

[54] B. J. Dalton and M. Gagen, "Strongly driven Stark coupled three-level systems and transitions at the Rabi frequency," *J. Phys. B: At. Mol. Phys.*, vol. 18, p. 4403, 1985.

[55] B. J. Dalton, R. McDuff, and P. L. Knight, "Coherent population trapping: Two unequal phase fluctuating laser fields," *Optica Acta*, vol. 32, no. 1, p. 61, 1985.

[56] R. M. Whitley and C. R. Stroud, "Double optical resonance," *Physical Review A*, vol. 14, no. 4, p. 1498, 1976.

[57] G. Alzetta, A. Gozzini, L. Moi, and G. Orriols, "An experimental method for the observation of r.f. transitions and laser beat resonances in oriented Na vapour," *Il Nuovo Cimento B Series 11*, vol. 36, no. 1, p. 5, 1976.

[58] E. Arimondo and G. Orriols, "Nonabsorbing atomic coherences by coherent two-photon transitions in a three-level optical pumping," *Lettere Al Nuovo Cimento Series 2*, vol. 17, no. 10, p. 333, 1976.

[59] R. G. Brewer and E. L. Hahn, "Coherent two-photon processes: Transient and steady-state cases," *Phys. Rev. A*, vol. 11, p. 1641, 1975.

[60] B. Michaelis, C. Emary, and C. W. J. Beenakker, "All-electronic coherent population trapping in quantum dots," *Europhysics Letters (EPL)*, vol. 73, no. 5, p. 677, 2006.

[61] A. Donarini, M. Niklas, M. Schafberger, N. Paradiso, C. Strunk, and M. Grifoni, "Dark states in a carbon nanotube quantum dot," *arXiv:1804.02234v1*, 2018.

[62] M. Büttiker, "Scattering Theory of Thermal and Excess Noise in Open Conductors," *Phys. Rev. Lett.*, vol. 65, no. 23, pp. 2901–2904, 1990.

[63] S. Oberholzer, M. Henny, C. Strunk, C. Schönenberger, T. Heinzel, K. Ensslin, and M. Holland, "The Hanbury Brown and Twiss Experiment with fermions," *Science*, vol. 284, no. 5412, pp. 296–298, 1999.

[64] D. Steininger, *Shot Noise Detection in Carbon Nanotube Quantum Dots*. PhD thesis, Universität Regensburg, 2017.

[65] G.-E. Onac, *High Frequency Noise Detection in Mesoscopic Devices*. PhD thesis, TU Delft, 2005.

[66] J. B. Johnson, "Thermal Agitation of Electricity in Conductors," *Physical Review*, vol. 32, p. 97, 1928.

[67] H. Nyquist, "Thermal agitation of electric charge in conductors," *Physical Review*, vol. 32, no. 1, p. 110, 1928.

[68] S. Kogan, *Electronic Noise and Fluctuations in Solids*. Cambridge University Press, 1996.

[69] W. Schottky, "Über spontane Stromschwankungen in verschiedenen Elektrizitätsleitern," *Annalen der Physik*, vol. 362, p. 541, 1918.

[70] U. Fano, "Ionization Yield of Radiations. II. The Fluctuations of the Number of Ions," *Physical Review*, vol. 72, no. 1, p. 26, 1947.

[71] B. J. van Wees, H. van Houten, C. W. J. Beenakker, J. G. Williamson, L. P. Kouwenhoven, D. van der Marel, and C. T. Foxon, "Quantized conductance of point contacts in a two-dimensional electron gas," *Physical Review Letters*, vol. 60, no. 9, p. 848, 1988.

[72] M. Reznikov, M. Heiblum, H. Shtrikman, and D. Mahalu, "Temporal correlation of electrons: Suppression of shot noise in a ballistic quantum point contact," *Physical Review Letters*, vol. 75, no. 18, p. 3340, 1995.

[73] A. Kumar, L. Saminadayar, D. C. Glattli, Y. Jin, and B. Etienne, "Experimental Test of the Quantum Shot Noise Reduction Theory," *Physical Review Letters*, vol. 76, no. 15, p. 2778, 1996.

[74] H. Birk, M. J. De Jong, and C. Schönenberger, "Shot-noise suppression in the single-electron tunneling regime," *Physical Review Letters*, vol. 75, no. 8, p. 1610, 1995.

[75] A. Nauen, I. Hapke-Wurst, F. Hohls, U. Zeitler, R. J. Haug, and K. Pierz, "Shot noise in self-assembled InAs quantum dots," *Physical Review B*, vol. 66, no. 16, p. 161303, 2002.

[76] A. Nauen, F. Hohls, N. Maire, K. Pierz, and R. J. Haug, "Shot noise in tunneling through a single quantum dot," *Physical Review B*, vol. 70, p. 033305, 2004.

[77] C. A. Merchant and N. Marković, "Current and shot noise measurements in a carbon nanotube-based spin diode (invited)," *Journal of Applied Physics*, vol. 105, no. 7, p. 07C711, 2009.

[78] C. W. J. Beenakker and M. Büttiker, "Suppression of shot noise in metallic diffusive conductors.," *Physical review. B, Condensed matter*, vol. 46, no. 3, p. 1889, 1992.

[79] R. J. Schoelkopf, P. J. Burke, A. A. Kozhevnikov, D. E. Prober, and M. J. Rooks, "Frequency Dependence of Shot Noise in a Diffusive Mesoscopic Conductor," *Physical Review Letters*, vol. 78, no. 17, p. 3370, 1997.

[80] Y. Zhang, L. DiCarlo, D. T. McClure, M. Yamamoto, S. Tarucha, C. M. Marcus, M. P. Hanson, and A. C. Gossard, "Noise Correlations in a Coulomb-Blockaded Quantum Dot," *Physical Review Letters*, vol. 99, no. 3, p. 036603, 2007.

[81] R. de Picciotto, M. Reznikov, M. Heiblum, V. Umansky, G. Bunin, and D. Mahalu, "Direct observation of a fractional charge," *Physica B: Condensed Matter*, vol. 249-251, p. 395, 1998.

[82] L. Saminadayar, D. C. Glattli, Y. Jin, and B. Etienne, "Observation of the e/3 Fractionally Charged Laughlin Quasiparticle," *Physical Review Letters*, vol. 79, no. 13, p. 2526, 1997.

[83] Y. Ronen, Y. Cohen, J.-H. Kang, A. Haim, M.-T. Rieder, M. Heiblum, D. Mahalu, and H. Shtrikman, "Charge of a quasiparticle in a superconductor," *Proceedings of the National Academy of Sciences*, vol. 113, no. 7, p. 1743, 2016.

[84] X. Jehl, P. Payet-Burin, C. Baraduc, R. Calemczuk, and M. Sanquer, "Andreev Reflection Enhanced Shot Noise in Mesoscopic SNS Junctions," *Physical Review Letters*, vol. 83, no. 8, p. 1660, 1999.

[85] R. J. Schoelkopf, A. A. Clerk, S. M. Girvin, K. W. Lehnert, and M. H. Devoret, *Qubits as Spectrometers of Quantum Noise.* Springer Netherlands, 2003.

[86] D. C. Glattli, P. Jacques, A. Kumar, P. Pari, and L. Saminadayar, "A noise detection scheme with 10 mK noise temperature resolution for semiconductor single electron tunneling devices," *Journal of Applied Physics*, vol. 81, no. 11, p. 7350, 1997.

[87] E. Onac, F. Balestro, B. Trauzettel, C. F. J. Lodewijk, and L. P. Kouwenhoven, "Shot-Noise Detection in a Carbon Nanotube Quantum Dot," *Phys. Rev. Lett.*, vol. 96, p. 026803, 2006.

[88] M. Hashisaka, Y. Yamauchi, S. Nakamura, S. Kasai, K. Kobayashi, and T. Ono, "Measurement for quantum shot noise in a quantum point contact at low temperatures," *Journal of Physics: Conference Series*, vol. 109, p. 012013, 2008.

[89] M. Hashisaka, Y. Yamauchi, S. Nakamura, S. Kasai, T. Ono, and K. Kobayashi, "Bolometric detection of quantum shot noise in coupled mesoscopic systems," *Physical Review B*, vol. 78, no. 24, p. 241303, 2008.

[90] L. DiCarlo, Y. Zhang, D. T. McClure, C. M. Marcus, L. N. Pfeiffer, and K. W. West, “System for measuring auto- and cross correlation of current noise at low temperatures,” *Review of Scientific Instruments*, vol. 77, no. 7, p. 073906, 2006.

[91] D. T. McClure, L. DiCarlo, Y. Zhang, H.-A. Engel, C. M. Marcus, M. P. Hanson, and A. C. Gossard, “Tunable Noise Cross Correlations in a Double Quantum Dot,” *Phys. Rev. Lett.*, vol. 98, p. 056801, 2007.

[92] B. Witkamp, M. Poot, and H. S. J. Van Der Zant, “Bending-mode vibration of a suspended nanotube resonator,” *Nano Letters*, vol. 6, no. 12, p. 2904, 2006.

[93] R. G. Knobel and A. N. Cleland, “Nanometre-scale displacement sensing using a single electron transistor,” *Nature*, vol. 424, no. 6946, p. 291, 2003.

[94] M. D. LaHaye, O. Buu, B. Camarota, and K. C. Schwab, “Approaching the Quantum Limit of a Nanomechanical Resonator,” *Science*, vol. 304, no. 5667, p. 74, 2004.

[95] D. R. Schmid, *Suspended Carbon Nanotubes as Electronical and Nano-Electro-Mechanical Hybrid Systems in the Quantum Limit*. PhD thesis, Universität Regensburg, 2014.

[96] A. K. Hüttel, M. Poot, B. Witkamp, and H. S. J. van der Zant, “Nanoelectromechanics of suspended carbon nanotubes,” *New Journal of Physics*, vol. 10, no. 9, p. 095003, 2008.

[97] N. Anderson, A. Hartschuh, and L. Novotny, “Chirality changes in carbon nanotubes studied with near-field Raman spectroscopy,” *Nano Letters*, vol. 7, no. 3, p. 577, 2007.

[98] M. S. Dresselhaus and P. C. Eklund, “Phonons in carbon nanotubes,” *Advances in Physics*, vol. 49, no. 6, p. 705, 2000.

[99] B. J. LeRoy, S. G. Lemay, J. Kong, and C. Dekker, “Electrical generation and absorption of phonons in carbon nanotubes,” *Nature*, vol. 432, no. 7015, p. 371, 2004.

[100] E. Mariani and F. von Oppen, “Electron-vibron coupling in suspended carbon nanotube quantum dots,” *Physical Review B*, vol. 80, p. 155411, 2009.

[101] A. K. Hüttel, B. Witkamp, M. Leijnse, M. R. Wegewijs, and H. S. J. van der Zant, "Pumping of Vibrational Excitations in the Coulomb-Blockade Regime in a Suspended Carbon Nanotube," *Physical Review Letters*, vol. 102, p. 225501, jun 2009.

[102] J. O. Island, V. Tayari, A. C. McRae, and A. R. Champagne, "Few-hundred ghz carbon nanotube nanoelectromechanical systems (nems)," *Nano Letters*, vol. 12, no. 9, p. 4564, 2012. PMID: 22888989.

[103] B. Reulet, A. Kasumov, M. Kociak, R. Deblock, I. Khodos, Y. Gorbatov, V. Volkov, C. Journet, and H. Bouchiat, "Acoustoelectric effects in carbon nanotubes," *Physical review letters*, vol. 85, no. 13, p. 2829, 2000.

[104] S. Braig and K. Flensberg, "Vibrational sidebands and dissipative tunneling in molecular transistors," *Physical Review B*, vol. 68, p. 205324, 2003.

[105] X. H. Qiu, G. V. Nazin, and W. Ho, "Vibronic States in Single Molecule Electron Transport," *Phys. Rev. Lett.*, vol. 92, p. 206102, 2004.

[106] H. Park, J. Park, A. K. L. Lim, E. H. Anderson, A. P. Alivisatos, and P. L. McEuen, "Nanomechanical oscillations in a single C-60 transistor," *Nature*, vol. 407, p. 57, 2000.

[107] K. C. Nowack and M. R. Wegewijs, "Vibration-assisted tunneling through competing molecular states," *arXiv:cond-mat/0506552*, 2005.

[108] D. Boese and H. Schoeller, "Influence of nano-mechanical properties on single electron tunneling: A vibrating Single-Electron Transistor," *EPL (Europhysics Letters)*, vol. 54, no. 5, p. 668, 2000.

[109] K. D. McCarthy, N. Prokof'ev, and M. T. Tuominen, "Incoherent dynamics of vibrating single-molecule transistors," *Physical Review B*, vol. 67, p. 245415, 2003.

[110] J. Franck, "Elementary processes of photochemical reactions," *Trans. Faraday Soc.*, no. 1923, p. 536, 1924.

[111] E. Condon, "A theory of intensity distribution in band systems," *Physical Review*, vol. 28, no. 6, p. 1182, 1926.

[112] J. Koch and F. von Oppen, "Franck-Condon Blockade and Giant Fano Factors in Transport through Single Molecules," *Phys. Rev. Lett.*, vol. 94, p. 206804, 2005.

[113] J. Koch, F. von Oppen, and A. V. Andreev, "Theory of the Franck-Condon blockade regime," *Physical Review B*, vol. 74, p. 205438, 2006.

[114] R. Leturcq, C. Stampfer, K. Inderbitzin, L. Durrer, C. Hierold, E. Mariani, M. G. Schultz, F. Von Oppen, and K. Ensslin, "Franck-Condon blockade in suspended carbon nanotube quantum dots," *Nature Physics*, vol. 5, no. 5, p. 327, 2009.

[115] A. Thielmann, M. H. Hettler, J. König, and G. Schön, "Shot noise in tunneling transport through molecules and quantum dots," *Physical Review B*, vol. 68, no. 11, p. 115105, 2003.

[116] T. Hasler, M. Jung, V. Ranjan, G. Puebla-Hellmann, A. Wallraff, and C. Schönenberger, "Shot Noise of a Quantum Dot Measured with Gigahertz Impedance Matching," *Phys. Rev. Applied*, vol. 4, p. 054002, 2015.

[117] F. Pistolesi and S. Labarthe, "Current blockade in classical single-electron nanomechanical resonator," *Physical Review B*, vol. 76, p. 165317, 2007.

[118] E. M. Weig, R. H. Blick, T. Brandes, J. Kirschbaum, W. Wegscheider, M. Bichler, and J. P. Kotthaus, "Single-Electron-Phonon Interaction in a Suspended Quantum Dot Phonon Cavity," *Physical Review Letters*, vol. 92, no. 4, p. 046804, 2004.

[119] Y. M. Blanter, O. Usmani, Nazarov, and Y. V., "Single-Electron Tunneling with Strong Mechanical Feedback," *Phys. Rev. Lett.*, vol. 93, p. 136802, 2004.

[120] O. Usmani, Y. M. Blanter, and Y. V. Nazarov, "Strong feedback and current noise in nanoelectromechanical systems," *Physical Review B*, vol. 75, p. 195312, 2007.

[121] O. A. Usmani, *Strong Feedback in Nanoelectromechanical Systems*. PhD thesis, TU Delft, 2006.

[122] A. Isacsson and T. Nord, "Low-frequency current noise of the single-electron shuttle," *Europhysics Letters*, vol. 66, no. 5, p. 708, 2004.

[123] J. Kong, H. T. Soh, A. M. Cassell, C. F. Quate, and H. Dai, "Synthesis of individual singlewalled carbon nanotubes on patterned silicon wafers," *Nature*, vol. 395, no. 3, p. 878, 1998.

[124] C. Enss and S. Hunklinger, *Low-temperature physics*. Berlin Heidelberg: Springer-Verlag, 2005.

[125] C. Strunk, *Moderene Thermodynamik*. Berlin München Boston: de Gruyter, 2015.

[126] F. Pobell, *Matter and Methods at Low Temperatures*. Berlin Heidelberg: Springer-Verlag, 3 ed., 2007.

[127] L. DiCarlo, *Mesoscopic Electronics Beyond DC Transport*. PhD thesis, Harvard University, 2007.

[128] M. Görtler, *Temperaturbeständigkeit dünner ferromagnetischer Schichten*. Bachelor thesis, Universität Regensburg, 2013.

[129] A. Donarini, G. Begemann, and M. Grifoni, "All-electric spin control in interference single electron transistors," *Nano Letters*, vol. 9, no. 8, p. 2897, 2009.

[130] M. G. Schultz and F. von Oppen, "Quantum transport through nanostructures in the singular-coupling limit," *Physical Review B*, vol. 80, p. 033302, jul 2009.

[131] K. J. G. Götz, S. Blien, P. L. Stiller, O. Vavra, T. Mayer, T. Huber, T. N. G. Meier, M. Kronseder, C. Strunk, and A. K. Hüttel, "Co-sputtered MoRe thin films for carbon nanotube growth-compatible superconducting coplanar resonators," *Nanotechnology*, vol. 27, no. 13, p. 135202, 2016.

[132] J. B. Gramich, *Andreev and Spin Transport in Carbon Nanotube Quantum Dot Hybrid Devices*. PhD thesis, Universität Basel, 2016.

[133] K. J. G. Götz, *Carbon Nanotube quantum dots : Transport , mechanical charge detection , and fabrication development*. PhD thesis, Universität Regensburg, 2017.

[134] D. R. Schmid, P. L. Stiller, C. Strunk, and A. K. Hüttel, "Magnetic damping of a carbon nanotube nano-electromechanical resonator," *New Journal of Physics*, vol. 14, no. 8, p. 083024, 2012.

[135] A. Nocera, C. A. Perroni, V. M. Ramaglia, G. Cantele, and V. Cataudella, "Magnetic effects on nonlinear mechanical properties of a suspended carbon nanotube," *Physical Review B*, vol. 87, no. 15, p. 155435, 2013.

[136] D. A. Bagrets and Y. V. Nazarov, “Full counting statistics of charge transfer in Coulomb blockade systems,” *Physical Review B*, vol. 67, no. 8, p. 085316, 2003.

[137] M. Niklas, A. Trottmann, A. Donarini, and M. Grifoni, “Fano stability diagram of a symmetric triple quantum dot,” *Physical Review B*, vol. 95, p. 115133, 2017.

[138] A. Baumgartner, G. Abulizi, K. Watanabe, T. Taniguchi, J. Gramich, and C. Schönenberger, “Carbon nanotube quantum dots on hexagonal boron nitride,” *Applied Physics Letters*, vol. 105, no. 2, p. 023111, 2014.

[139] J. J. Viennot, J. Palomo, and T. Kontos, “Stamping single wall nanotubes for circuit quantum electrodynamics,” *Applied Physics Letters*, vol. 104, no. 11, p. 113108, 2014.

[140] J. Gramich, A. Baumgartner, M. Muoth, C. Hierold, and C. Schönenberger, “Fork stamping of pristine carbon nanotubes onto ferromagnetic contacts for spin-valve devices,” *Physica Status Solidi (B) Basic Research*, vol. 252, no. 11, p. 2496, 2015.

[141] S. Sahoo, “An Experimental Investigation of Spin Polarized Transport in Carbon Nanotubes,” 2005.

[142] D. Chevallier, J. Rech, T. Jonckheere, and T. Martin, “Current and noise correlations in a double-dot Cooper-pair beam splitter,” *Physical Review B*, vol. 83, p. 125421, 2011.

Acknowledgement

I would like to express my gratitude for the support experienced during my studies. In particular, I would like to thank the following persons who essentially contributed to my PhD project.

- **Prof. Dr. Christoph Strunk** for offering me the opportunity of joining his group as a PhD student and being part of this exciting research project. I gratefully acknowledge the supervision including the discussions of measurement results and providing advice.
- **Dr. Andrea Donarini** for agreeing to act as second referee for my thesis and for the help with the theoretical analysis of our measurements.
- **Dr. Andreas Hüttel** for the fruitful discussions about nanoelectromechanics.
- **Prof. Dr. Dieter Weiss** for providing the clean room facilities and other infrastructure at the chair.
- **Dr. Nicola Paradiso** for proofreading this thesis, as well as the feedback and advice.
- **Dr. Michael Niklas** for performing the numerical simulations on the dark states and the numerous discussions.
- **Dr. Daniel Steininger** for helping me getting started with the noise setup.
- **Prof. Dr. Dominique Bougeard, Dr. Dieter Schuh and Michaela Trottmann** for providing the QPC for the noise calibration.
- **Christian Bäuml** for carrying out the calibration measurements.
- **Tom Haller, Uli Gürster, Michael Weigl and Daniel Pahl** for the technical support in the laboratories and clean room.

- **Elke Haushalter and Claudia Moser** for taking care of all the administrative tasks.
- **Thomas Solleder and Christian Haimerl** for their supply with liquid helium and nitrogen.
- **All members of the group** for the pleasant atmosphere.
- **My family** for their constant support.

Last but definitely not least I want to thank **Maike Halbhuber** for bearing with me during this period. You always encouraged me not to give up and I am so grateful to have you. I cannot thank you enough for everything!